

Best Available Copy

(12) 10

AD A 078006

RADC-TR-79-221, Vol I (of two)
Interim Report
September 1979

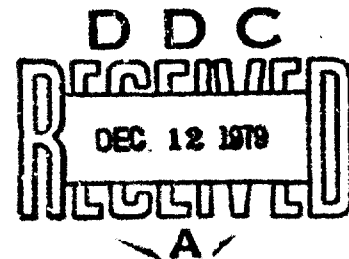


ANALYTICAL STUDIES OF PHASE ESTIMATION TECHNIQUES

EIKONIX Corporation

LEVEL II

sponsored by
Defense Advanced Research Projects Agency (DoD)
ARPA Order No. 3223



APPROVED FOR PUBLIC RELEASE. DISTRIBUTION UNLIMITED

DDC FILE COPY

The views and conclusions contained in this document are those of the authors and should not be interpreted as necessarily representing the official policies, either expressed or implied, of the Defense Advanced Research Projects Agency or the U.S. Government.

ROME AIR DEVELOPMENT CENTER
Air Force Systems Command
Griffiss Air Force Base, New York 13441

79 12 11 010

**Best
Available
Copy**

This report has been reviewed by the RADC Information Office (OI) and is releasable to the National Technical Information Service (NTIS). At NTIS it will be releasable to the general public, including foreign nations.

RADC-1R-79-271, Vol 1 (of two) has been reviewed and is approved for publication.

APPROVED:

DORIS HAMILL, Lt. USAF
Project Engineer

If your address has changed or if you wish to be removed from the RADC mailing list, or if the addressee is no longer employed by your organization, please notify RADC (OCSE), Griffiss AFB NY 13441. This will assist us in maintaining a current mailing list.

Do not return this copy. Retain or destroy.

(U) TR-79-221-VOL-1

UNCLASSIFIED

SECURITY CLASSIFICATION OF THIS PAGE (When Data Entered)

REPORT DOCUMENTATION PAGE		READ INSTRUCTIONS BEFORE COMPLETING FORM
1. REPORT NUMBER	2. GOVT ACCESSION NO.	3. RECIPIENT'S CATALOG NUMBER
RAIDC TR-79-221, Vol-1 (of two)		9
4. TITLE (and Subtitle)	5. TYPE OF REPORT & PERIOD COVERED	
ANALYTICAL STUDIES OF PHASE ESTIMATION TECHNIQUES.	Final Technical Report. September 77 - November 78	
6. AUTHOR(s)	7. PERFORMING ORG. REPORT NUMBER	
R. Chidlaw A. Davaney R. Consalves	EC/2107401-TR-1-VOL-1	
8. PERFORMING ORGANIZATION NAME AND ADDRESS	9. CONTRACT OR GRANT NUMBER(s)	
EIKONIX Corporation 103 Terrace Hall Ave Burlington MA 01803	F30602-77-C-0176 DPA 9416-30231	
10. CONTROLLING OFFICE NAME AND ADDRESS	11. PROGRAM ELEMENT, PROJECT, TASK AREA & WORK UNIT NUMBERS	
Defense Advanced Research Projects Agency 1400 Wilson Blvd Arlington VA 22209	C2230105	
12. MONITORING AGENCY NAME & ADDRESS (if different from Controlling Office)	13. REPORT DATE	
Rome Air Development Center (OCSE) Griffis AFB NY 13441	September 1979	
14. DISTRIBUTION STATEMENT (of this Report)	15. NUMBER OF PAGES	
Approved for public release; distribution unlimited	224	
16. DISTRIBUTION STATEMENT (of the abstract entered in Block 20, if different from Report)	17. SECURITY CLASS (of this report)	
Same	UNCLASSIFIED	
18. SUPPLEMENTARY NOTES	19. DECLASSIFICATION/DOWNGRADING SCHEDULE	
RAIDC Project Engineer: Boris Hamill, Lt. USAF (OCSE)	N/A	
20. ABSTRACT (Continue on reverse side if necessary and identify by block number)		
Phase retrieval Adaptive optics		
21. ABSTRACT (Continue on reverse side if necessary and identify by block number)		
The phase retrieval problem consists of the wave aberration function of an optical system from intensity measurements made in the image plane. An adaptive optical system may then be corrected for the aberration to yield improved performance. Several algorithms for performing phase retrieval are discussed and the results of computer simulations are presented. The sensitivity of the algorithms with respect to type and magnitude of aberrations, image plane detector dimensions and noise levels, non-monochromaticity of incident radiation and the structured target objects is investigated. Results demonstrate the (over)		

DD FORM 1 JAN 73 1473

UNCLASSIFIED

SECURITY CLASSIFICATION OF THIS PAGE (When Data Entered)

311-001

UNCLASSIFIED

SECURITY CLASSIFICATION OF THIS PAGE (When Data Entered)

practicality of phase retrieval.

UNCLASSIFIED

SECURITY CLASSIFICATION OF THIS PAGE (When Data Entered)

Analytical Studies of Phase Estimation Techniques

R. Chidlaw
A. Devaney
R. Gonsalves

Contractor: ELKONIX Corporation
Contract Number: F30602-77-C-0176
Effective Date of Contract: 7 September 1977
Contract Expiration Date: 15 November 1979
Short Title of Work: Analytical Studies of Phase Estimation
Program Code Number: 7E20
Period of Work Covered: September 77 - November 78

Principal Investigator: R. Gonsalves
Phone: 617-273-0350

Project Engineer: Doris Hamill, Lt., USAF
Phone: 615-340-3148

Approved for public release; distribution unlimited

This research was supported by the Defense Advanced Research Projects Agency of the Department of Defense and was monitored by Doris Hamill (OCSE), Griffiss AFB NY 13441 under Contract F30602-77-C-0176.

Accession For	
NTIS GRA&I	<input checked="checked" type="checkbox"/>
DOC TAB	<input type="checkbox"/>
Unannounced	<input type="checkbox"/>
Justification	
By	
Distribution/	
Availability Codes	
List	Avail and/or special
A	

TABLE OF CONTENTS

Section	Title	Page
1.0	INTRODUCTION	1
2.0	ANALYSIS	11
2.1	Summary	11
2.2	The Effect of Aliasing on Phase Retrieval	11
2.3	The Effect of Large Aberrations of Phase Retrieval	16
2.4	A Procedure for Increasing the Effective Sampling Rate of an Array of Detectors	22
2.5	The Effects of Finite Detector Size and Scene Spatial Frequency Content on Phase Retrieval	28
2.6	The Effect of Non-Monochromatic Radiation on the Point Spread Function	32
3.0	THE GERCHBERG-SAXTON ALGORITHM	44
4.0	THE DEVANEY-GONSALVES ALGORITHM	53
4.1	Noise-Free Point Detector Results	53
4.2	Effects of Noise	77
4.3	Effects of Non-Point Detectors	88
5.0	THE TWO-IMAGE PLANE ALGORITHM	98
5.1	Introduction	98
5.2	Results	98
6.0	CONCLUSIONS AND RECOMMENDATIONS	104
Appendix A	The Devaney-Gonsalves Algorithm (separate document)	A-1
Appendix B	The Two-Image Plane Algorithm (separate document)	B-1

TABLE OF FIGURES

Number	Title	<u>Page</u>
1.1	Graphic Illustration of the Use of a Phase Retrieval Algorithm in an Adaptive Imaging System.	4
1.2	Block diagram of control loop of an adaptive imaging system using an "inverse filter" to estimate the PSF from imagery of a known object	5
1.3	Cassegrain system with adaptive secondary (e.g., deformable mirror) and dual image planes consisting of Charge Coupled Device arrays (CCD) located at different distances from secondary.	6
1.4	Block diagram illustrating the operation of the Gerchberg-Saxton (G.S.) Algorithm for estimating the phase of the generalized pupil function $F_{p,k}$ from its modulus $f(p,k)$ and the modulus $h(x_n, y_m, t)$ of its p,k Fourier transform n,m	8
2.1	Two Functions Yielding the Same Geometric Optics Transfer Function	20
2.2	Mirror Image Functions Possessing Identical Transfer Functions	21
2.3	Two sets of samples of a PSF obtained at the two times t_1 and $t_2 = t_1 + d/v$. A relative linear velocity of V^2 is assumed to exist between the PSF and the detector array.	24
2.4	Samples of a PSF moving at a uniform velocity at 45° relative to the horizontal axis of an array of point detectors (large dots).	25
2.5	Values of α Satisfying Equation (2.22)	
2.6	Samples of a PSF moving at a uniform velocity at 26.58° relative to the horizontal axis of an array of point detectors (large dots).	28
2.7	Sampling Array Geometry	29
2.8	One Wave of Defocus at a Single Wavelength	34
2.9	Polychromatic Case For One Wave of Defocus	35
2.10	Polychromatic Case For One Wave of Defocus	36
2.11	One Wave of Coma At a Single Wavelength	37
2.12	Polychromatic Case For One Wave of Coma	38
2.13	Polychromatic Case For One Wave of Coma	39
2.14	One Wave of Defocus Plus One Wave of Coma at a single Wavelength	40

TABLE OF FIGURES (Continued)

<u>Number</u>	<u>Title</u>	<u>Page</u>
2.15	Polychromatic Case For One Wave Of Defocus Plus One Wave of Coma	41
2.16	Polychromatic Case For One Wave of Defocus Plus One Wave of Coma	42
3.1	Gerchberg-Saxton Phase Retrieval Algorithm	45
4.1	Contour Plot of Initial Phase Aberration Function - Test 5	54
4.2	Contour Plot of Initial MTF - Test 5	55
4.3	Contour Plot of Estimated Phase Aberration Function - Test 5	56
4.4	Contour Plot of the Residual Phase Aberration - Test 5	57
4.5	Contour Plot of MTF from the Residual Phase Aberration	58
4.6	Contour Plot of Initial Phase Aberration Function	59
4.7	Contour Plot of Initial MTF	60
4.8	Contour Plot of Estimated Phase Aberration Function	61
4.9	Contour Plot of the Residual Phase Aberration (initial phase aberration less the estimated phase aberration)	62
4.10	Contour Plot of MTF from Residual Phase Aberration.	63
4.11	Contour Plot of Initial Phase Aberration Function.	64
4.12	Contour Plot of Initial MTF	65
4.13	Contour Plot of Estimated Phase Aberration Function	66
4.14	Contour Plot of the Residual Phase Aberration	67
4.15	Contour Plot of MTF from the Residual Phase Aberration	68
4.16	Test 14 Phase Aberration	69
4.17	Contour Plot of Initial Phase Aberration Function	70
4.18	Contour Plot of Initial MTF	71

TABLES OF FIGURES (Continued)

<u>Number</u>	<u>Title</u>	<u>Page</u>
4.19	Contour Plot of Estimated Phase Aberration Function	72
4.20	PSF Input to First Iteration	74
4.21	PSF After First Correction	75
4.22	PSF After Second Correction	76
4.23	Initial Phase Aberration	79
4.24	Initial MTF	80
4.25	Initial MTF with Added Noise	81
4.26	Estimated Phase in Noisy Case	82
4.27	Residual Phase Aberration After Correction in Noisy Case	83
4.28	MTF After Correction in Noisy Case	84
4.29	Original PSF	85
4.30	Original PSF with Noise	86
4.31	Corrected PSF from First Run of Algorithm in Noisy Case	87
4.32	Corrected PSF from Noise-Free Case	89
4.33	Corrected PSF from improved algorithm in noisy case	89a
4.34	Initial System Point Spread Function	91
4.35	Initial Phase Aberration Across the Exit Pupil	92
4.36	Initial Point Spread Function Convolved with Detector Size	93
4.37	Measured Initial Point Spread Function Including Detector Noise and Detector Size	94
4.38	Phase Retrieval Estimate of Wavefront Aberration	95
4.39	System Point Spread Function After Correction	97
5.1(a)	Case N, Original MTF	100
5.1(b)	Case N, Noisy MTF	100
5.1(c)	Case Z, Transform of Detected Signal of Point Object	101
5.1(d)	Case Z, Transform of Detected Signal of Point Object Plus Noise	101

TABLES OF FIGURES (Continued)

Number	Title	<u>Page</u>
5.2(a)	Case CC, Transform of Detected Signal of Extended Object	102

LIST OF TABLES

Number	Title	Page
3.1	Results of Tests of the Two-Dimensional Gerchberg-Saxton Algorithm	47
3.2	Random Number Seeds	49
3.3	Parameters for Convergence Acceleration	52
5.1	Results of the Two Image Plane Simulations	99
5.2	Results of the Two Image Plane Simulations	100
5.3	Results of the Two Image Plane Simulations	101

1.0 INTRODUCTION

The question of whether or not the wave aberration function $W(u,v)$ of an isoplanatic imaging system is uniquely retrievable from the system's point spread function (PSF) appears to have been first studied by A. Walther and E. O'Neill^(1,2). Basing their investigations on the well-known result that the so-called generalized pupil function

$$F(u,v) = f(u,v) e^{ik_0 W(u,v)} \quad (1.1)$$

forms a Fourier transform pair with the coherent spread function

$$\psi(x,y) = \iint du dv F(u,v) e^{-i(u x + v y)}, \quad (1.2)$$

Walther and O'Neill correctly noted that the problem of deducing $W(u,v)$ from the PSF

$$h(x,y) = |\psi(x,y)|^2 \quad (1.3)$$

really amounts to that of retrieving the phase of $\psi(x,y)$ from its modulus. The problem of determining the phase of a complex function from the functions' modulus is usually termed a phase retrieval problem and, as discussed by Walther and O'Neill, does not generally admit a unique solution unless auxiliary information of some sort is available regarding the complex quantity whose phase is to be determined (in this case the coherent spread function $\psi(x,y)$). As an example of this indeterminacy, we

1. E.L.O'Neill and A.Walther, "The question of phase in image formation," Opt. Acta 10, 33-40 (1963).
2. A. Walther, "The question of phase retrieval in optics," Opt. Acta 10, 41-49 (1963).

note that for any imaging system possessing a radially symmetric pupil function, the wave aberration functions $W(\rho, \theta)$ and $-W(-\rho, -\theta)$ yield identical PSF's. Thus, for such systems, estimates of the wave aberration function based on knowledge only of the PSF will be indeterminate at least up to transformations of the type given above.

For the moment let us suppose that besides the PSF we also have available the pupil function $P(\rho, \theta)$ or, what amounts to the same thing, the modulus $|P(\rho, \theta)|$ of the generalized pupil function. Because $h(x, y)$ and $P(\rho, \theta)$ form a Fourier transform pair, the problem of deducing the phase of $h(x, y)$ from its modulus $h^{1/2}(x, y)$ becomes that of deducing the phase of a function (i.e., $h(x, y)$) given the modulus of the function and the modulus of its Fourier transform (i.e., $P(\rho, \theta)$). It happens that precisely this latter problem arises in electron microscopy^(3,4) where certain workers have investigated the possibility of deducing the phase of a coherently illuminated object from intensity measurements performed in both the image and diffraction planes of an electron microscope. In this connection Gerchberg and Saxton⁽⁵⁾ devised an algorithm using multiple Fast Fourier Transforms (FFT's) for retrieving a function from its modulus and the modulus of its Fourier transform. Although no one has (to our knowledge) been able to furnish an acceptable uniqueness theorem as to the solutions obtained by the Gerchberg-Saxton algorithm, we

1. L.J. Misell, "An examination of iterative method for the solution of the phase problem in optics and electron optics," J. Phys. 96, 2220-2225 (1973).
2. A.J. Brenth et al., The problem of phase retrieval in light and electron microscopy of strong optics, "Opt. Acta 22, 615-628 (1975).
3. R.W. Gerchberg and W.O. Saxton, "Phase determination from image and diffraction plane pictures in the electron microscope," Optik. 34, 275-283 (1971). R.W. Gerchberg and W.O. Saxton, "A practical algorithm for the determination of phase from image and diffraction plane pictures," Optik. 35, 237-246 (1972)

and others have found simulation studies that the algorithm can be expected to yield a unique phase reconstruction so long as the moduli of the function and its Fourier transform are adequately sampled.

The Gerchberg-Saxton algorithm is not the only computation technique available for deducing the phase of a complex function from its modulus and the modulus of its Fourier transform. An alternative scheme has also been proposed by Gerchberg and Saxton while Gonsalves provided an algorithm⁽⁶⁾ specifically tailored to the problem of deducing the aberrations of a lens from the lens' pupil function and point spread function.

The problem of deducing a lens' wave aberration function from its point spread function is intimately connected to the problem of estimating wavefront distortions of adaptive optical imaging systems from imagery of a star object. In this later application, the image of the star object is detected by a square array of photodiodes to yield an estimate of the PSF. The PSF estimate is then input to a digital processor programmed with the phase retrieval algorithm. The output from the processor is an estimate $\hat{W}(\lambda, \rho)$ of the wave aberration function $W(\lambda, \rho)$ which is then used to determine the appropriate control signals required to drive the adaptive imaging system to a state having a more

6. R.A. Gonsalves, "Phase retrieval from modulus data," J.Opt. Soc.Am. 66, 961-964 (1976).

favorable aberration function. This procedure is illustrated graphically in Figure 1.1.

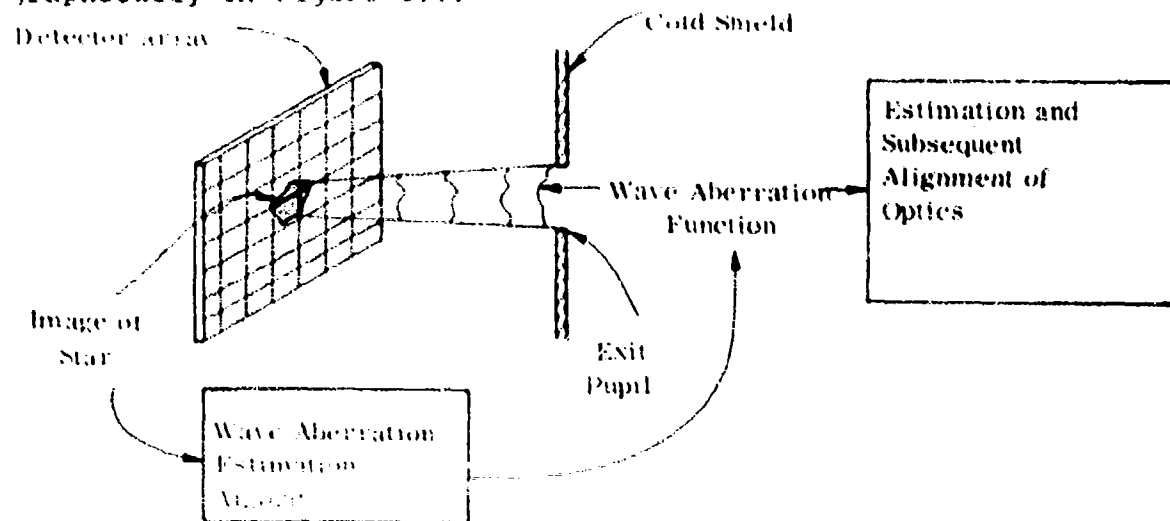


Figure 1.1 Graphic Illustration of the Use of a Phase Retrieval Algorithm in an Adaptive Imaging System.

The phase retrieval algorithms discussed above can also be applied in situations where the system PSF is not directly observable but can, nevertheless, be estimated from imagery produced by the system. For example, if we restrict our attention to a single isoplanatic patch the image intensity profile $I(x,y)$ and object intensity profile $O(x,y)$ are related via the equation

$$I(x,y) = \iint_{-\infty}^{\infty} dx' dy' O(x',y') h(x-x', y-y') \quad (1.4)$$

where $h(x,y)$ is the system PSF corresponding to the particular isoplanatic patch in question. If the object profile $O(x,y)$ is known the Equation (1.4) can be inverted (eq., by use of Fourier transforms) to yield the PSF $h(.)$ which can be directly input to a phase retrieval algorithm. A block diagram illustrating the procedure is presented in Figure 1.2.

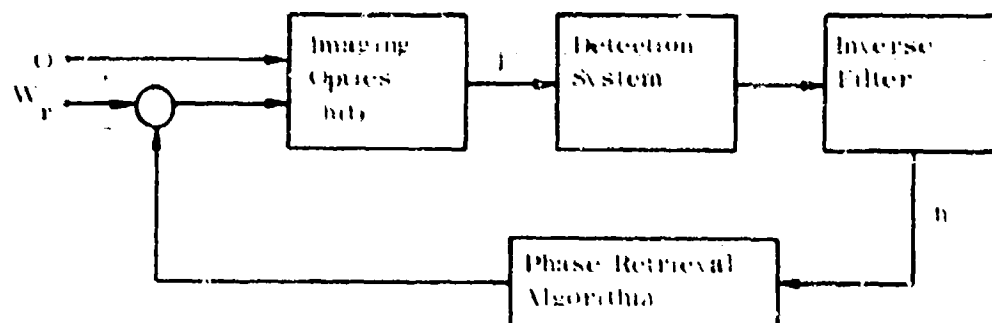


Figure 1.2 Block diagram of control loop of an adaptive imaging system using an "inverse filter" to estimate the PSF from imagery of a known object. The estimated PSF is input to a phase retrieval algorithm for determination of the system aberrations for subsequent control of the optics.

In cases where the scene being imaged is either completely or partially unknown one can still employ the aberration estimation algorithm discussed above in conjunction with techniques which adaptively estimate the scene being imaged. The overall process may, however, require long execution times and, thus, may not even converge in cases where the image motion is pronounced. For this reason EIKONIX has developed an algorithm which allows one to estimate an optical system's aberration function from two images of an unknown scene recorded at different

system defocus values. Hence, by the use of dual image planes such as shown in Figure 1.3 in conjunction with the aforementioned algorithm, it is possible to assess the wave aberration function of the imaging system. It is important to stress that no a priori information regarding the scene being imaged need be known and no dithering of elements within the adaptive optical system is required to deduce the wavefront distortions. Just as was the case when the scene being imaged is known, the entire process measurement-wave aberration estimation-correction is completely accomplished in open loop fashion using only the imagery recorded over the two image planes shown in Figure 1.3.

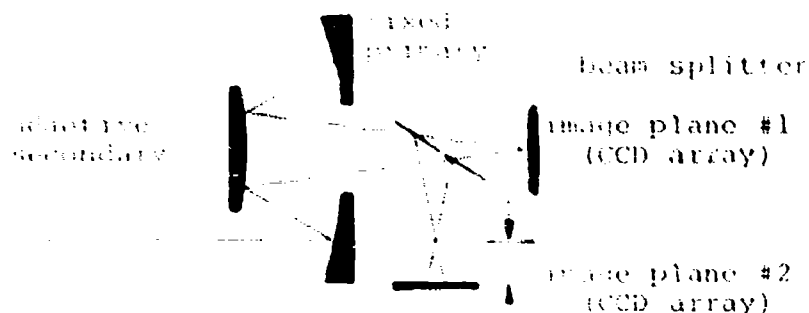


Figure 1.3 Cassegrain system with adaptive secondary (e.g., deformable mirror) and dual image planes consisting of Charge Coupled Device arrays (CCD) located at different distances from secondary. In the above figure image plane #1 is located at best focus while image plane #2 is defocused by the (known) amount of d from plane #1.

This document constitutes the Final Report on Contract F30602-77-C-0176 titled "Analytical Studies of Phase Estimation Techniques." The objective of this program was to evaluate the application of the optical system wavefront aberration estimation techniques discussed above to multi-element wide field of view optical configurations. To this end it was necessary to:

(1) perform an analytical investigation into the theory of wave aberration estimation; (2) develop wave aberration estimation algorithms to be used in computer simulation studies and, (3) to perform computer simulations against known and unknown scenes in the presence of varying amounts of noise and wavefront error.

The estimation techniques under investigation can be classified as shown in Diagram 1.1. In this diagram "G.S. phase retrieval algorithm" stands for the "Gerchberg-Saxton" algorithm which uses the multiple Fourier transform technique described in the Proposal for this contract and shown schematically in Figure 4.

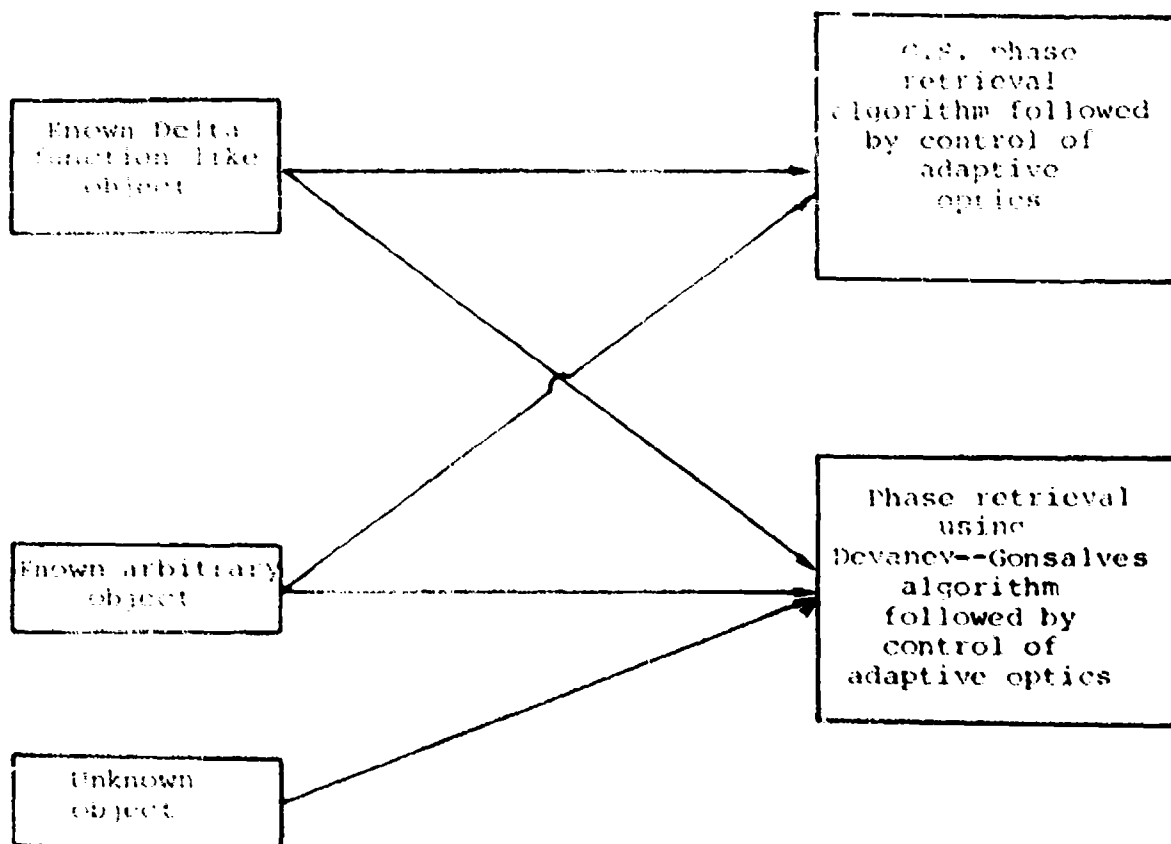


Diagram 1.1 Alternative System Philosophies

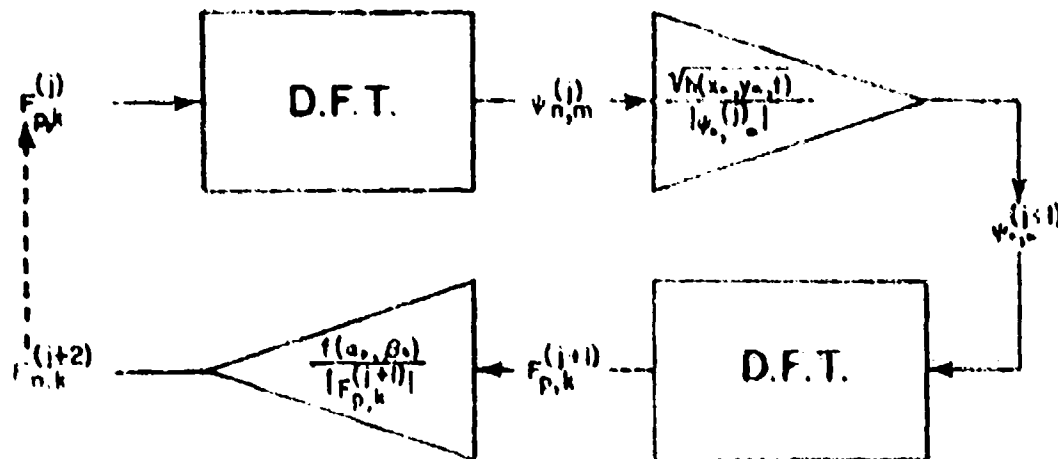


Figure 1.4 Block diagram illustrating the operation of the Gerchberg-Saxton (G.S.) Algorithm for estimating the phase of the generalized pupil function $F_{p,k}$ from its modulus $f(\alpha_p, \beta_p)$ and the modulus $V_n(x_n, y_n, l)$ of its Fourier transform $\psi_{n,m}$.

The results from the analytical investigation phase of the program are reported in Chapter 2. This phase of the effort included investigations into the effects of polychromatic radiation, detector noise, image motion, image aliasing, aberration magnitude and spatial frequency content of scenes on the process of phase retrieval. The results of this investigation indicate that:

1. The spectral radiation bands anticipated in the HALO mission do not pose a problem for the phase retrieval algorithms.
2. The NEFD's of CCD arrays anticipated for use in the HALO mission are such that electronic detector noise will not seriously degrade the performance of the phase retrieval algorithms.

3. Image aliasing will seriously degrade the performance of the algorithms but can be overcome by use of a multiplex sampling scheme discussed in Chapter 2.
4. The performance of the phase retrieval algorithms is optimum for moderate amounts of aberration. The performance for very weak and very strong amounts of aberration depends on the signal to noise ratio and on the spatial frequency content of the scenes being imaged.
5. The effects of scene spatial frequency content and finite detector size on the phase estimation algorithms depend on the amount of aberration - simulation studies.

A large part of the work performed in the program was, of course, devoted to actually generating new software to implement the various aberration estimation techniques. Software generated during the course of the program includes:

1. A program to generate two-dimensional PSF's.
2. A program to perform the two-dimensional Gerchberg-Saxton algorithm.
3. A program to perform the Devaney-Gonsalves algorithm on two-dimensional data from the one image plane.
4. A program to perform the Devaney-Gonsalves algorithm on two-dimensional data from the two image plane.
5. A program to generate polychromatic one-dimensional OTF's.

The last task in the Statement of Work (Task 4.2.3) calls for computer testing of the various aberration estimation software packages developed in the program. The results from representative simulations are presented in Chapters 3, 4, and 5.

The results from the simulation studies using the Gerchberg Saxton (G.S.) algorithm are presented in Chapter 3. This algorithm did not perform well in the simulations. In particular, the results of the simulations indicate that the algorithm is not

"robust" in two dimensions (i.e., its performance is highly dependent on the choice of a starting estimate). Because of this it was decided to proceed directly to the two dimensional Devaney-Gonsalves algorithm early in the course of the program.

The results from testing of the two-dimensional Devaney-Gonsalves algorithms are presented in Chapter 4. We say algorithms because, as required by Task 4.1.6 of the Statement of Work, a number of algorithms were developed and tested corresponding to different models of the wave aberration function; the principle conclusion to be drawn from the simulation studies presented in Chapter 4 is that these algorithms work extremely well and are very robust so long as there is no limit to the amount of computation time allowed. Sometimes extremely long execution times are required by the algorithms. The reasons for this are discussed in detail in Appendix A, along with a statement of the algorithm and a more complete presentation of the results of Chapter 4.

Chapter 5 presents results of the two image plane simulations. One particular wavefront aberration is used, with varying noise levels, detector sizes, and object spectra. Results show that the algorithm will yield good estimates even in the presence of large amounts of noise, large detectors, and large objects. However, the same problem of long execution times is present as in the one image case. Appendix B presents a proprietary version of Chapter 5.

2.0 ANALYSIS

2.1 SUMMARY

In this Chapter we review the work performed on the tasks contained with the "Analysis" paragraph (4.1) of the "Statement of Work" for the Contract. In Section 2.2 we discuss the effect of undersampling of an image of a star object. For this case it is shown that the phase retrieval is not unique. In Section 2.3 we show that the phase retrieval will also not be unique if the aberrations are such that the Optical Transfer Function (OTF) is well approximated by the so-called "Geometrical Optics" OTF. Section 2.4 discusses a possible technique for achieving Nyquist rate sampling by means of a sampling multiplex procedure. The effect of finite detector size and of scene spatial frequency content are discussed in Section 2.5 where a theorem is established which shows that these two factors have precisely the same effect on phase retrieval. Finally, Section 2.6 addresses the question of the effect of non-monochromatic light on phase retrieval.

2.2 THE EFFECT OF ALIASING ON PHASE RETRIEVAL

For the case of a star object the phase retrieval problem reduces to that of determining the phase of the coherent spread function,

$$\psi(x) = \int_{-\alpha_0}^{\alpha_0} d\alpha F(\alpha) e^{-i\alpha x}, \quad (2.1)$$

from its modulus $|\psi(x)|$ and the modulus of its Fourier transform $F(\alpha)$. In the above equation $\alpha = \frac{2\pi}{f\lambda} u$ is a "reduced coordinate," with f being the focal length of the imaging system, λ the wavelength of the light field and u the position coordinate over the exit pupil. The argument of $\psi(x)$ denotes position along the image plane. For simplicity of presentation we have restricted

our attention to the one-dimensional case. The results established below hold equally well in the case of two dimension, however.

We note that since the integral in Equation (2.1) extends only over the finite interval $[-a_0, a_0]$ we may expand the Generalized Pupil Function $F(a)$ in a Fourier series with period $2Na_0$.

$$F(a) = \sum_{v=-\infty}^{\infty} C_v e^{i \frac{2\pi}{2Na_0} v a} \quad (2.2)$$

where N is any integer \geq unity. When Equation (2.2) is submitted into Equation (2.1) one obtains

$$\psi(x) = \sum_{v=-\infty}^{\infty} C_v \int_{-a_0}^{a_0} da e^{i \left(\frac{\pi}{Na_0} v - x \right) a} \quad (2.3)$$

$$= \sum_{v=-\infty}^{\infty} C_v \cdot 2 \left[\frac{\sin \left(\frac{\pi}{Na_0} v - x \right) a_0}{\left(\frac{\pi}{Na_0} v - x \right)} \right]$$

However, from Equation (2.2) we conclude that

$$C_v = \frac{1}{2Na_0} \int_{-a_0}^{a_0} da F(a) e^{-i \left(\frac{\pi}{Na_0} v \right) a} = \frac{1}{2Na_0} \psi \left(x = \frac{\pi}{Na_0} v \right) \quad (2.4)$$

where we have used Equation (2.1). Finally, upon substituting from Equation (2.4) into Equation (2.3) we obtain the sampling series representation of $\psi(x)$:

$$\psi(x) = \frac{1}{N} \sum_{v=-\infty}^{\infty} \psi\left(x - \frac{\pi}{Na_0} v\right) \text{sinc} \left\{ a_0 \left(x - \frac{\pi}{Na_0} v \right) \right\}. \quad (2.5)$$

It is important to note that for the sampling series (2.5) to hold the quantity N must be a positive integer greater than or equal to unity. If $N = 1$, the complex function $\psi(x)$ is said to be sampled at its Nyquist Rate while for $N > 1$ it is sampled above its Nyquist Rate (oversampled). Now the modulus square $|\psi|^2$ of $\psi(x)$ also admits a sampling series representation. In particular, it is not difficult to show that

$$|\psi(x)|^2 = \frac{1}{M} \sum_{v=-\infty}^{\infty} \left| \psi\left(x - \frac{\pi}{M(2a_0)} v\right) \right|^2 \text{sinc} \left\{ a_0 \left(x - \frac{\pi}{M(2a_0)} v \right) \right\}, \quad (2.6)$$

where M is also a positive integer greater or equal to unity. Again, if $M = 1$, $|\psi(x)|^2$ is said to be sampled at its Nyquist rate while if $M > 1$ it is said to be oversampled.

We note that the Nyquist rate for the modulus of ψ (or, equivalently $|\psi(x)|^2$) is twice the Nyquist rate for ψ . (This can be shown to be due to the fact that the bandwidth of the modulus of a function is twice that of the function itself.) In particular, the maximum sample spacing allowed for adequate sampling of $\psi(x)$ is

$$\Delta_{\psi} = \frac{\pi}{a_0} = \Delta F_{\psi}, \quad (2.7)$$

while the maximum sample spacing allowed for sampling of the modulus of $\psi(x)$ (or, equivalently, of $|\psi(x)|^2$) is

$$\Delta_{|\psi|} = \frac{\pi}{2a_0} = \frac{\Delta F_{\psi}}{2} = \frac{1}{2} \Delta_{\psi}, \quad (2.8)$$

We shall now show that if the modulus of ψ is sampled at or below the Nyquist rate for ψ (i.e., if $\Delta_\psi \geq \Delta_\psi$), then the retrieval of the phase of ψ from its modulus and the modulus $|F(\alpha)|$ of its Fourier transform will not be unique if the pupil function is a constant.

Theorem I

Let the pupil function $f(\alpha) = |F(\alpha)| = f_0$ be constant. Further, let $W(\alpha)$ be a continuous but otherwise arbitrary wave aberration function defined over the exit pupil $-\alpha_0 \leq \alpha \leq \alpha_0$ and let μ be a real number in this same interval. Then any aberration function of the form

$$W_\mu(\alpha) = \begin{cases} W(\alpha - \mu + \alpha_0) & \text{if } -\alpha_0 \leq \alpha < \mu \\ W(\alpha - \mu - \alpha_0) & \text{if } \mu < \alpha \leq \alpha_0 \end{cases} \quad (2.9)$$

will generate a coherent spread function $\psi_\mu(x)$ having the same modulus $|\psi(x)|$ at the sample points $x = n \Delta_\psi$; $n = 0, \pm 1, \pm 2, \dots$

Proof of Theorem I

From Equation (2.1) we have that

$$\psi_\mu(x) = \int_{-\alpha_0}^{\alpha_0} d\alpha F_\mu(\alpha) e^{-i\alpha x} = f_0 \int_{-\alpha_0}^{\alpha_0} d\alpha e^{i\frac{x^2}{2} W_\mu(\alpha)} e^{-i\alpha x}. \quad (2.10)$$

On substituting from Equation (2.9), we obtain

$$\begin{aligned} \psi_{\mu}(x) = f_0 \int_{-a_0}^{\mu} da e^{i \frac{2\pi}{\lambda} W(a - \mu + a_0)} e^{-iax} \\ + f_0 \int_{\mu}^{a_0} da e^{i \frac{2\pi}{\lambda} W(a - \mu + a_0)} e^{-iax}, \end{aligned} \quad (2.11)$$

which simplifies to become

$$\begin{aligned} \psi_{\mu}(x) = f_0 e^{-i(\mu - a_0)x} \int_{-\mu}^{a_0} da' e^{i \frac{2\pi}{\lambda} W(a')} e^{-iaa'x} \\ + f_0 e^{-i(\mu + a_0)x} \int_{-\mu}^{\mu} da' e^{i \frac{2\pi}{\lambda} W(a')} e^{-iaa'x}. \end{aligned} \quad (2.12)$$

If we put

$$x = n \Lambda_{\psi} = \frac{n}{a_0} \quad (2.13)$$

then $a_0 x = n$ and Equation (2.12) gives

$$\psi_{\mu}(x=n\Lambda_{\psi}) = e^{-in\Lambda_{\psi}} \int_{-\mu}^{a_0} da' e^{i \frac{2\pi}{\lambda} W(a')} e^{-ia'(n\Lambda_{\psi})} \quad (2.14)$$

$$= e^{-in\Lambda_{\psi}} \psi(x=n\Lambda_{\psi}) \quad (2.14)$$

which establishes the theorem.

The above Theorem shows that it is extremely important to sample at the Nyquist rate appropriate for the intensity of the image in order to obtain a unique determination of the wave aberration function. As we shall show in the following section nonuniqueness of the phase retrieval problem is also encountered when the aberrations of the system are so severe that geometrical optics gives a complete description of the image forming properties of the system.

2.3 THE EFFECT OF LARGE ABERRATIONS OF PHASE RETRIEVAL

The distinguishing characteristic of a highly aberrated imaging system is the relative unimportance of diffraction and interference effects in determining its image forming properties. In particular, it is common practice to characterize such systems by the so-called "Geometrical Optics Optical Transfer Function" rather than the exact (within the limits of scalar diffraction theory) transfer function given by

$$\text{OTF}(F_x, F_y) = \iint du dv f(u, v) f(u + 2\lambda F_\theta F_x, v + 2\lambda F_\theta F_y) \exp \left[i \frac{2\pi}{\lambda} \left[W(u, v) - W(u + 2\lambda F_\theta F_x, v + 2\lambda F_\theta F_y) \right] \right] \quad (2.15)$$

where F_θ is the F number of the imaging system. The Geometrical Optics Transfer Function is obtained from the exact expression given in Equation (2.15) by taking the Geometrical Optics limit $\lambda \rightarrow 0$. The details of performing the required limiting operation are quite straightforward, (cf., K. Miyamoto, "Wave Optics and Geometrical Optics in Optical Design", in Progress in Optics, ed., E. Wolf (North Holland, Amsterdam, 1966), Vol. I, p.43), and one obtains

$$\text{OTF}_{\text{G.O.}}(F_x, F_y) = \iint_{\Lambda} du dv \exp \left[-i4\pi F_\theta \left[F_x \frac{\partial W(u, v)}{\partial u} + F_y \frac{\partial W(u, v)}{\partial v} \right] \right] \quad (2.16)$$

In Equation (2.16) A represents the area of the unit circle and $OTF_{G.O.}$ is the Geometrical Optics OTF.

In the following analysis we employ the Geometric Optics Transfer Function given in Equation (2.16). It is found that this quantity by itself does not uniquely determine the slopes $(\partial W/\partial u, \partial W/\partial v)$ of the wave aberration function. In other words, within the framework set by Geometrical Optics, wavefront estimation via the use of phase retrieval techniques is not unique.

It is extremely important to note that this nonuniqueness holds only in the geometric optics limit when diffraction and interference effects can be completely ignored. These effects will be present no matter how large the aberrations and it is, evidently, precisely these effects that are responsible for the success (and apparent uniqueness) of phase retrieval techniques in the case of small and moderate amounts of aberration. If the measurement process used to deduce the OTF were perfect, then the effects of diffraction and interference on the OTF would be observable and, hence, the process of phase retrieval would (presumably) be unique. However, when the aberrations are large and measurement noise is present, these effects can become "lost" in the noise with the result that the Geometrical Optics Transfer Function fits the noisy data quite well and phase retrieval will not be unique.

The severity of the aberrations and the amount of measurement noise required to cause phase retrieval techniques to fail is not known at present and can probably not be determined in advance even for the simplest optical configurations. However, preliminary one-dimensional computer simulations indicate that diffraction effects play an important role even for cases of very severe (in excess of ten waves of aberration) wavefront errors.

Finally, it should be noted that although the results presented below establish the fact that the wave aberration function cannot be uniquely deduced from the Geometrical Optics Transfer Function alone it is quite conceivable that certain types of auxiliary information concerning the aberration function might lead to a unique specification of this quantity. In particular, it appears likely that the phase retrieval will yield a unique solution if one knows in advance that the wave aberration function admits a finite order polynomial representation; e.g., an expansion into the classical wave aberration polynomials.

Proof of Nonuniqueness in the Geometric Optics Limit

For simplicity, let us consider first the one-dimensional case where $OTF_{G.O.}$ reduces to

$$OTF_{G.O.}(F_x) = \int_{-1}^1 du e^{i F_x g(u)}, \quad (2.17)$$

with

$$g(u) = -4\pi F \frac{\partial W(u)}{\partial u}.$$

We now establish the following Theorem.

Theorem II

If $g(u)$ is a bounded solution to the integral equation (2.17) then so too is the real valued bounded function $d(u)$ which satisfies the infinite set of conditions

$$\int_{-1}^1 du g^n(u) = \int_{-1}^1 du d^n(u); \quad n = 1, 2, 3, \dots, \quad (2.18)$$

but is otherwise arbitrary.

Proof of Theorem II

Since the integral in Equation (2.17) extends over a finite interval and the Taylor series expansion of $\exp[i F_x g(u)]$ is uniformly convergent within this interval (due to the assumed boundedness of $g(u)$) we may write

$$\text{OTF}_{\text{G.O.}}(F_x) = \sum_{n=0}^{\infty} \frac{(i F_x)^n}{n!} \int_{-1}^1 du g^n(u) \quad (2.19)$$

If the bounded function $d(u)$ satisfies the infinite set of conditions given in Equation (2.18), then we can replace each integral on the r.h.s. of Equation (2.19) with the r.h.s. of Equation (2.15) and thus obtain

$$\text{OTF}_{\text{G.O.}}(F_x) = \sum_{n=0}^{\infty} \frac{(i F_x)^n}{n!} \int_{-1}^1 du d^n(u) = \int_{-1}^1 du e^{i F_x d(u)}, \quad (2.20)$$

where the last equality results from the assumed boundedness of $d(u)$ and, hence, the uniform convergence of the sum. This proves the theorem.

Theorem II implies that the quantity $g(u)$ and, hence, the derivative of the wave aberration function $\partial W(u)/\partial u$ (i.e., the wavefront slope) cannot be uniquely deduced from the Geometric Optics Transfer Function. In particular, it is easily verified that the infinite set of conditions given in Equation (2.18) hold if segments of the $g(u)$ function are interchanged. Even if one imposes the further condition that the function $d(u)$ be continuous, it is still not difficult to construct a function which satisfies these conditions. Figure 2.1 illustrates one method of generating an equivalent

function $d(u)$; the level d_0 can be shifted at will, showing that there are an infinite number of such functions which yield the same transfer function. From the method of construction, these equivalent functions may not have continuous first derivatives.

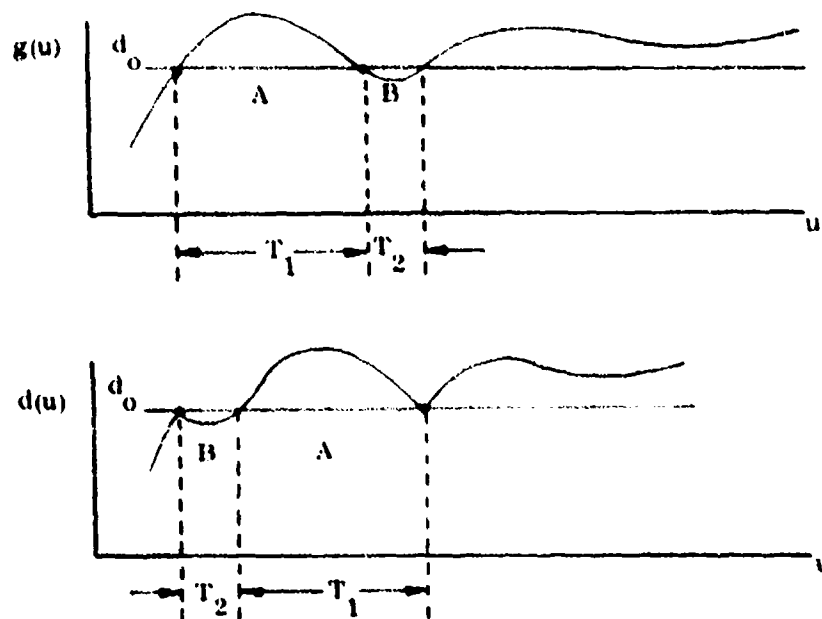


Figure 2.1 Two Functions Yielding the Same Geometric Optics Transfer Function

An equivalent function possessing all the quantities of the original function $g(u)$ consists of the "mirror image" of the original function. That is, the function $S(u) = g(-u)$ as shown in Figure 2.2., will have the same transfer function. This can be proved by direct substitution:

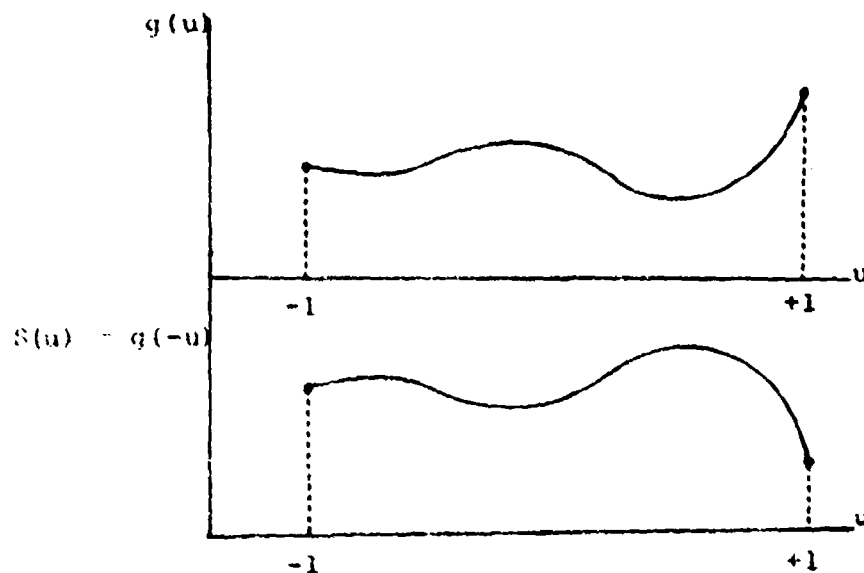


Figure 2.2 Mirror Image Functions Possessing Identical Transfer Functions

In a practical situation, the wave aberration function and hence its slope $g(u)$ is a sampled, discrete process. We see that if there are N independent samples, we may arrange them in any order, thus generating $N!$ different functions which correspond to the same transfer function. There may be several sets of samples which assume the same quantized values; thus the number of distinguishable displacement functions is accordingly decreased, but this is not important to this discussion. The important point to note is the lack of uniqueness in determining an aberration function from a

Geometrical Optics Transfer Function.

An entirely parallel discussion as that presented above implies for the two-dimensional case. In particular, we have the following theorem;

Theorem III

Let $\partial W(u,v)/\partial u$ and $\partial W(u,v)/\partial v$ be the first partial derivatives of a wave aberration function which yields the Geometric Optics Transfer Function.

$$\text{OFT}_{\text{G.O.}}(F_x, F_y) = \iint_A du dv e^{-i4\pi F \left[F \frac{\partial W(u,v)}{\partial u} + F_y \frac{\partial W(u,v)}{\partial v} \right]} \quad (2.21)$$

Further, let $\partial W/\partial u$ and $\partial W/\partial v$ be everywhere bounded within the pupil area A . Then there exists at least one other wave aberration function $\bar{W}(u,v)$ which also has bounded first partial derivatives $\partial \bar{W}/\partial u$, $\partial \bar{W}/\partial v$ and which yields the same Geometric Optics Transfer Function as does $W(u,v)$.

We omit a proof of Theorem III since it follows directly from the discussion presented above for the one-dimensional case.

2.4 A PROCEDURE FOR INCREASING THE EFFECTIVE SAMPLING RATE OF AN ARRAY OF DETECTORS

As shown in Section 2.1 the phase retrieval problem does not admit a unique solution if the PSF is sampled below the Nyquist rate of $(2/\lambda F\#)$ samples per unit length. Throughout this document it is assumed that this sampling requirement is met. However, it is anticipated that the actual detectors to be used in the HALO mission will be too large to meet this rather

stringent sampling requirement and, thus, it was necessary to explore alternative procedures for achieving the required sampling rates.

The procedure described in this section uses a relative image motion between the detector array and the image from which the aberration estimation is being performed to obtain a higher sampling rate than would normally be achievable with the detector array. Since the effect of the finite areas of the detector surfaces simply modifies the spatial frequency spectrum of the object being imaged (see Theorem IV in Section 2.4) we shall, in the following discussion, limit our attention to an array of point detectors. The results obtained hold equally well for the case of detectors having finite areas.

The proposed technique is most easily introduced in a one-dimensional context. In Figure 2.3 is shown a one-dimensional PSF which is sampled by the linear array of point detectors having a sample spacing of Δ . It is assumed that the PSF moves across the detector array with a uniform velocity V and that it does not change shape over the time interval (Δ/V) . At time t_1 , the detectors will measure the values of the PSF labeled by the number one in the Figure (The detectors are assumed to be "turned on" only in a very short time interval centered at t_1). At time $t_2 = t_1 + \Delta/V = t_1 + \Delta/2v$ the detectors will measure the values of the PSF labeled by the number two in Figure 2.3. Because the time increment between the reading at t_1 and t_2 was selected to be $(\Delta/2v)$ the above process is seen to yield equally spaced samples of the PSF with the samples being $\Delta/2$ units apart. It is clear that by choosing smaller values of the time increment even higher sampling rates can result.

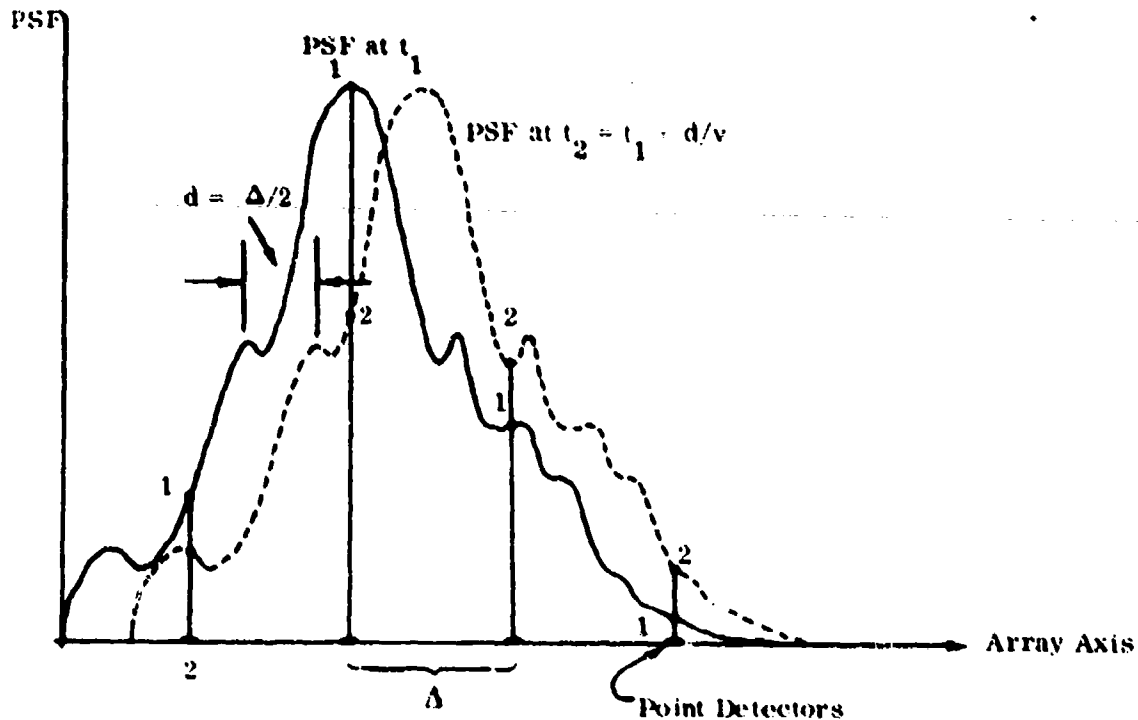


Figure 2.3 Two sets of samples of a PSF obtained at the two times t_1 and $t_2 = t_1 + d/v$. A relative linear velocity of V is assumed to exist between the PSF and the detector array.

An entirely analogous situation as that described above results in the two-dimensional case. In two dimensions, however, it is important that the motion of the PSF at an angle relative to one of the detector axes. This condition is necessary in order to achieve a high sampling rate in two orthogonal directions.

In Figure 2.4 is shown an array of point detectors (large dots) having a sample spacing of Δ . Assume that a PSF were to sweep across this array at a velocity of V and at an angle at 45° with respect to the array's horizontal axis. If the detector array were to make two successive instantaneous measurements separated by a time interval of $(\Delta/\sqrt{2} V)$ seconds apart then the two sets of measurement together would yield samples of the PSF at all sample points shown in the Figure. (The large dots would be the sample positions at one time and the smaller dots the sample positions at the other time.) The overall process would thus be equivalent to sampling the stationary PSF by a regular square array of point detectors having the geometry shown in the box in Figure 2.4.

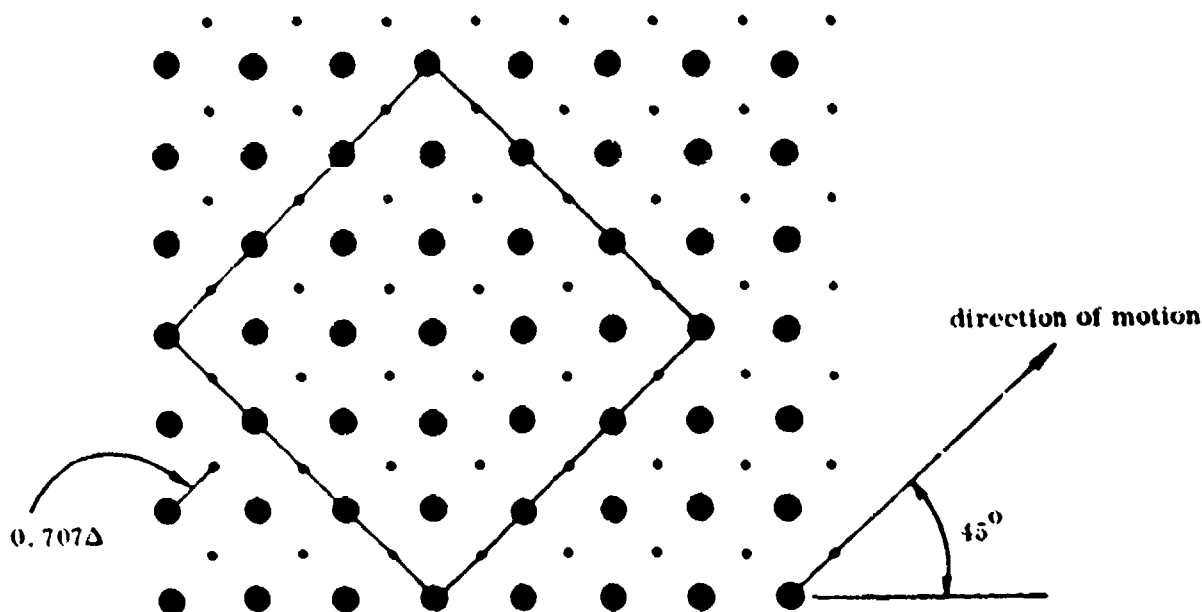


Figure 2.4 Samples of a PSF moving at a uniform velocity at 45° relative to the horizontal axis of an array of point detectors (large dots).

A higher sampling rate than that shown in Figure 2.4 can be achieved if the angle θ between the array axis and the direction of motion of the PSF is smaller than 45° . However, it is easily shown that in order to obtain an equally spaced square matrix of samples this angle can only assume values which satisfy the equation

$$\tan \theta = 1/n; \quad n = 1, 2, 3, \dots \quad (2.22)$$

A plot of the allowable values of θ versus n is shown in Figure 2.5.

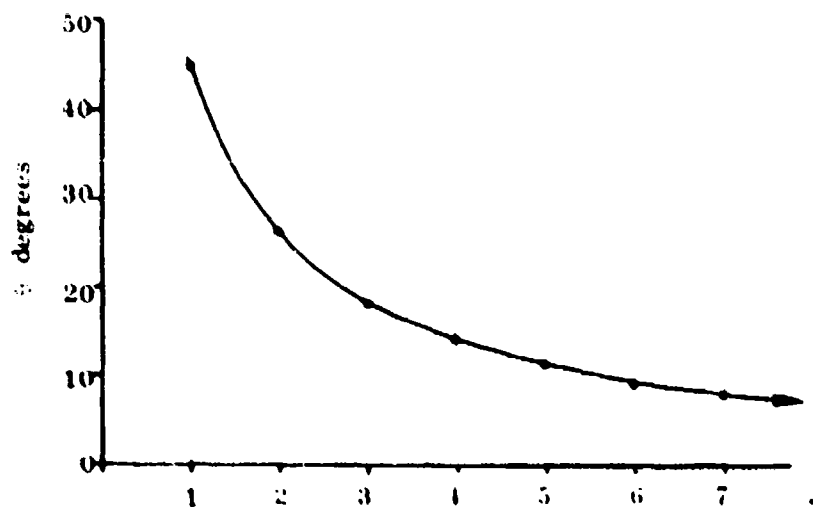


Figure 2.5 Values of θ Satisfying Equation (2.22)

The condition (Eq. 2.22) results from the requirement that the relative motion between the detector array and the PSF be such that at the beginning of a new sampling sequence the relative position of the PSF and the detector array be the same as it was at the initiation of the previous sampling sequence. In the case shown in Figure 2.4 the sampling sequence consisted of two sets of measurements. At the initiation of the sequence the measurement points are indicated by the large dots while at the second sampling time the measurement points would be the small dots. Since the direction of motion is 45° the next sampling time (assuming samples to be taken $(\Delta/\sqrt{2}v)$ seconds apart) would occur again at the locations of the large dots and, thus, the whole process would be repeated.

In Figure 2.6 is shown the case of $n = 2$ or $\theta \approx 26.56^\circ$. The sampling sequence consists of five equally spaced measurements occurring $(1/\sqrt{5}) \Delta/v$ second apart. (In general, the number of measurements in a sampling sequence is $n^2 + 1$ and the time between samples is thus $((1/\sqrt{n^2 + 1}) \Delta/v$ seconds). At the sixth measurement time the relative position between the sampling array and the PSF is the same as at the initiation of the sampling sequence so the whole process repeats after every five measurements.

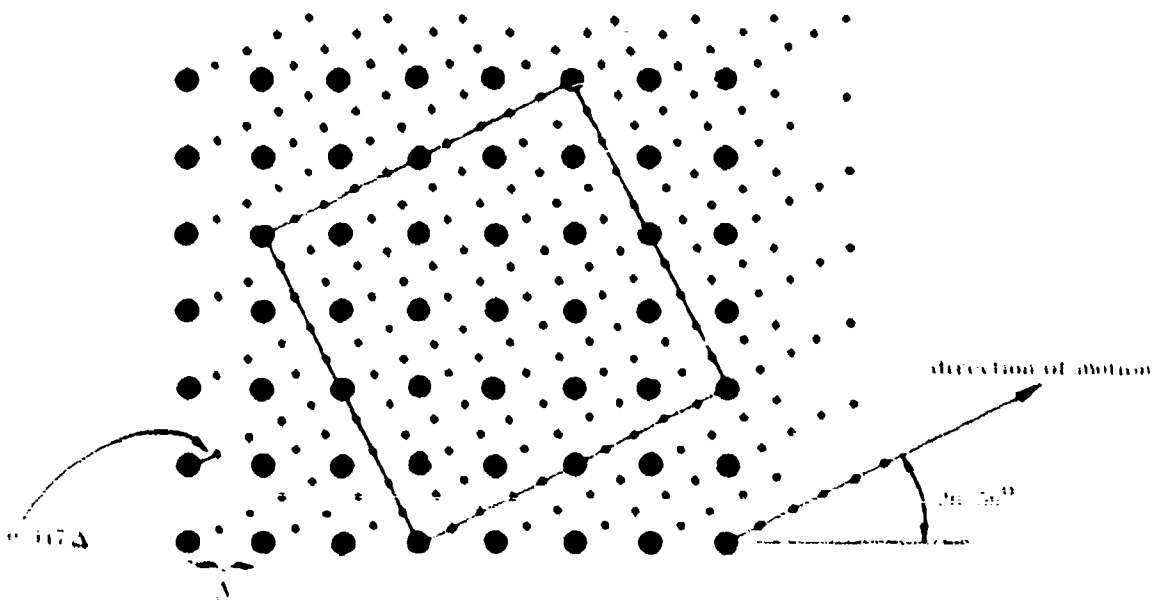


Figure 2.6 Samples of a PSF moving at a uniform velocity at 26.58° relative to the horizontal axis of an array of point detectors (large dots).

From the analysis presented above it is concluded that suitable sampling rates can be achieved if relative image motion exists between the image field and the detecting array. This motion must be at an angle relative to the array axis and the angle must satisfy Equation (2.22) for the resulting sampling matrix to be square and regular.

2.5 THE EFFECTS OF FINITE DETECTOR SIZE AND SCENE SPATIAL FREQUENCY CONTENT ON PHASE RETRIEVAL

One of the major problems encountered with sampled data

imaging systems is aliasing introduced by undersampling in the image plane. In addition, the finite size of each element of an array of detectors has the effect of decreasing the object spectrum at high spatial frequencies and, thus, leads to small signal to noise ratios at high spatial frequencies. Both of these effects have an impact on the process of aberration function estimation. In the following discussion we present the analysis which relates the output of a two-dimensional array of detectors to the image being detected and in the process establish the result that scene spatial frequency content and finite detector size have precisely the same impact on phase retrieval.

We shall assume that the image $I(x,y)$ of an object $O(x,y)$ is sampled by a regular array of identical detectors such as shown in Figure 2.7. In this Figure

$$\begin{aligned} x_n &= n/2f_o \\ y_m &= m/2f_o \end{aligned} \quad (2.23)$$

where $1/2f_o$ is the center to center separation of the detectors and n and m are integers.

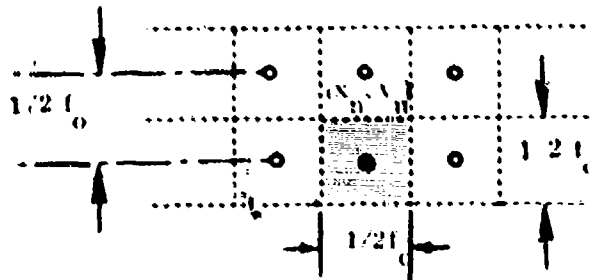


Figure 2.7 Sampling Array Geometry

In the absence of noise the response of each detector will be assumed to be given by

$$i_{n,m} = \iint dx' dy' I(x', y') D(x' - x_n, y' - y_m) \quad (2.24)$$

where $D(x', y') = 0$ if $|x'|$ or $|y'| > 1/4f_o$.

By substituting the Fourier integral representation

$$I(x', y') = \frac{1}{(2\pi)^2} \iint dk_x dk_y \hat{I}(k_x, k_y) e^{i[k_x x' + k_y y']} \quad (2.25)$$

into Equation (2.24) we find that $i_{n,m}$ becomes

$$i_{n,m} = \frac{1}{(2\pi)^2} \iint_{-\infty}^{\infty} dk_x dk_y \hat{I}(k_x, k_y) \tilde{D}(k_x, k_y) e^{i\left[k_x \frac{n}{2f_o} + k_y \frac{m}{2f_o}\right]} \quad (2.26)$$

where

$$\tilde{D}(k_x, k_y) = \iint dx' dy' D(x', y') e^{-i[k_x x' + k_y y']} \quad (2.27)$$

and

$$\begin{aligned} \hat{I}(k_x, k_y) &= \iint dx' dy' I(x', y') e^{-i[k_x x' + k_y y']} \\ &= \hat{O}(k_x, k_y) \text{OTF}(k_x, k_y) \end{aligned} \quad (2.28)$$

with $\hat{O}(k_x, k_y)$ being the spatial frequency spectrum of the object being imaged and $\text{OTF}(k_x, k_y)$ the Optical Transfer Function of the imaging system. Finally, on substituting Equation (2.28) into Equation (2.26) we find that

$$i_{n,m} = \iint_{-\infty}^{\infty} dk_x dk_y \tilde{O}(k_x, k_y) \text{OTF}(k_x, k_y) e^{i \left[k_x \frac{n}{2f_o} + k_y \frac{m}{2f_o} \right]} \quad (2.29)$$

where

$$\tilde{O}(k_x, k_y) = \tilde{D}(k_x, k_y) \tilde{O}(k_x, k_y) \quad (2.30)$$

We conclude from Equation (2.29) that the effects of finite detector size as manifested in the detector frequency response function $\tilde{D}(k_x, k_y)$ and object spatial frequency content $\tilde{O}(k_x, k_y)$ have entirely equivalent effects on the output $i_{n,m}$ from an element of the detector array. This "equivalence property" allows us to conceptually replace an actual detector array by an array of point detectors so long as we also replace the actual object spectrum $\tilde{O}(k_x, k_y)$ by the modified spectrum $\tilde{O}(k_x, k_y)$ as defined in Equation (2.30). This equivalence is stated precisely in the following Theorem:

Theorem IV

Let the image of an object having a spatial frequency spectrum $\tilde{O}(k_x, k_y)$ be sampled by a regular array of identical detectors having a center to center separation of $1/2f_o$ and frequency response function $\tilde{D}(k_x, k_y)$. Then the output from this detector array is precisely the same as would be obtained from detecting the image of an object having the spatial frequency spectrum $\tilde{O}(k_x, k_y) = \tilde{O}(k_x, k_y) \tilde{D}(k_x, k_y)$ by a regular array of point detectors having the same center to center separation (i.e., $1/2f_o$).

Proof of Theorem

The proof of the Theorem follows at once from Equations (2.29) and (2.30).

Comments

The above result is extremely important in that it allows us to always deal with an array of point detectors without any loss of generality. Because of this, for example, the analysis presented in the preceeding section is directly applicable to arrays of non-point detectors. In addition, it shows that the problem of phase retrieval from a star object using a regular array of non-point detectors is precisely the same as the problem of phase retrieval from non-point objects using an array of point detectors. This later equivalence turns out to be extremely important in the simulation studies presented in Chapter 4.

2.6 THE EFFECT OF NON-MONOCHROMATIC RADIATION ON THE POINT SPREAD FUNCTION

In order to determine the effect of polychromatic radiation on the process of phase retrieval, a number of (one-dimensional) multi-spectral PSF's and OTF's were generated, having various amounts of coma and defocus. The input spectra for these PSF's and OTF's contained three to five wavelengths and had a total width of 10% to 20% of the central wavelength. The results indicate that the introduction of many spectral components affects the detailed structure of the PSF but not its general shape. Another way of putting this is that the OTF is affected mainly at the higher spatial frequencies.

Method of Calculation

Let $P(x, \lambda)$ be the point spread function at wavelength λ at point x . Then the multi-spectral PSF is given by

$$P(x) = \sum_{\lambda} c_{\lambda} P(x, \lambda) / \sum_{\lambda} c_{\lambda} \quad (2.31)$$

where the quantities c_{λ} represent the relative weights of the different wavelengths. For each wavelength $P(x, \lambda)$ is given by

$$P(x, \lambda) = \left| \int d\alpha f(\alpha) e^{-2\pi i \frac{\alpha x}{2\lambda F\#}} e^{\frac{2\pi i}{\lambda} W(\alpha)} \right|^2 \quad (2.32)$$

where $F\#$ = the F number of the system

α = the aperture coordinate/the aperture radius

$f(\alpha)$ = the pupil function of the system

$\frac{W(\alpha)}{\lambda}$ = the total phase shift due to the wave aberration function $W(\alpha)$ at wavelength λ

It is important to note that it is tacitly assumed in this analysis that the wave aberration function $W(\alpha)$ is independent of wavelength. Such an assumption is valid for optical imaging systems employing high quality mirrors such as is envisioned for HALO.

The plots presented in Figure 2.8 through 2.16 show the total phase shift at the central wavelength; i.e.,

$$\frac{W(\alpha)}{\lambda} = \sum_n \Lambda_n \alpha^n, \quad (2.33)$$

the multi-spectral (polychromatic) PSF, and the modulus and phase of the polychromatic OTF for various choices of the expansion coefficients (aberrations) Λ_n and for various wavelength spectra. Figures 2.8 - 2.10 show line spread functions and OTF's calculated for an aberration of one wave of

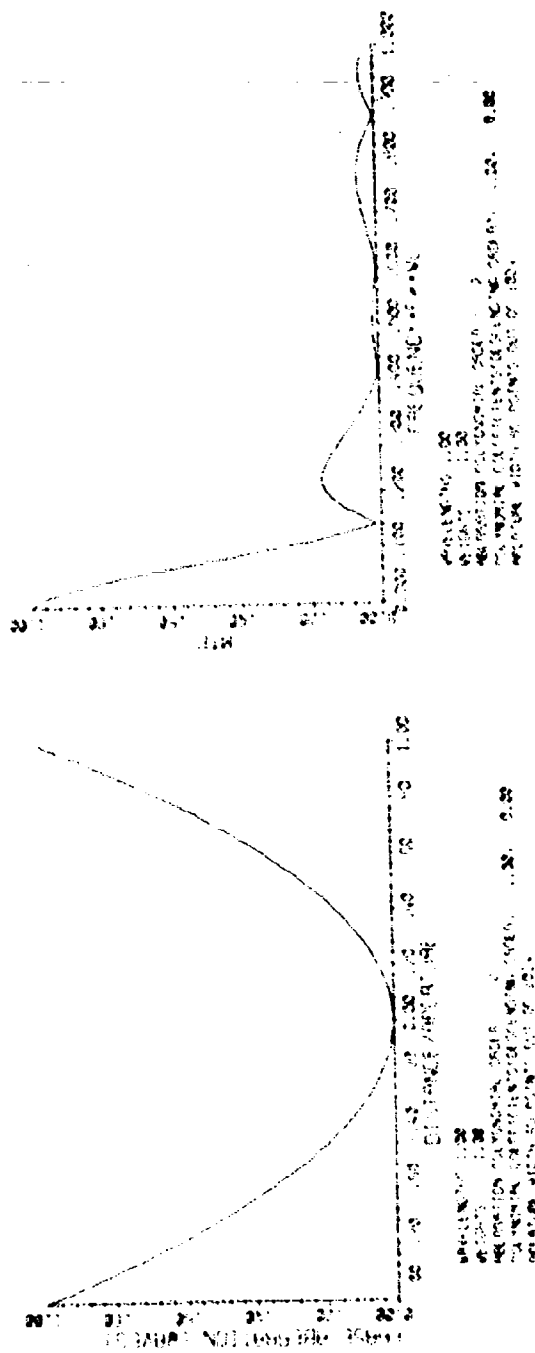


Figure 2.8 One Wave of Defocus at a Single Wavelength

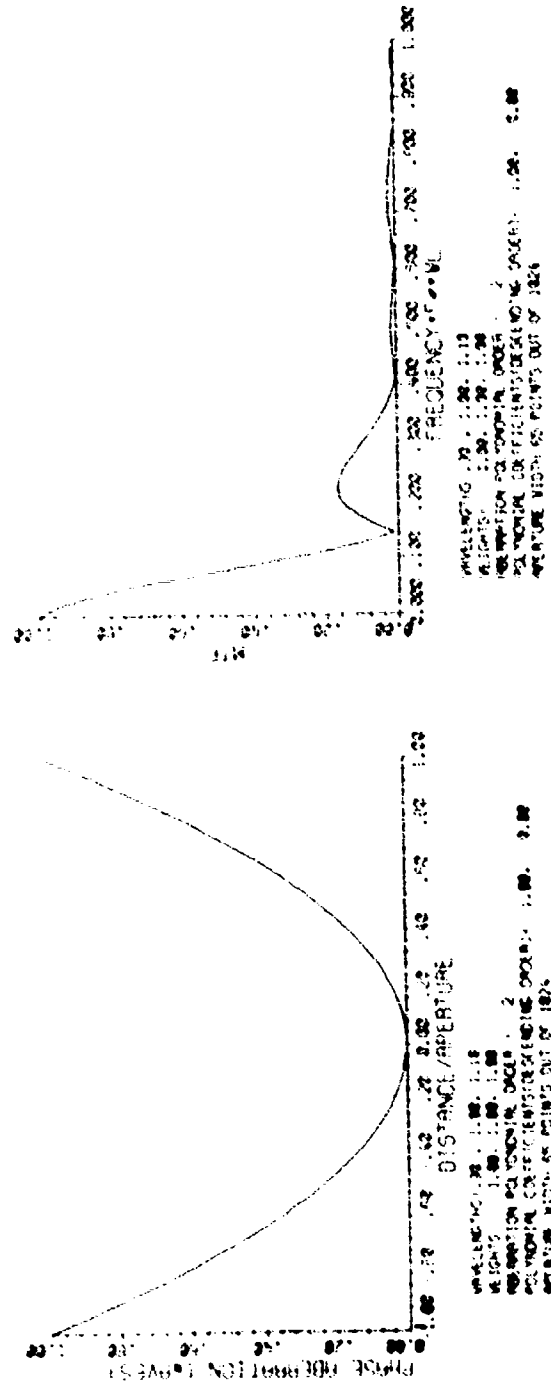
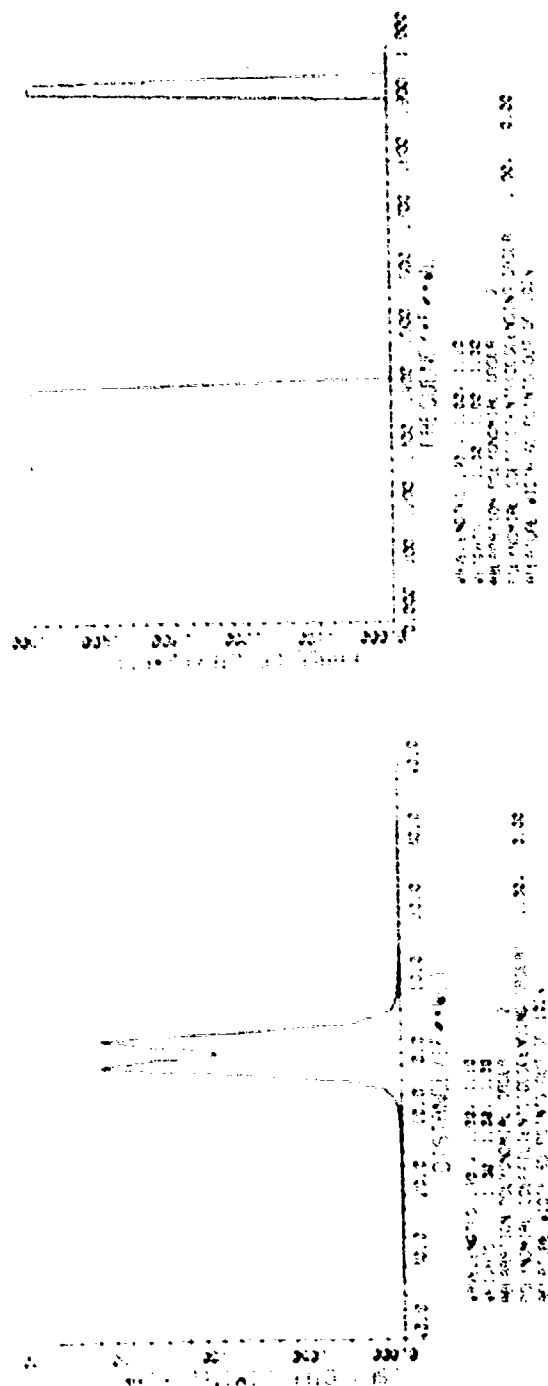


Figure 2.9 Polychromatic Case For One Wave of Defocus

36

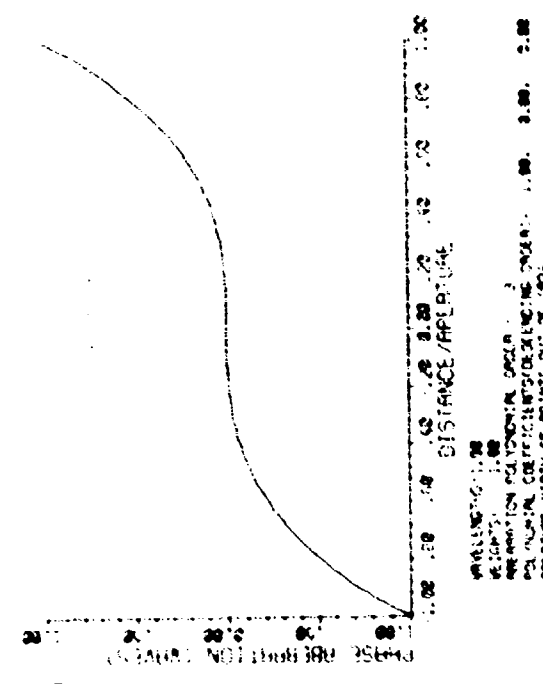
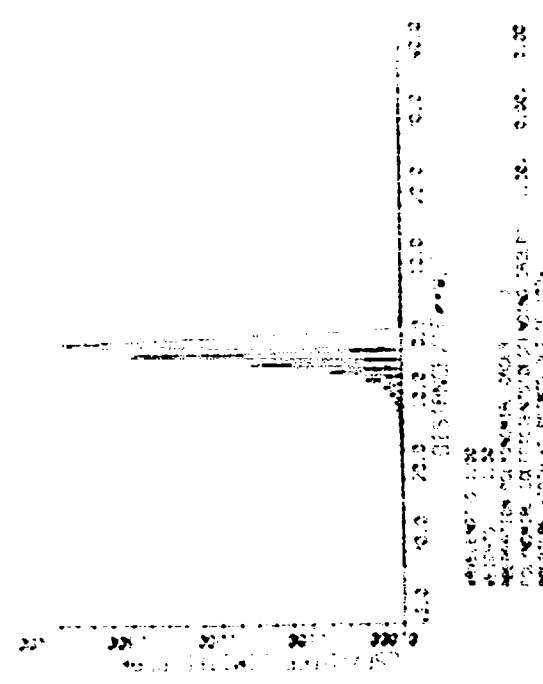
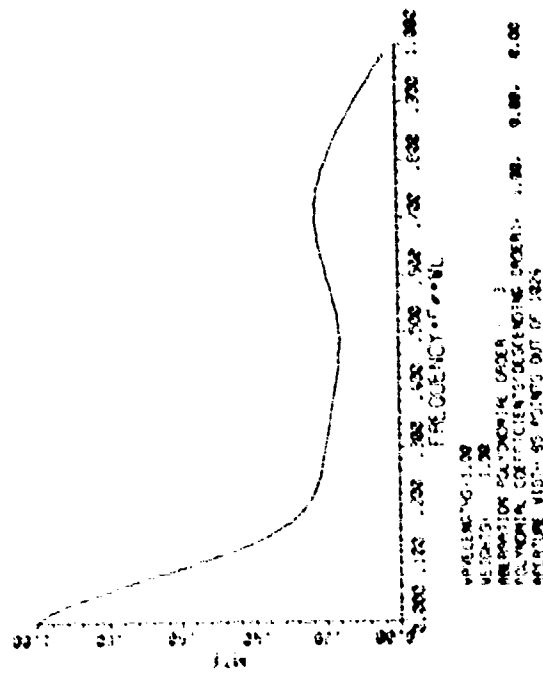
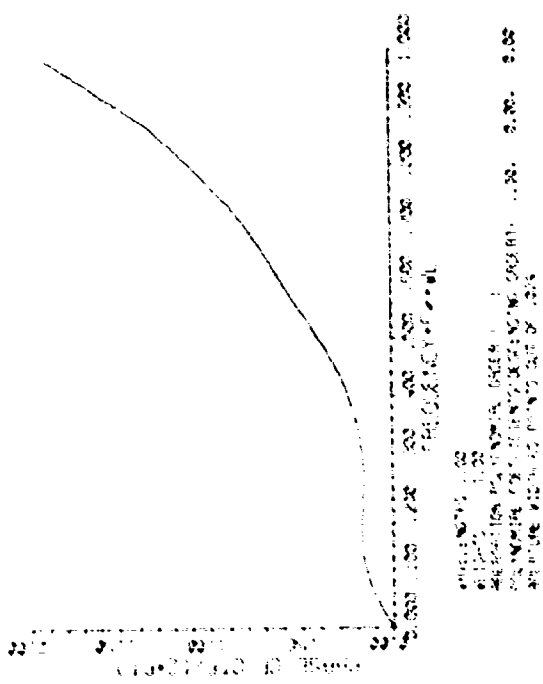


Figure 2.11 One Wave of Coma At A Single Wavelength

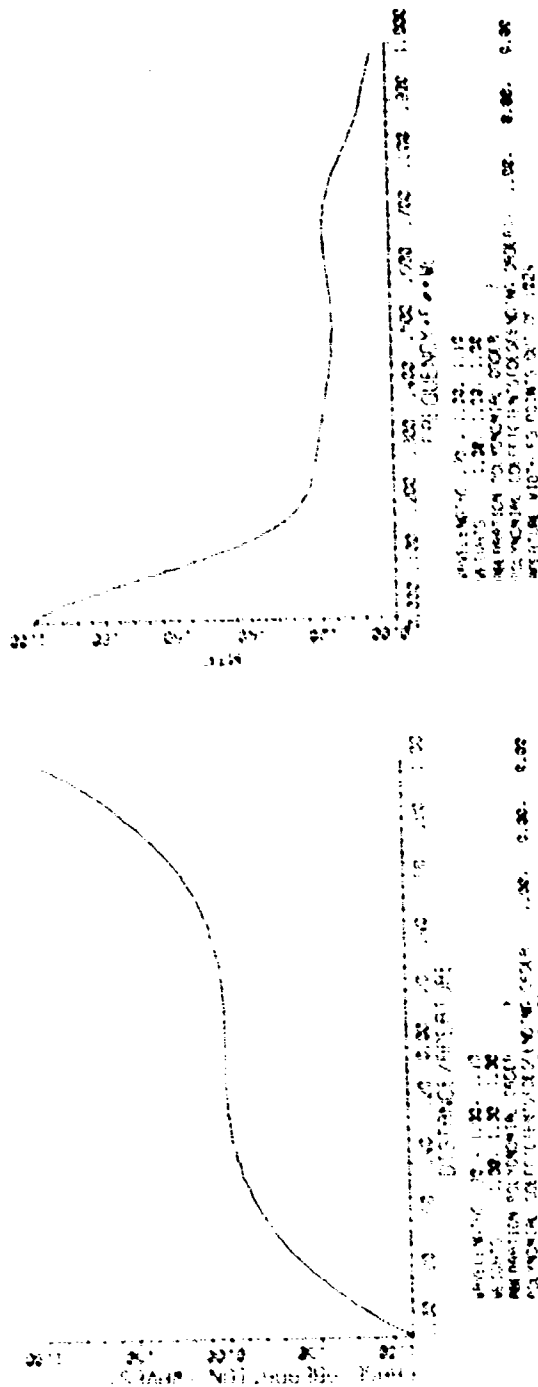


Figure 2.12 polychromatic Case For One Wave of Coma

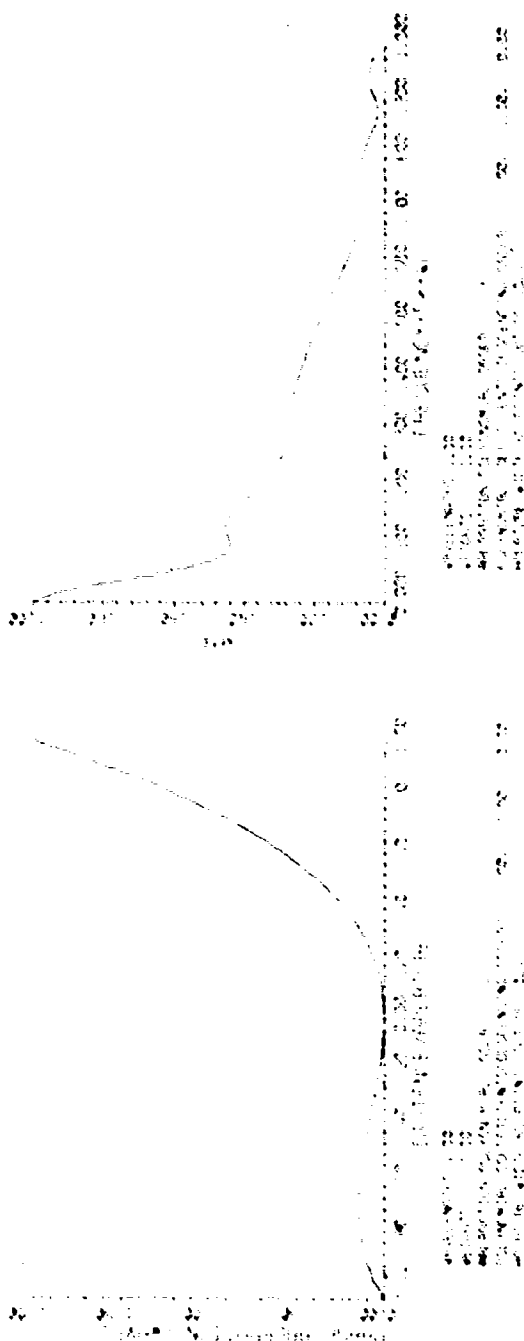
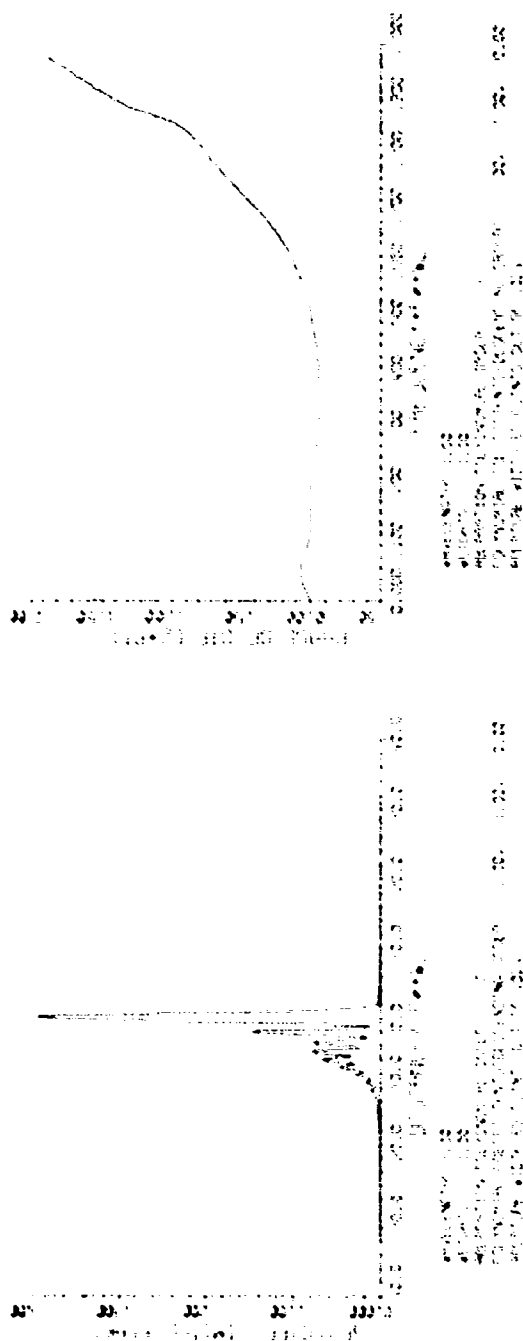


Figure 2.14 One Wave of Defocus Plus One Wave of Coma at a Single Wavelength

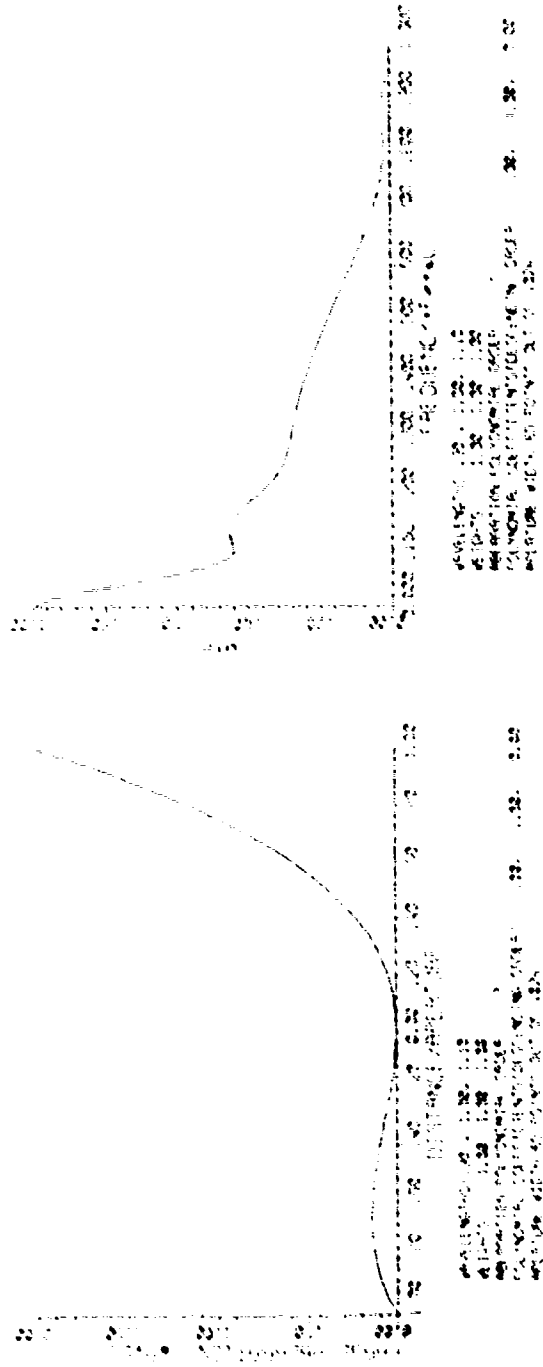


Figure 2.15 Polychromatic Case For One Wave of Defocus Plus One Wave of Coma

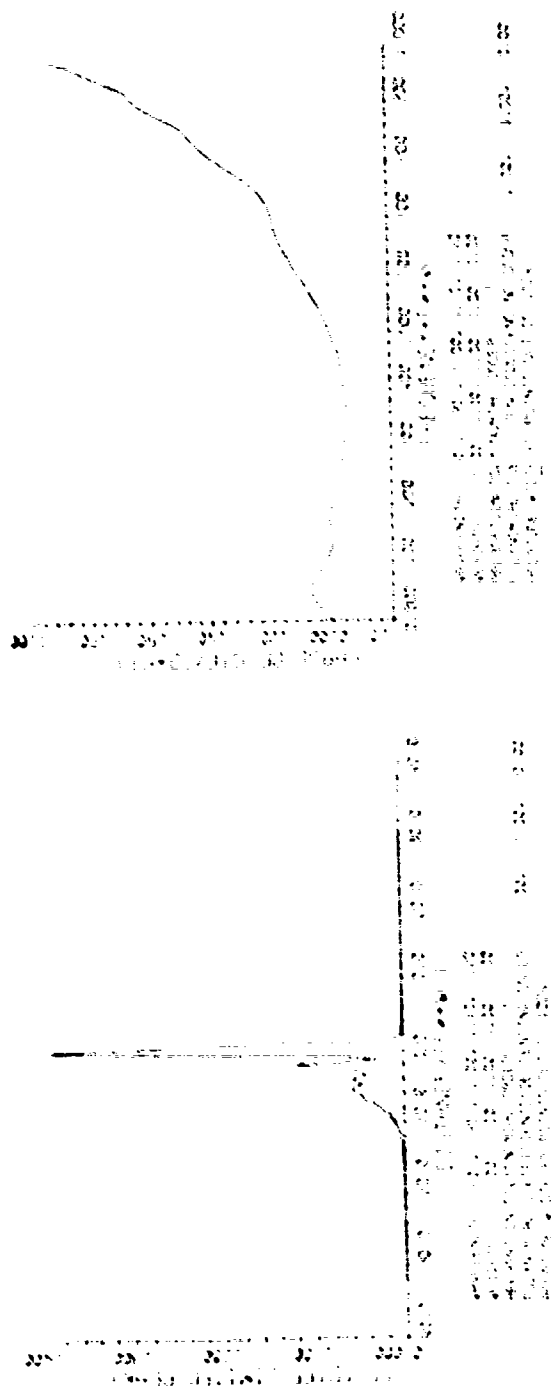


Figure 2.16 Polychromatic Case For One Wave of Defocus Plus One Wave of Coma

defocus. The first figure shows the monochromatic case, while the next two figures show the case of three wavelengths with a total spread of $\pm 10\%$, and five wavelengths with a total spread of $\pm 20\%$. Figures 2.11 - 2.13 and Figures 2.14 - 2.16 show a similar series for one wave of coma, and for one wave of coma plus one wave of defocus.

As mentioned above, these results indicate that the polychromatic and monochromatic OTF's are quite similar, differing mainly at high spatial frequencies. In this sense the effect of polychromatic radiation on the process of wave aberration estimation is quite similar to the effect of detector noise on this process. Because the phase retrieval algorithms appear to be highly insensitive to moderate amounts of detector noise, it is reasonable to conclude that they will likewise be insensitive to the effect of moderate amounts of spectral broadening in the detected radiation. This hypothesis can, of course, be tested in computer simulations although it was decided that such simulations were not warranted within the current effort.

3.0 THE GERCHBERG-SAXTON ALGORITHM

The Gerchberg-Saxton (G.S.) algorithm is a method which permits determination of wavefront aberrations from measured point spread functions by the use of repeated Fourier transforms. The overall operation of the algorithm is shown in Figure 1.4 of Chapter 1 and in more detail in Figure 3.1 below. It basically consists of going back and forth between the generalized pupil function and the coherent spread function by means of Fourier transforms, each time keeping the phase part of the function and replacing the magnitude by the known correct magnitude, which is the square root of the measured point spread function for the coherent spread function, and unity for the generalized pupil function. There is no proof that the algorithm must converge, or that if it does, it will converge to the correct aberration function. Clearly one possible mode of convergence, which is the desired result, is that W becomes equal to the actual wave aberration, and that $|CSF|^2$ is exactly equal to the measured h . If a different W were found such that we still had $|CSF|^2 = h$, then this would be an example of non-uniqueness. This has never occurred in our simulations, although we cannot prove its impossibility. A third possibility of convergence is one in which neither W nor CSF ever reach the proper values, but the estimates remain unchanged each time around the loop. This last possibility in fact seems to be a common occurrence although we are unable to state if the algorithm has truly converged to a poor result, or is merely changing at a very slow rate.

Previous work performed prior to this contract extensively tested the G.S. algorithm in the one-dimensional case with excellent results. ⁽⁷⁾ No examples of false convergence were

7. A.J.Devaney, R.A.Gonsalves and R.Chidlaw, "Application of phase retrieval techniques to adaptive imaging systems," J. Opt. Soc. Am. (A) 67, 1422 (1977).

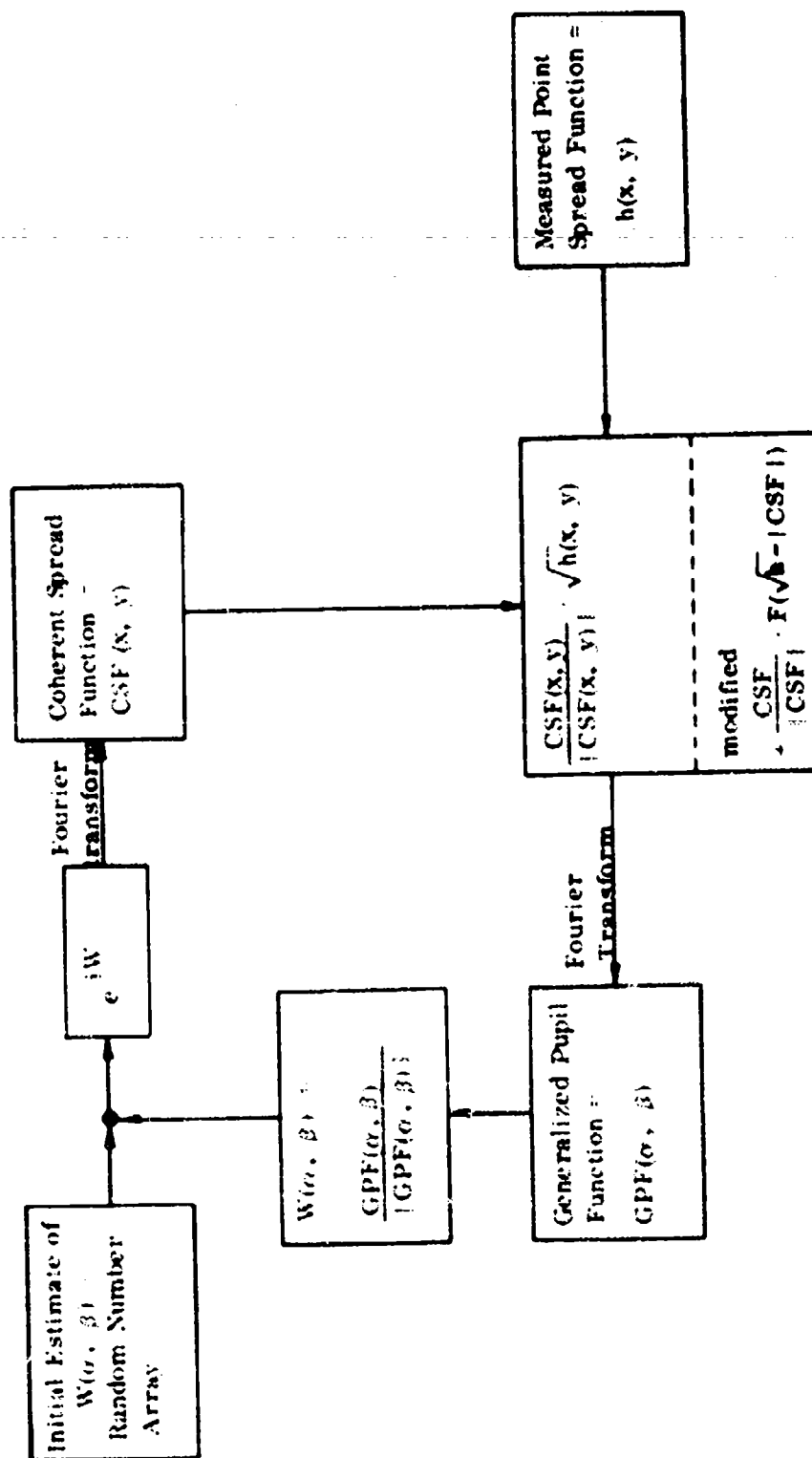


Figure 3.1 Gerchberg-Saxton Phase Retrieval Algorithm

observed. The two-dimensional G.S. algorithm was tested on this contract for a number of cases. For some initial (random) estimates of the phase, the procedure worked well. For others, convergence is extremely slow (perhaps on the order of 10,000 iterations) if indeed it would even be reached. A convergence acceleration technique inspired by Fienup⁽⁸⁾ yielded marginal improvement in both the fast converging and slow converging cases; but the slow converging cases remained too slow for use. The fast converging cases can be driven into instability by too much of this procedure.

Table 3.1 is a list of results. The amount of aberration is expressed in radians, in terms of: defocus - $P_3 r^2$, third-order spherical - $P_4 r^4$, and third-order astigmatism - $P_5 r^2 \cos \theta$. The initial estimate of the phase aberration is chosen as an array of random numbers. The RMS value of the array is adjusted depending on the Strehl ratio of the PSF. A linear tilt is added if the peak value of the PSF is not at the array center. The random numbers are generated by a system routine on the PDP 11/70 called RAN. It requires two random number "seeds" to determine a particular pseudo-random sequence. Three sets of seeds were used, as listed in Table 3.2.

8. J.R. Fienup, "Reconstruction of an object from the modulus of its Fourier transform", J. Opt. Soc. Am. (A) 67, 1389 (1977)/

TABLE 3.1

Results of Tests of the Two-Dimensional
Gerchberg-Saxton Algorithm

Case	Aberration (radians)	Random Number Seeds	Iterations Performed	N, N2	Acceleration NF F	Results
1	$P_3 = 3$	A	20	16, 32		good
2			30			good
3			50			very good
4		B	50			bad
5		A	50		0 0.01	very good
6			50		0 0.02	very good
7			50		0 0.05	bad
8			50		0 0.2	bad
9			20		10 0.05	bad
10			40		15 0.05	good
11	$P_3 = 1$	B	50	8, 32		bad
12		A	16	16, 32		fair
13		B	80			bad
14		C	80			bad
Case	Aberration (radians)	Random Number Seeds	Itera- tions Per- formed	N, N2	Accelera- tion	Results Start Min. Finish
15	$P_3 = 3$	A	40	16, 32	I	301.3 11.1
16					II	9.2
17					III	7.1
18					IV	4.7
19					V	2.7
20					VI	1.3
21					XII	0.77
22					VII	8.8 41
23					VIII	6.5 26.9
24					IX	9.0 37.2
25					XI	6.4 31.5

TABLE 3.1 (Continued)

Case	Aberration (radians)	Random Number Seeds	Itera- tions Per- formed	N, N2	Accelera- tion N NF	Results Start Min. Finish
26					X	3.7 8.3
27		B	50		XII	315.0 112.0 115.0
28	$\left\{ \begin{array}{l} P_3 = 2 \\ P_4 = 4 \\ P_5 = 5 \end{array} \right\}$	A	40	16,32		bad
29			100		60 0.03	bad
30			300		X	402 to 133 (de- creasing very slowly)
31			40		XV	402 to 178 (bad)
32			40		XIII (very strong)	402 to 169 (bad)

TABLE 3.2 RANDOM NUMBER SEEDS

A	11427	9223
B	2689	8957
C	4567	13879

The lens aperture is a circle of maximum diameter which will fit into an $N \times N$ array of points. This is buffered out to $N_2 \times N_2$ with zeros. If N_2 is twice N , the resulting PSF is sampled at the Nyquist rate.

The column labeled "acceleration" refers to the parameters using in attempting to accelerate convergence. If left blank, the original G. S. algorithm was used. In the "results" column, a judgment of how well the first aberration estimate compares with the actual input aberration is listed. Eventually a measure of the error between the original and estimated PSF's was added to provide a more exact measure.

Cases 1, 2, and 3 show the effect of increasing the number of iterations of the G.S. algorithm, which is an improvement in the estimate of the phase aberration. A different random number seed yields an estimate that bears no relation to the actual aberration, in Case 4. Other results show that this case has not really converged but is slowly changing.

Cases 12, 13, and 14 have a smaller amount of aberration. With the random number seed in Case 12, after only 16 iterations, the final estimate is definitely headed for convergence at the actual starting aberration. With different random numbers, even 80 iterations yields bad results. In Case 11, the effective sampling of the point spread function has been doubled, by reducing the number of points over the aperture to 8, but this case still failed to converge.

Cases 5 through 10 illustrate the first attempt at accelerating the algorithm. The G. S. algorithm was modified by the addition of a term $F \cdot (\sqrt{h} - \text{CSF})$, in the box labelled "modified" in Figure 3.1. This term causes the CSF to be corrected not to the known CSF modulus, \sqrt{h} , but rather shifted by an amount proportional to the difference between the estimate, $|\text{CSF}|$, and the desired quantity \sqrt{h} , but in the opposite direction. The parameter F denotes the strength of this correction. This new term has not altered what may be termed an eigenfunction of the loop; if a W which exactly yields a point spread function h is put into the loop, it will return unchanged. Thus any function W at which the old algorithm would converge will still be such a function in the new algorithm. It was hoped that this would eliminate the false convergence problems.

In Cases 5 through 8, F was set equal to the value specified in the table from the beginning of the algorithm. For low F 's, this converged; for large F 's, the algorithm did not. By waiting for 10 iterations before applying an F of 0.05, there is still no convergence in Case 9. But in Case 10, applying $F = 0.05$ after 15 iterations, the algorithm does converge. It was then decided to make the value of F , at any one iteration, depend on the difference between \sqrt{h} and $|\text{CSF}|$. An error was defined by

$$\text{ERROR} = \left| \sqrt{h} - |\text{CSF}| \right| \quad (3.1)$$

where the sum extends over the entire PSF plane. A series of different F functions were tried, as defined by Table 3.3. In all of these, the smaller the error becomes, the larger the value of F is. In Cases 15 to 21, increasing the strength of F resulted in faster convergence. In Cases 22 through 26, with stronger F 's, the error decreased to a certain point and then began to rise. A final error of less than 20 is indicative of

a very good estimate of the phase aberration. Although F function XII worked well with random number seed A, in Case 27 with random number seed B, convergence was not obtained.

Cases 28 to 32 are with a larger amount of aberration. Nothing worked for these cases, including a very large number of iterations, and a very strong F function, which would no doubt have produced an instability in the previous cases. Case 4 was repeated with 1000 iterations, which is nearing the limit of reasonable computation times on our 11/70, with no improvement. A final algorithm was tried in which every time the error, as defined by Equation (3.1) began to increase, a new random number set between 0 and 2π was added to the current estimate of W and the algorithm was allowed to continue. After 1000 iterations of this, good convergence was still not obtained.

The G. S. algorithm is quite attractive from the standpoint of implementation into Special Purpose hardware, and the overall simplicity of the method, but unless the problem of false convergence is solved, it will not be useable.

Total Error	I	II	III	IV	V	VI	VII	VIII	IX	X	XI	XII	XIII	XIV
200	0.00	0.00	0.00	0.00	0.00	0.00	0.00	0.00	0.00	0.00	0.00	0.00	0.00	0.00
180	0.00	0.00	0.00	0.00	0.00	0.00	.01	.01	.01	.01	.01	.01	.50	.05
140	.01	.01	.01	.01	.01	.01	.02	.02	.02	.02	.02	.02	.80	.10
120	.015	.02	.02	.025	.03	.03	.04	.04	.04	.04	.04	.03	.95	.15
110	.015	.02	.02	.025	.03	.03	.11	.11	.11	.55	.10	.04	1.20	.20
100	.02	.03	.035	.04	.06	.07	.18	.20	.20	.75	.15	.09	1.30	.20
90	.03	.04	.05	.065	.09	.11	.30	.40	.40	1.0	.25	.15	1.30	.40
80	.04	.05	.07	.09	.13	.15	.45	.55	.55	1.1	.35	.21	1.30	.55
70	.05	.065	.09	.11	.17	.21	.65	.75	.75	1.2	.50	.29	1.30	.75
60	.06	.08	.11	.14	.22	.29	.90	1.05	1.05	1.3	.70	.38	1.30	1.00
50	.07	.10	.13	.17	.28	.38	1.15	1.25	1.25	1.3	.90	.50	1.10	1.10
40	.08	.12	.15	.22	.35	.50	1.35	1.35	1.40	1.35	1.1	.60	1.20	1.20
30	.09	.14	.20	.30	.43	.60	1.50	1.40	1.50	1.35	1.35	.75	1.30	1.30
20	.10	.16	.25	.40	.52	.75	1.65	1.45	1.60	1.40	1.60	.90	1.30	1.30
10	.12	.18	.30	.50	.63	.90	1.80	1.50	1.65	1.60	1.85	1.00	1.35	1.35
5	.12	.20	.35	.60	.75	1.05	1.80	1.55	1.70	1.80	2.1	1.15	1.35	1.35
3	.15	.25	.35	.60	.75	1.05	2.0	1.60	1.80	2.00	2.5	1.35	1.40	1.40
2	.20	.25	.40	.70	.90	1.20	2.0	1.80	2.0		3.0	1.55	1.60	1.60
1	.20						2.0	2.0	2.2		3.5	1.90	1.80	1.80
							2.5	2.2	2.5		5.0	2.50	2.00	2.00

Table 3.3 Parameters for Convergence Acceleration

4.0 THE DEVANEY ALGORITHM

4.1 NOISE-FREE, POINT DETECTOR RESULTS

The definition of the Devaney-Gonslaves phase-retrieval algorithm is presented in the proprietary Appendix A. In this chapter we merely present results. The results are repeated in the Appendix with additional discussions concerning the algorithm.

Figure 4.1, 4.2, and 4.4 show, respectively, contour plots of the original simulated phase aberration across an aperture, the aberration estimated by the program, and the residual aberration (the initial as corrected by the estimate). The values at the contour lines are indicated by the symbols in the table to the right of the graph. All values are in terms of waves. The aperture coordinates X and Y are in terms of the reduced coordinates. The aperture itself is the best circle which fits inside the square array; since the square array is sampled on only a 9x9 mesh, the aperture is not a perfect circle. On Figure 4.4, there is little residual aberration; less than a deviation of 0.1 waves to either side of zero, which is the minimum contour step value used by the contouring program. Figures 4.3 and 4.5 show the MTF's corresponding to the initial aberration and the residual aberration. The latter MTF is essentially diffraction limited; the deviation from circularity near the center is due to the coarse grid on which the MTF is evaluated. Only half of the MTF is plotted since it is symmetric under the transformation $(x, y) \rightarrow (-x, -y)$. The coordinates x and y on the graph represent normalized spatial frequencies; a value of 1 indicates a frequency of $\lambda F^{\#}$. Figures 4.6 through 4.10 show contour plots of the results for another case. Yet another case is presented in Figures 4.11 through 4.15. This case had larger aberrations and took longer to complete than the previous cases.

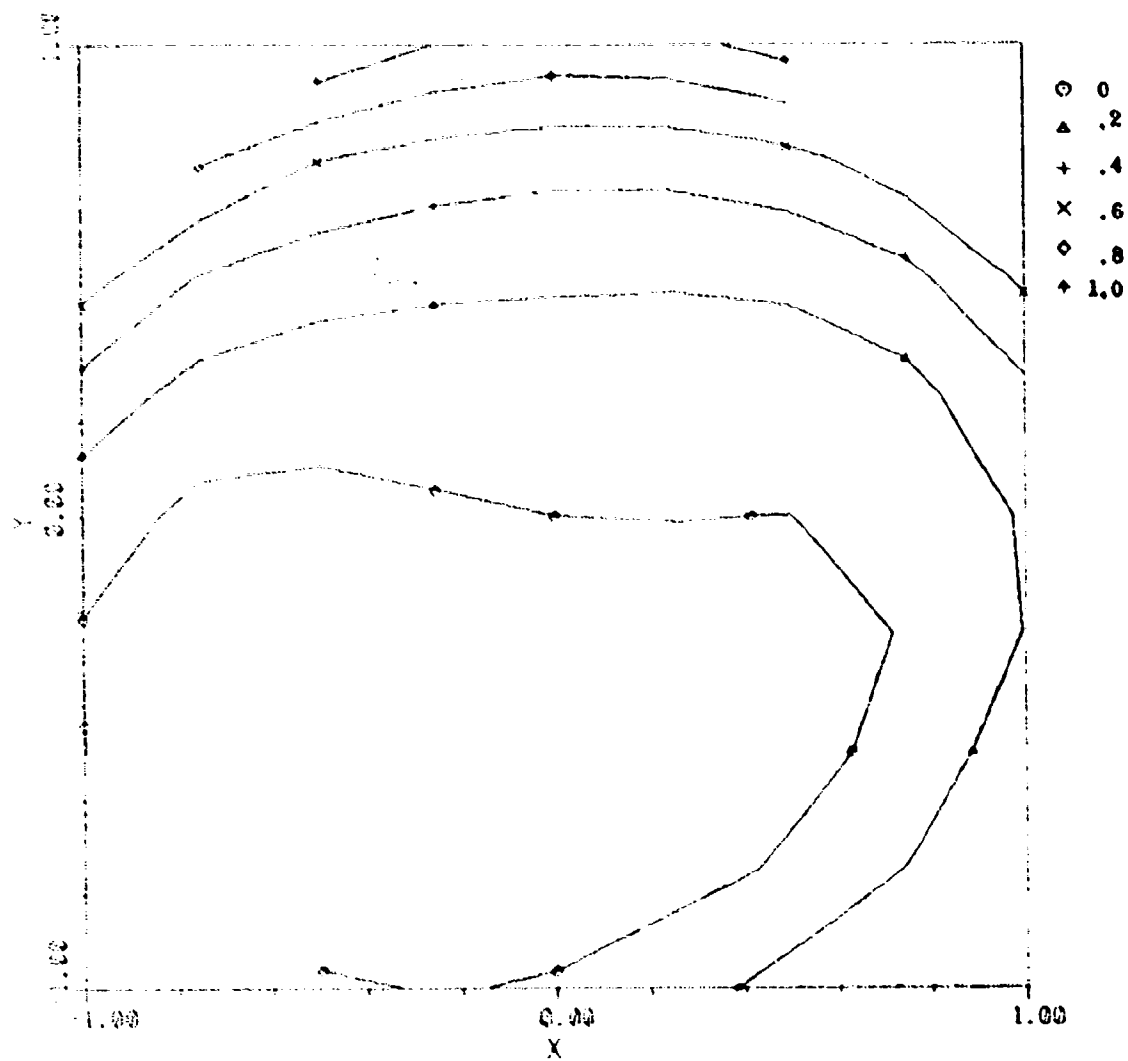


Figure 4.1 Contour Plot of Initial Phase Aberration Function - Test 5

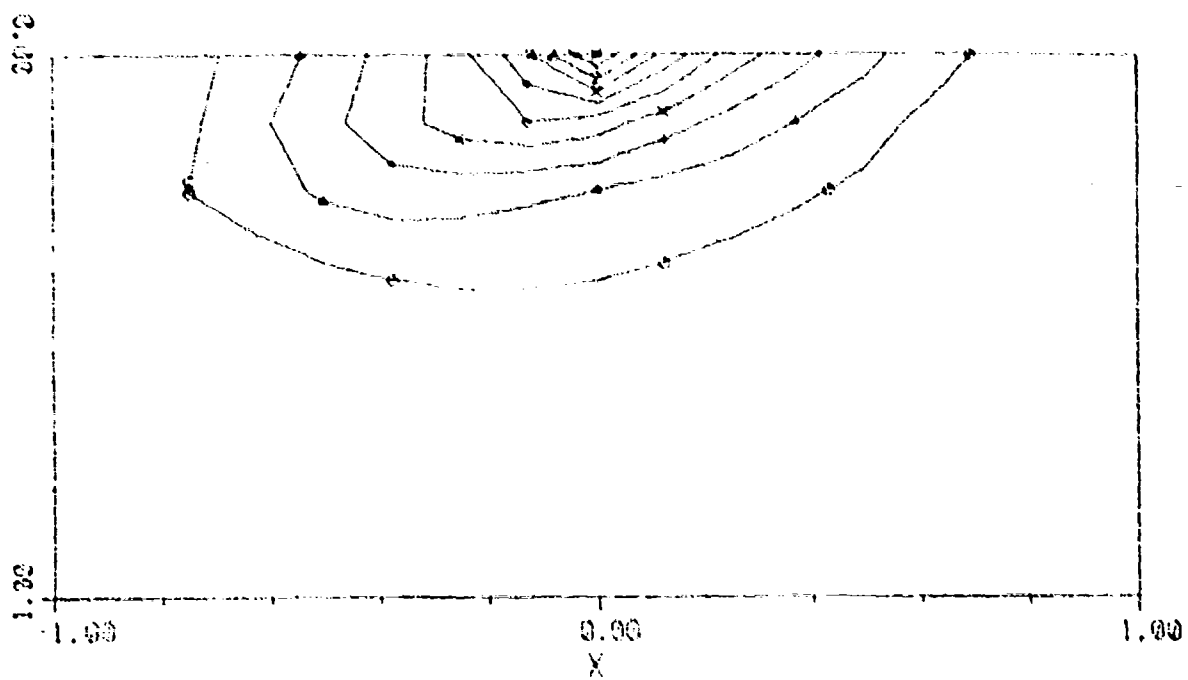


Figure 4.2 Contour Plot of Initial MTF - Test 5

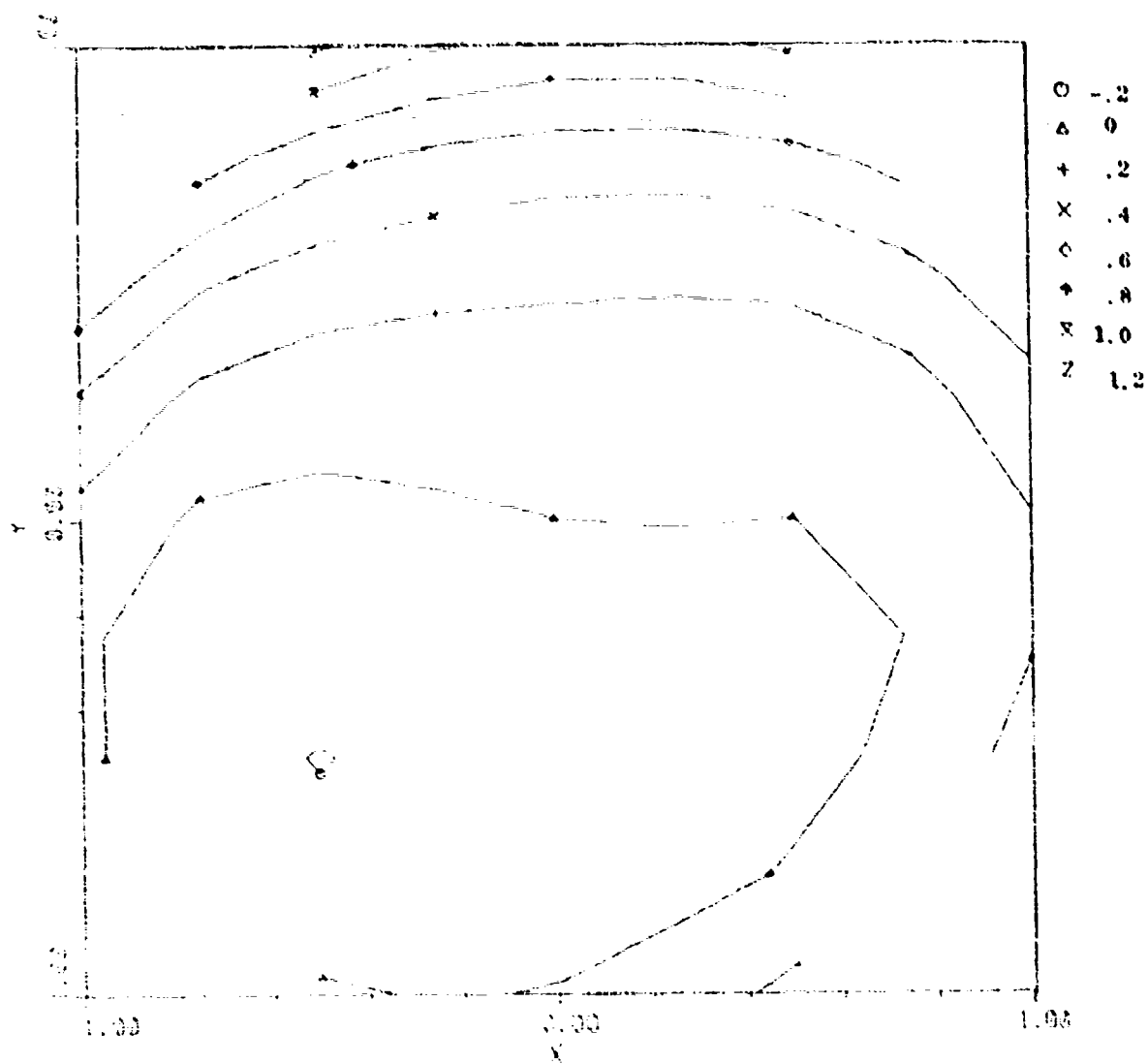


Figure 4.3 Contour Plot of Estimated Phase Aberration Function - Test 5

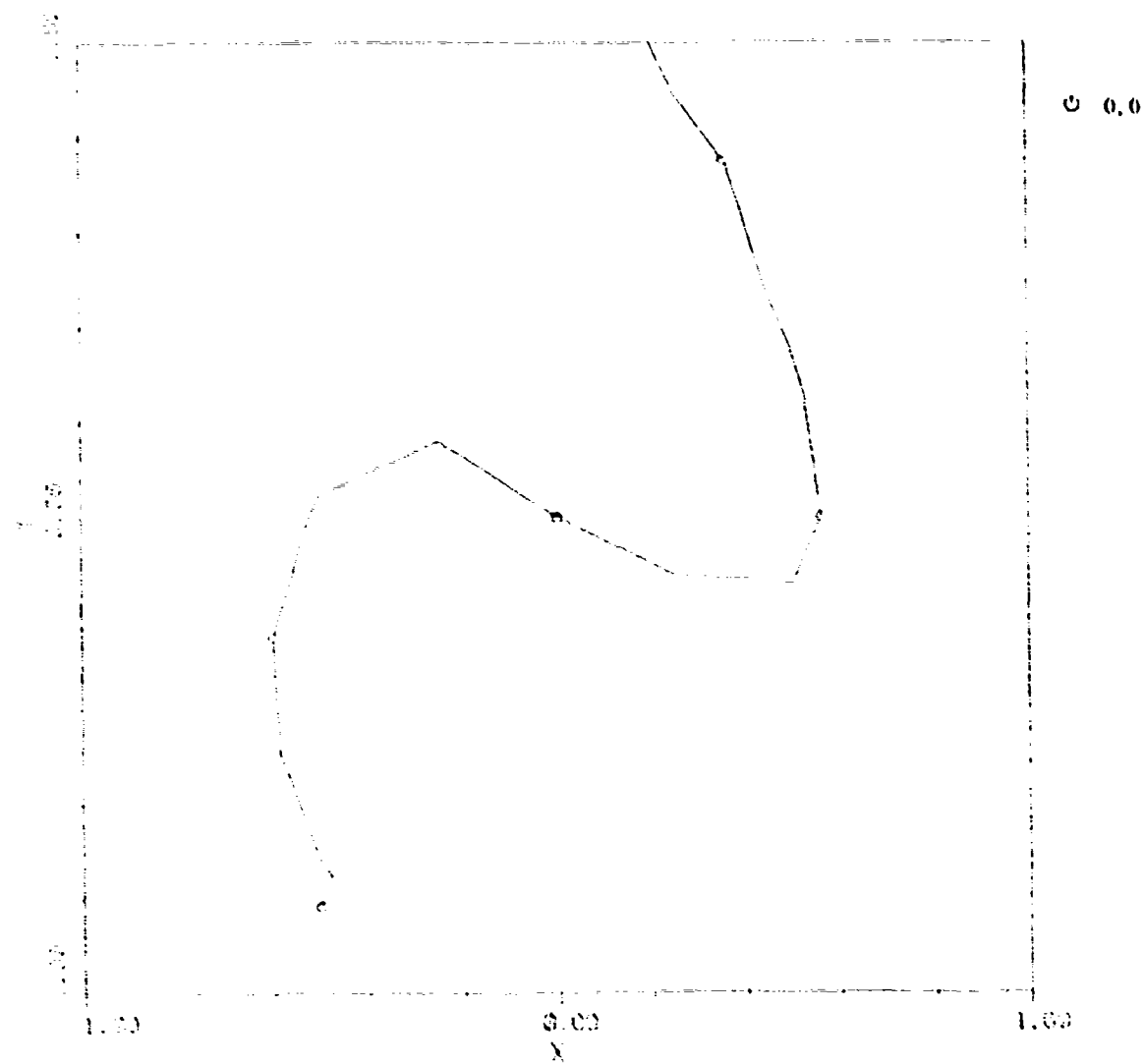
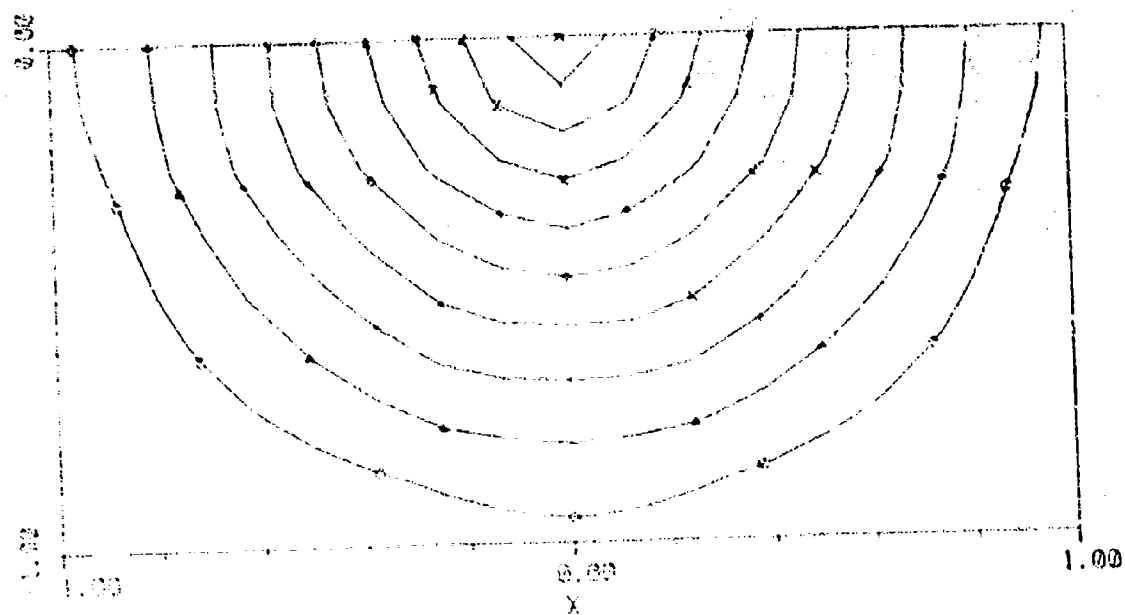
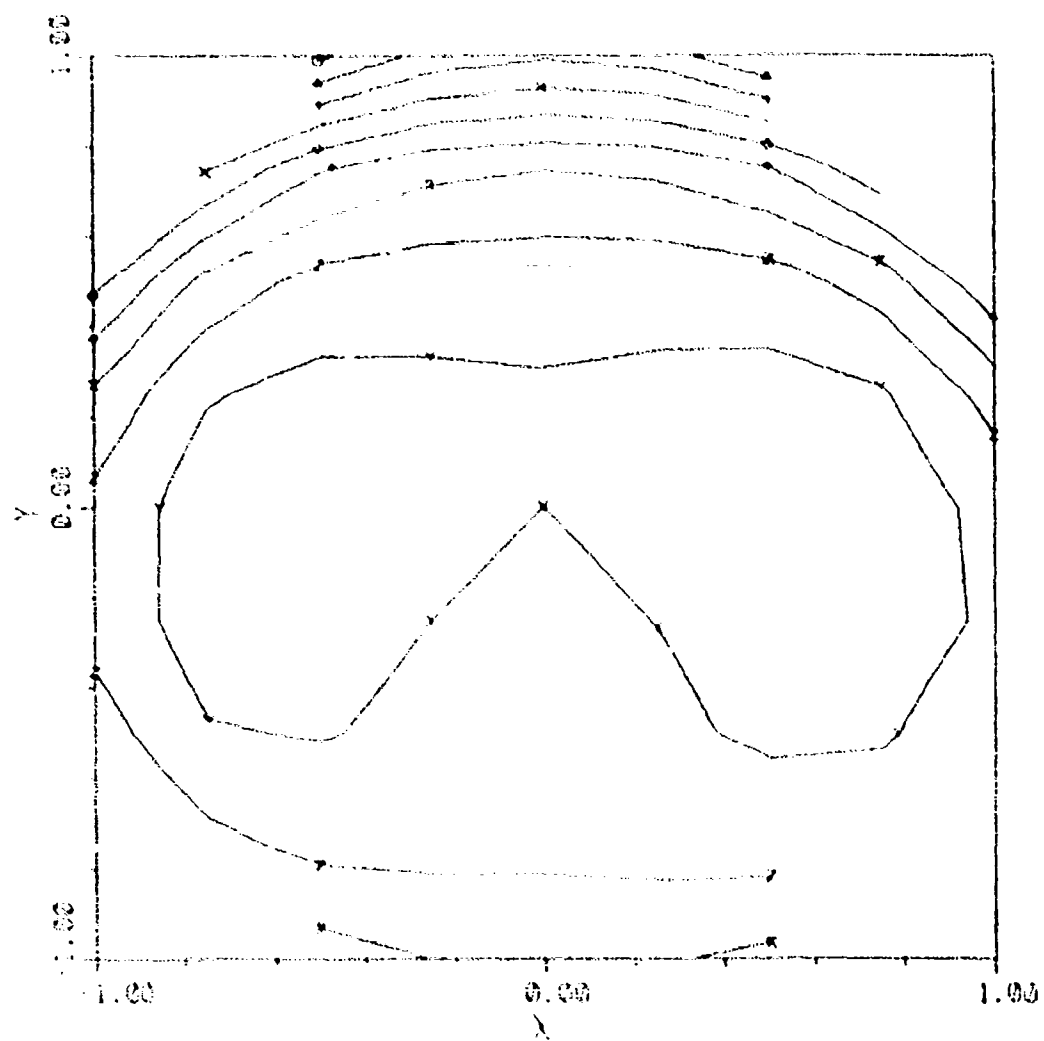


Figure 4.4 Contour Plot of the Residual Phase Aberration - Test 5



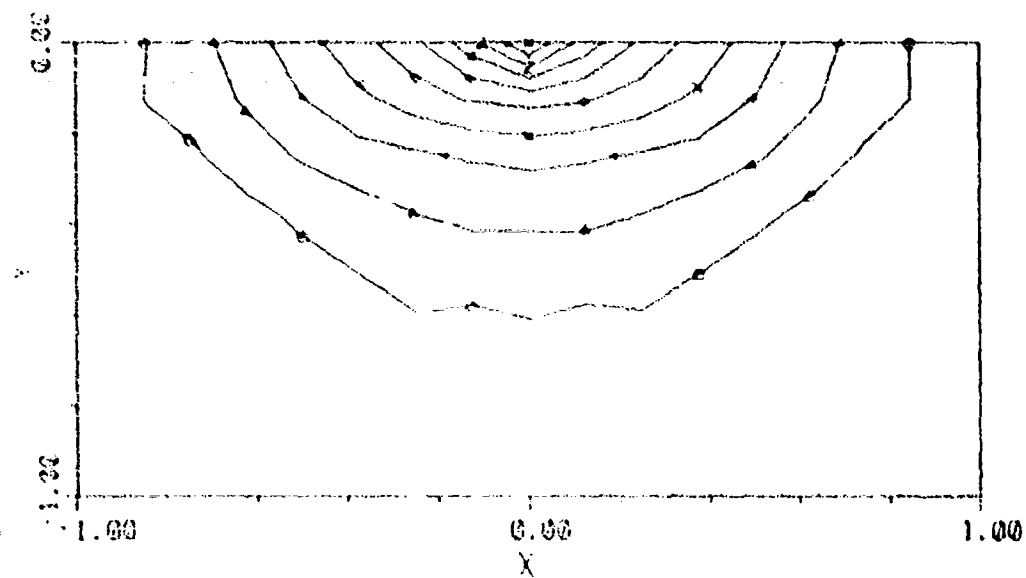
o .100
 ▲ .200
 + .300
 x .400
 ◇ .500
 ▲ .600
 * .700
 x .800
 y .900

Figure 4.5 Contour Plot of MTF from the Residual Phase Aberration



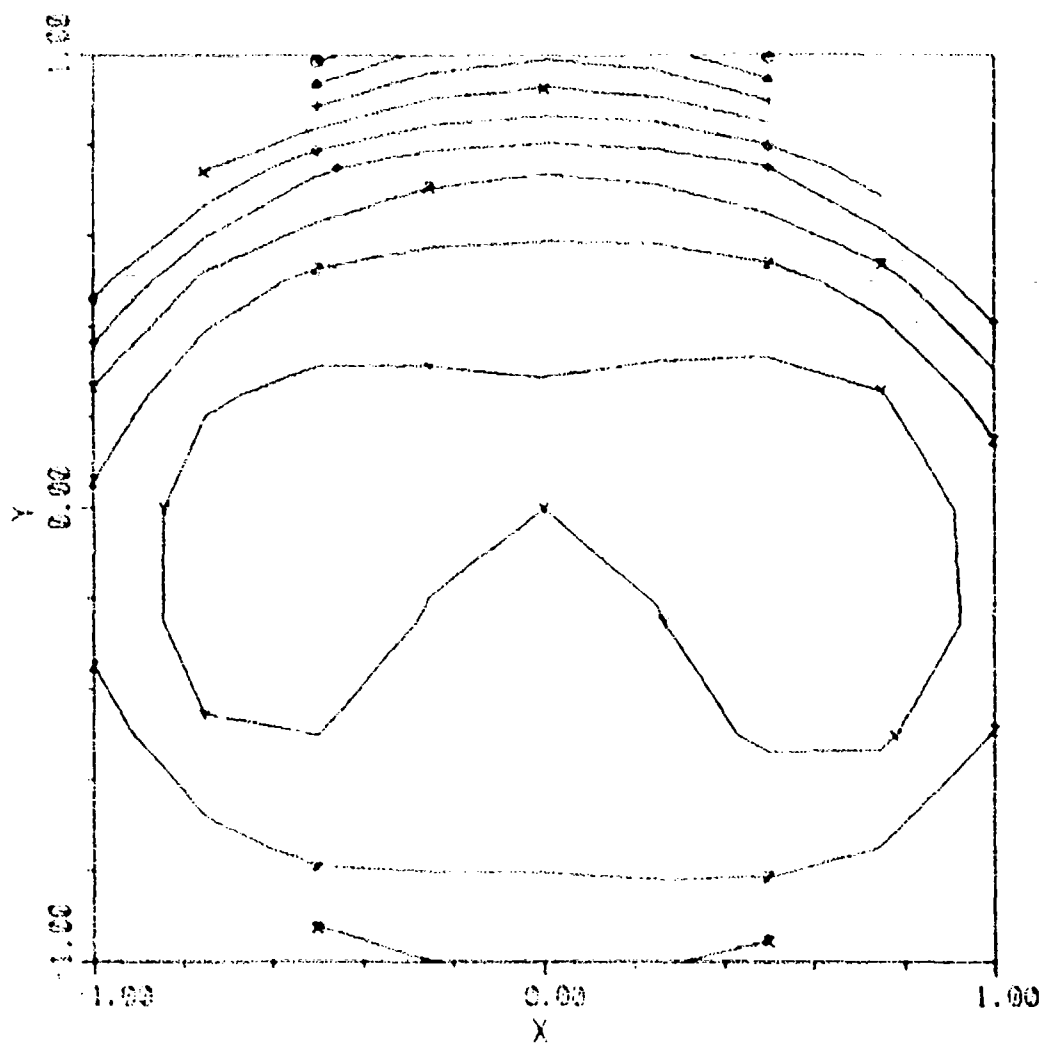
○	.800
▲	.700
+	.600
×	.500
◇	.400
◆	.300
*	.200
z	.100

Figure 4.6 Contour Plot of Initial Phase Aberration Function



c .100
 . .200
 . .300
 x .400
 o .500
 . .600
 x .700
 z .800
 v .900

Figure 4.7 Contour Plot of Initial MTF



o - .800
 ▲ - .700
 • - .600
 x - .500
 ◊ - .400
 ◆ - .300
 x - .200
 z - .100

Figure 4.8 Contour Plot of Estimated Phase Aberration Function

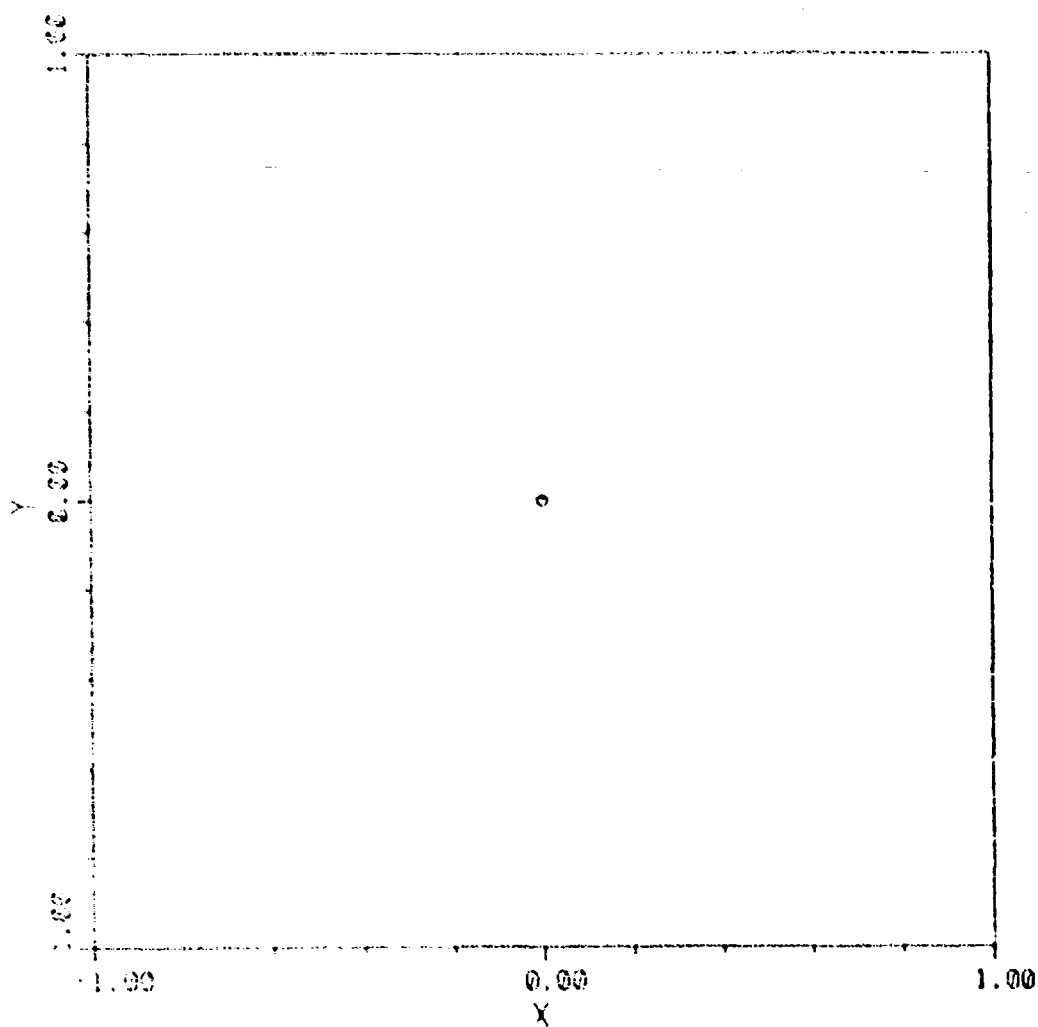
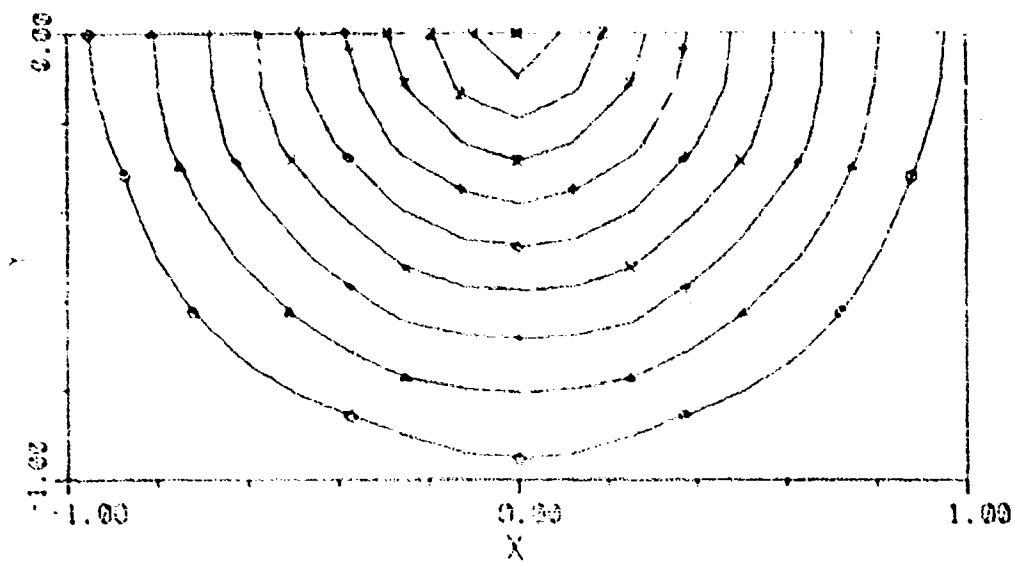
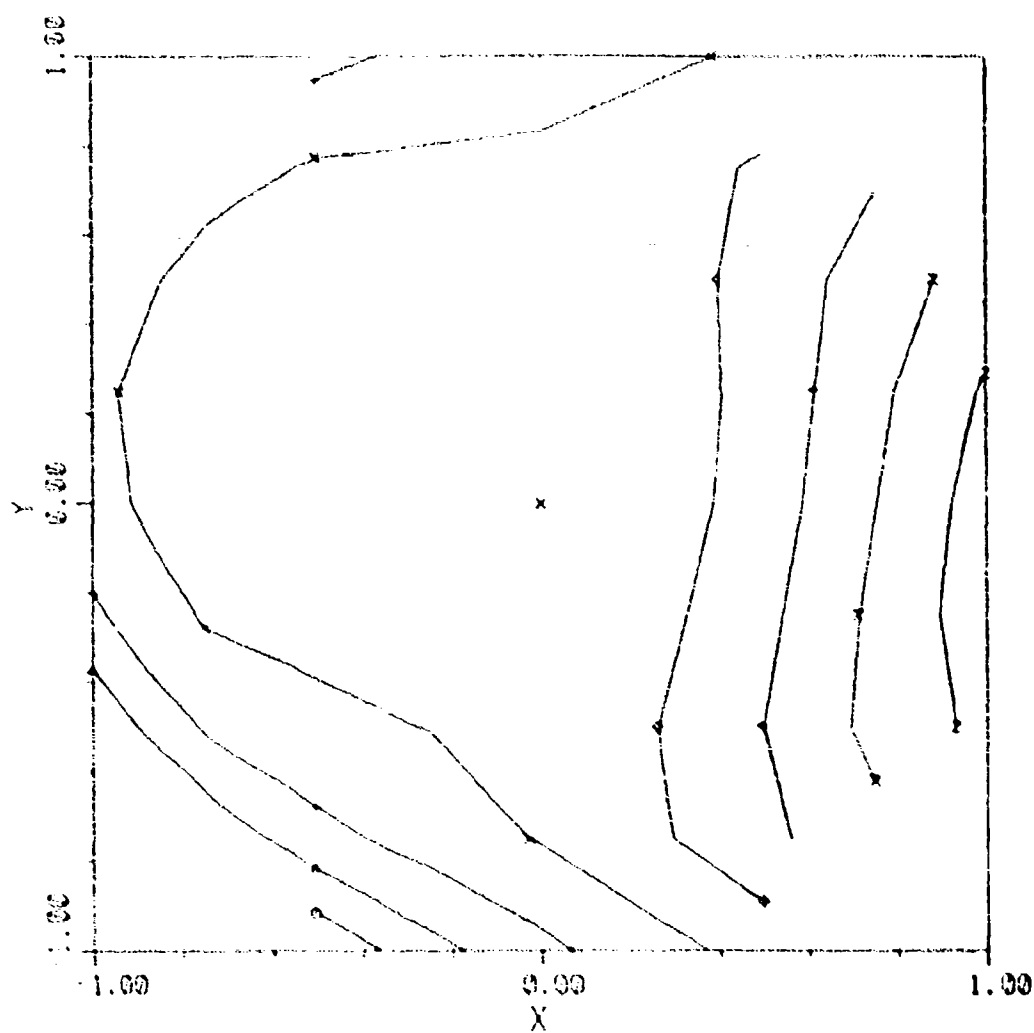


Figure 4.9 Contour Plot of the Residual Phase Aberration
(initial phase aberration less the estimated phase aberration)



- .100
- △ .200
- + .300
- × .400
- ◊ .500
- ◆ .600
- × .700
- z .800
- √ .900

Figure 4.10 Contour Plot of MTF
from Residual Phase Aberration



o - .600
 ▲ - .400
 + - .200
 x - .000
 ◇ .200
 ♦ .400
 x .600
 z .800

Figure 4.11 Contour Plot of Initial Phase Aberration Function

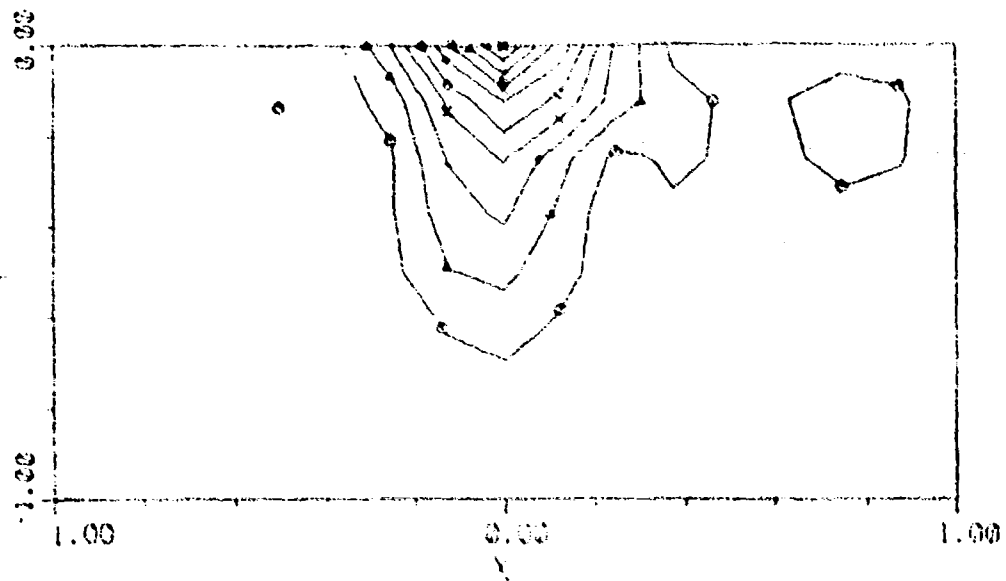
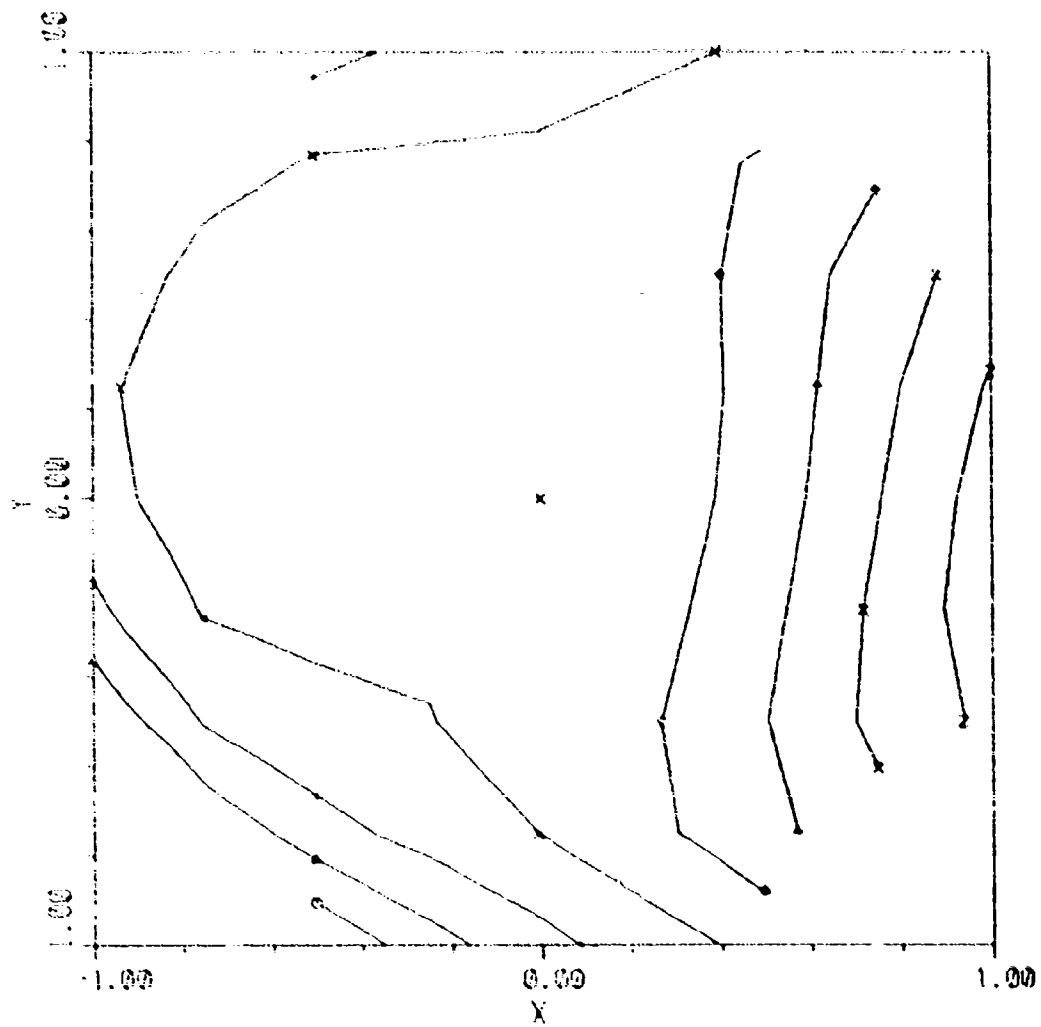
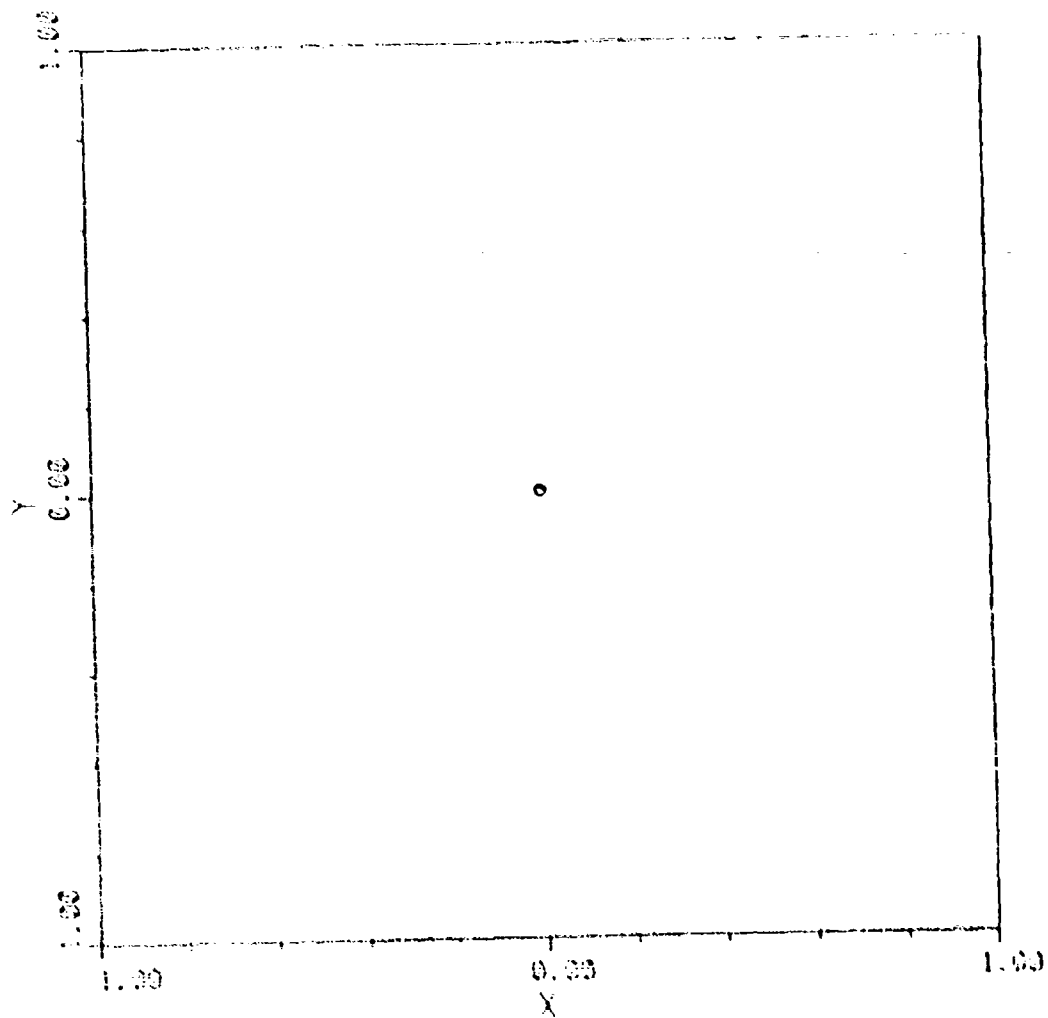


Figure 4.12 Contour Plot of Initial MTF



0 .600
 A .400
 . .200
 x .000
 . 200
 + .400
 x .600
 z .800

Figure 4.13 Contour Plot of Estimated Phase Aberration Function



o 0.000

Figure 4.14 Contour Plot of the Residual Phase Aberration

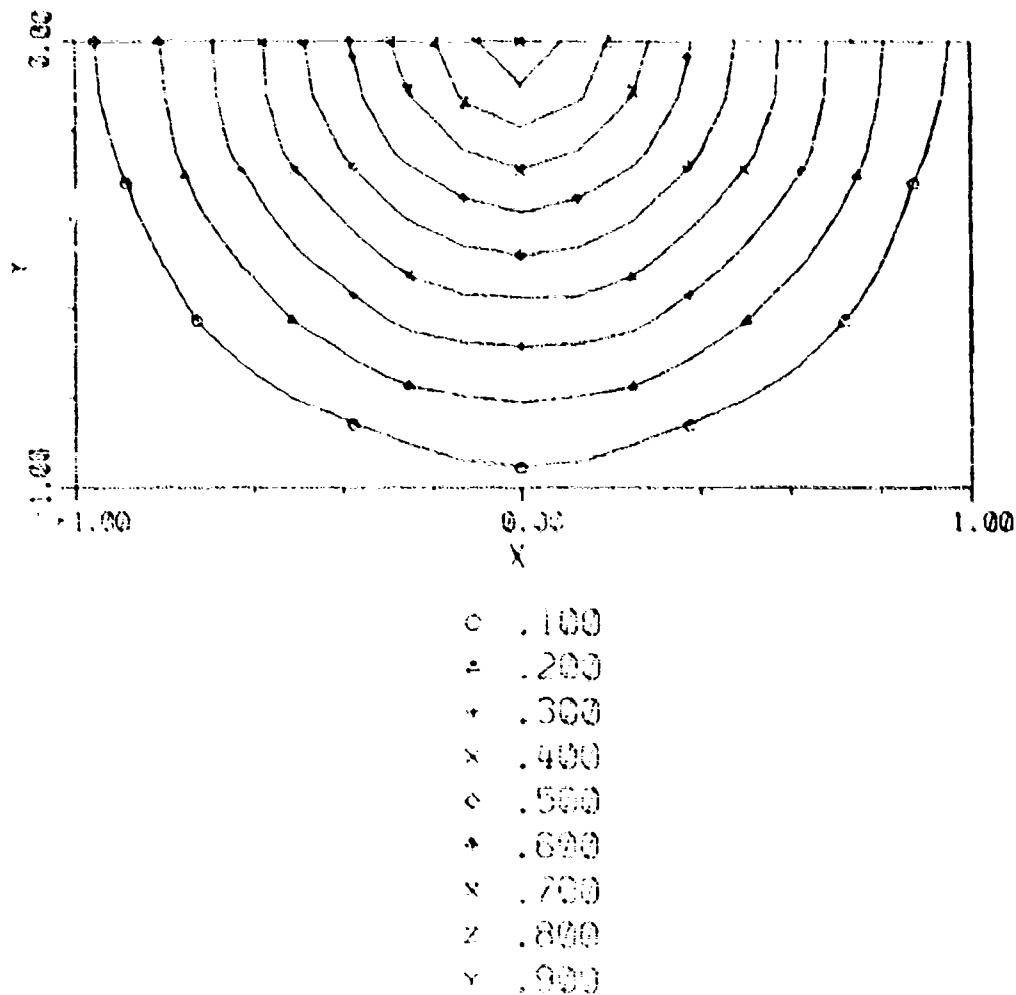


Figure 4.15 Contour Plot of MTF
from the Residual Phase Aberration

The next case used a larger and more complex aberration and required still more computer time for proper performance. Figure 4.16 numerically displays the phase aberrations over the aperture in units of radians. As can be seen, the maximum residual aberration at any point is less than 0.03 waves. Figures 4.17 through 4.19 show contour plots for this case; the residual phase aberration and MTF are not displayed since they are effectively diffraction limited.

Phase Aberration

	P H A S E A B E R R A T I O N (RADIANS)								
	1	2	3	4	5	6	7	8	9
1	0.00	0.00	-5.11	-2.41	-0.95	-0.09	0.23	0.00	0.00
2	0.00	-4.73	-1.78	-0.41	0.41	1.20	2.09	2.69	0.00
3	-6.02	-1.95	-0.43	0.10	0.48	1.19	2.35	3.72	4.36
4	-3.10	-0.47	0.15	0.12	0.20	0.83	2.14	3.91	5.34
5	-1.39	0.42	0.49	0.11	0.00	0.56	1.91	3.82	5.54
6	-0.51	1.01	0.82	0.25	0.02	0.50	1.78	3.61	5.15
7	-0.60	1.20	1.07	0.47	0.16	0.52	1.60	3.05	3.84
8	0.00	0.46	0.81	0.39	0.06	0.22	0.86	1.48	0.00
9	0.00	0.00	-1.00	-0.91	-1.18	-1.37	-1.58	0.00	0.00

Estimated Phase Aberration

	P H A S E A B E R R A T I O N (RADIANS)								
	1	2	3	4	5	6	7	8	9
1	0.00	0.00	-5.24	-2.47	-0.99	-0.12	0.14	0.00	0.00
2	0.00	-4.80	-1.86	-0.52	0.29	1.11	2.04	2.66	0.00
3	-6.15	-2.02	-0.55	-0.02	0.37	1.08	2.25	3.69	4.26
4	-3.15	-0.56	0.04	0.05	0.17	0.77	2.04	3.84	5.32
5	-1.42	0.34	0.41	0.08	0.00	0.53	1.82	3.74	5.52
6	-0.55	0.93	0.73	0.19	-0.02	0.43	1.68	3.53	5.11
7	-0.73	1.14	0.96	0.35	0.05	0.40	1.48	3.00	3.73
8	0.00	0.39	0.74	0.27	-0.07	0.10	0.79	1.41	0.00
9	0.00	0.00	-1.14	-0.98	-1.25	-1.44	-1.71	0.00	0.00

Residual Phase Aberration

	P H A S E A B E R R A T I O N (RADIANS)								
	1	2	3	4	5	6	7	8	9
1	0.00	0.00	0.13	0.06	0.04	0.04	0.09	0.00	0.00
2	0.00	0.08	0.08	0.11	0.12	0.10	0.05	0.03	0.00
3	0.13	0.07	0.12	0.12	0.11	0.11	0.10	0.03	0.09
4	0.05	0.09	0.11	0.06	0.04	0.06	0.09	0.07	0.02
5	0.04	0.09	0.09	0.03	0.00	0.03	0.09	0.08	0.02
6	0.04	0.08	0.10	0.06	0.04	0.06	0.10	0.08	0.03
7	0.13	0.05	0.11	0.12	0.11	0.12	0.12	0.06	0.11
8	0.00	0.07	0.07	0.11	0.13	0.12	0.08	0.06	0.00
9	0.00	0.00	0.14	0.07	0.07	0.07	0.13	0.00	0.00

Figure 4.16 Test 14 Phase Aberration

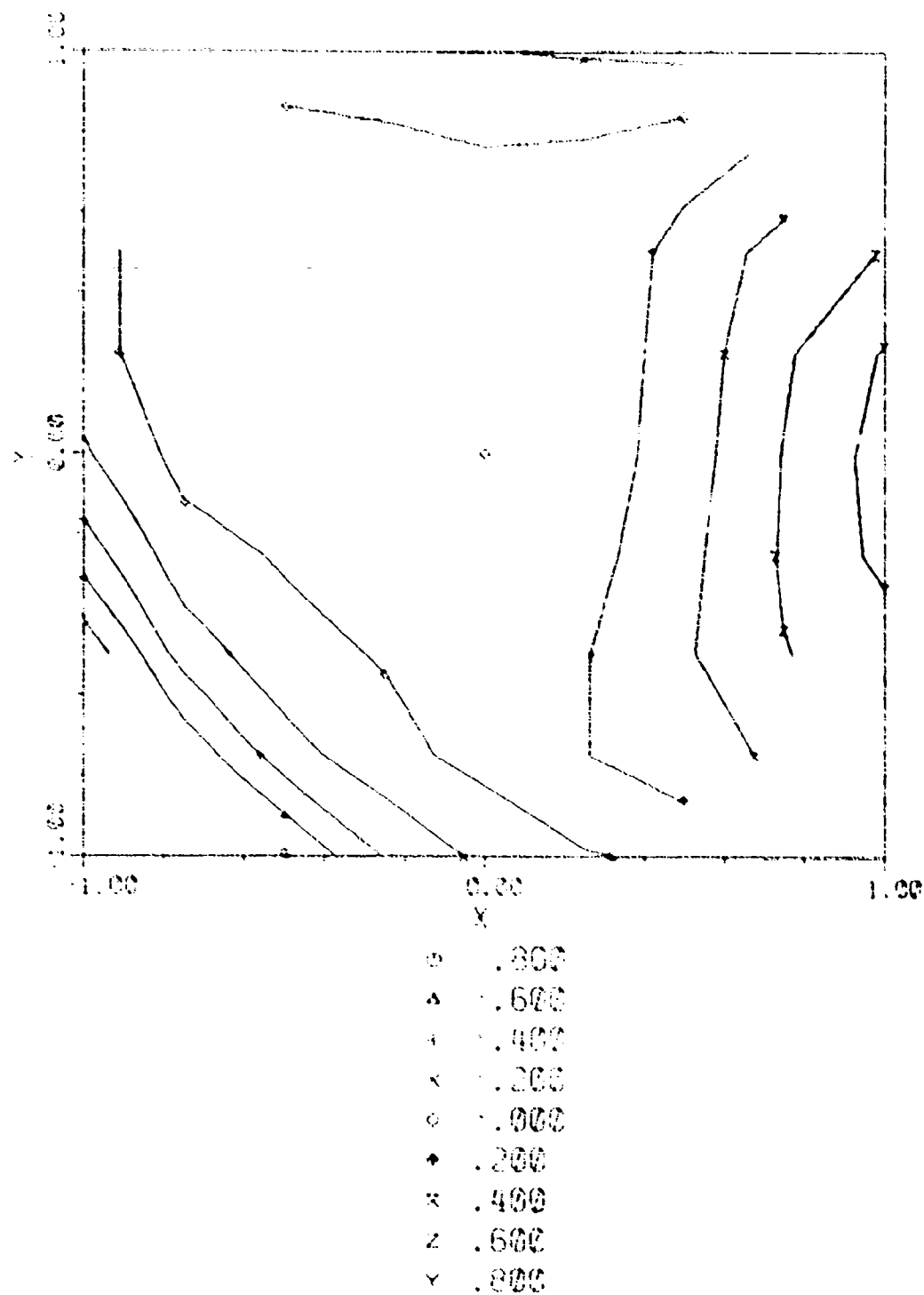
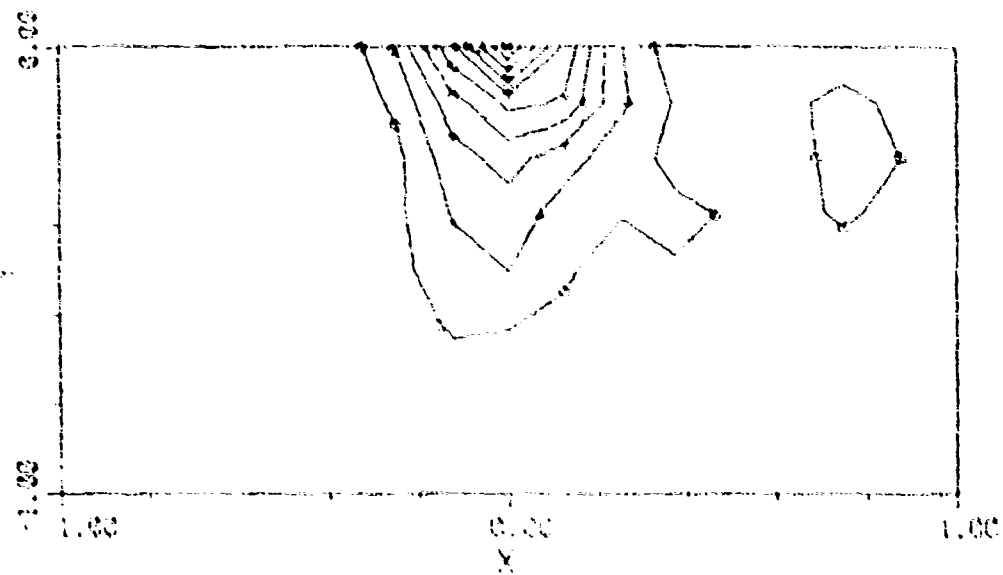


Figure 4.17 Contour Plot of Initial Phase Aberration Function



. .100
 . .200
 . .300
 x .400
 o .500
 + .600
 v .700
 z .800
 y .900

Figure 4.18 Contour Plot of Initial MTF

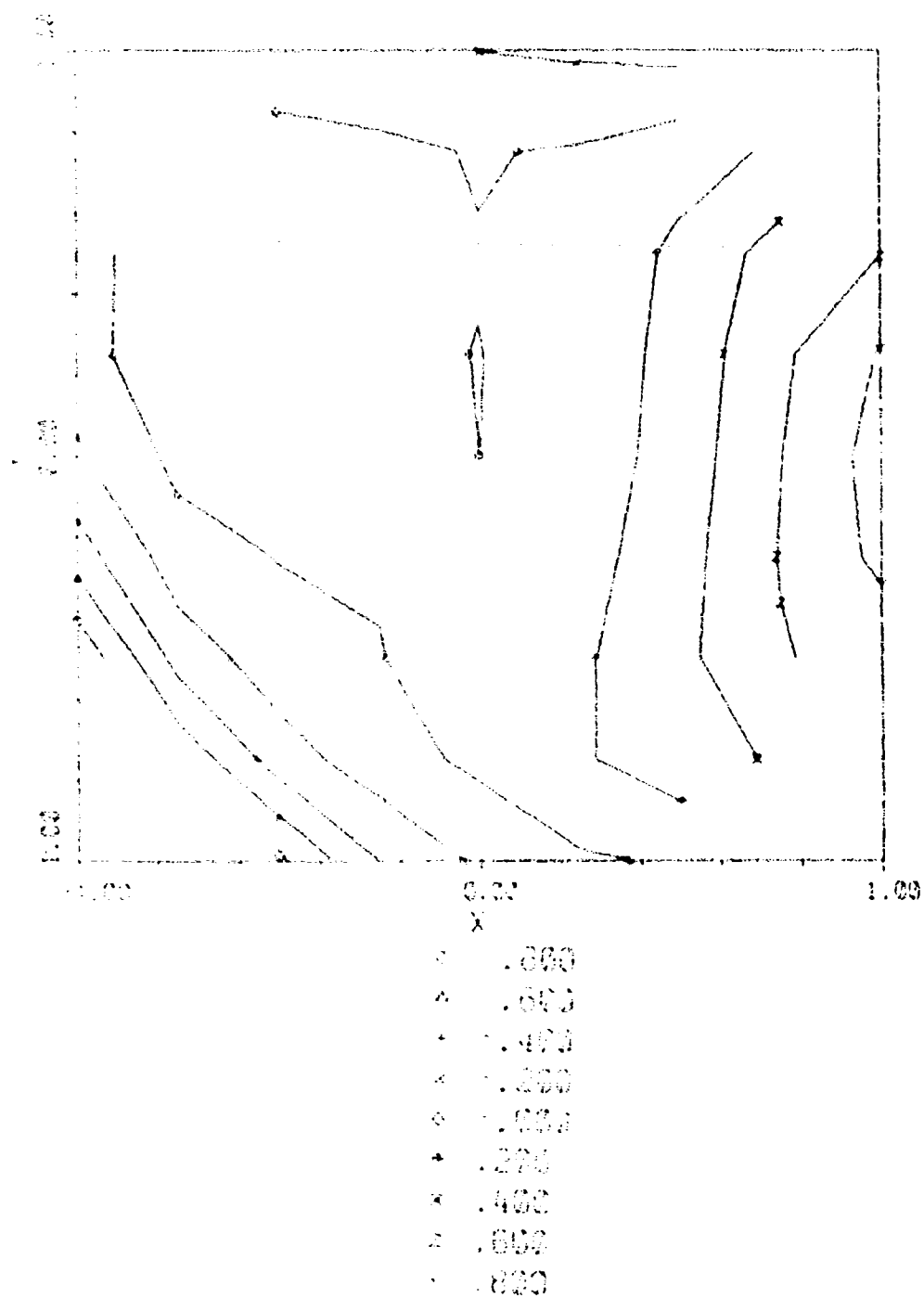


Figure 4.19 Contour Plot of Estimated Phase Aberration Function

Another case is shown in Figures 4.20 through 4.22. Figure 4.20 is the initial point spread function. The results of applying the wavefront correction as estimated by the phase retrieval program is shown in Figure 4.21. This estimate was clearly not an optimum estimate. Nevertheless, it is close enough to the actual aberration that the corrected point spread function is considerably improved. The phase retrieval program was then run again, with this improved point spread function as input. Correcting the system this time yields diffraction limited performance. This is an illustration of an "iterative" correction scheme, where each correction results in an improvement over the previous state of the optics. If the aberrations are severe enough, it may well not be feasible to do all the correction at once, but rather to employ a series of correction steps.

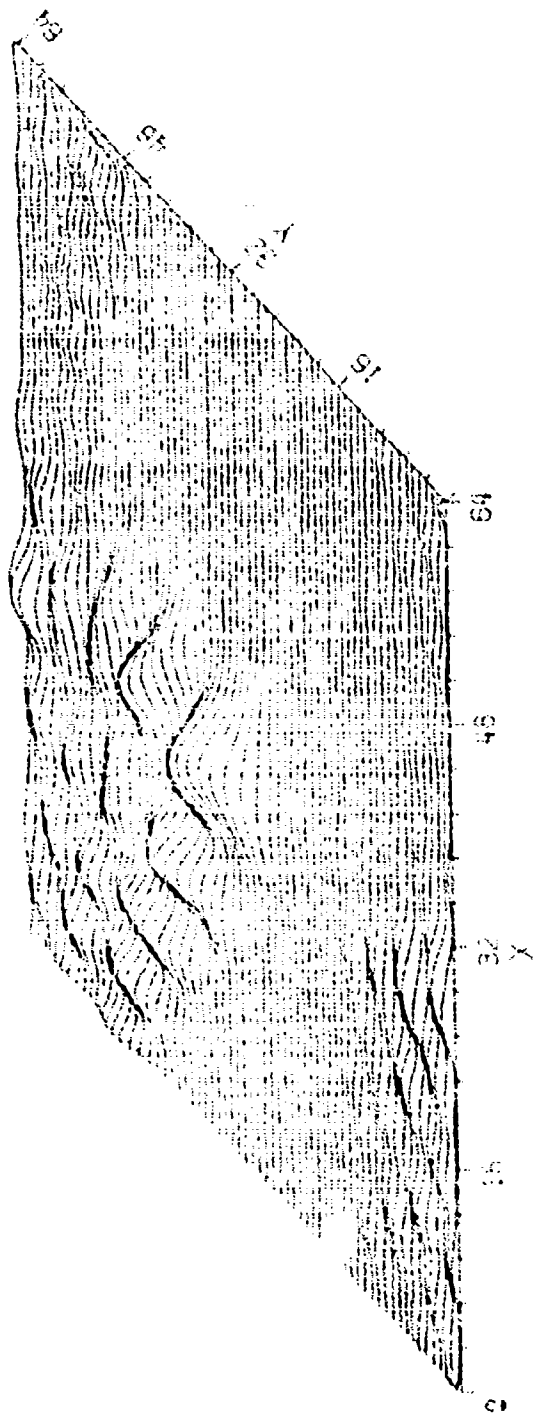


Figure 4.20 PSF Input to First Iteration

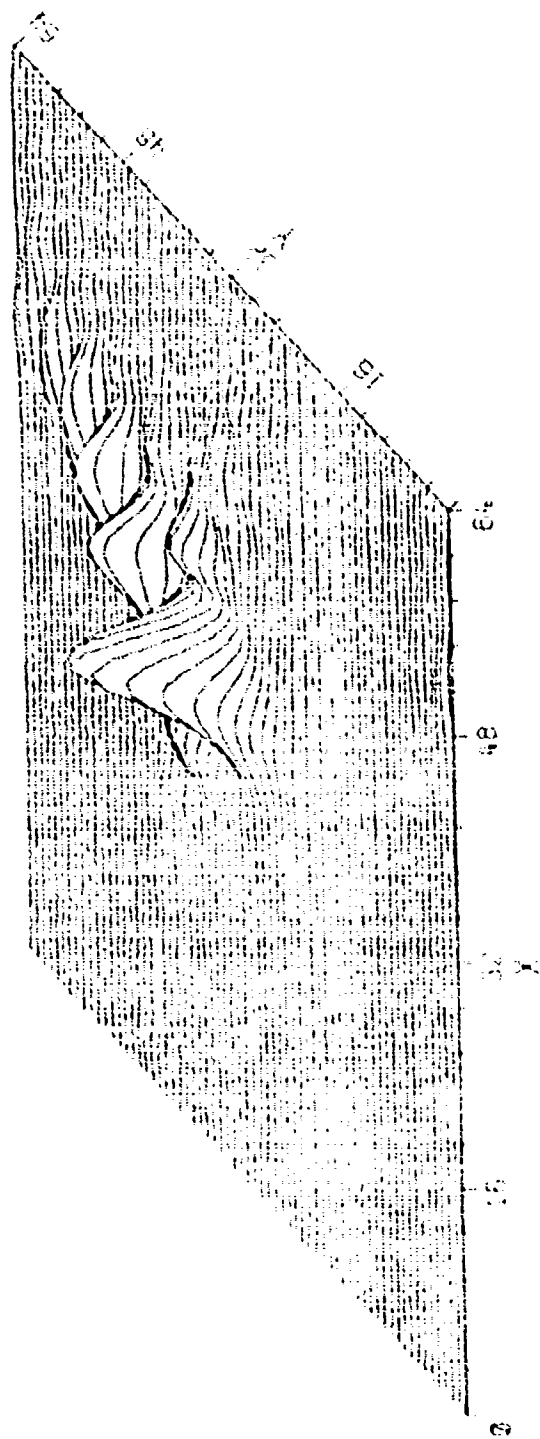


Figure 4.21 PSF After First Correction

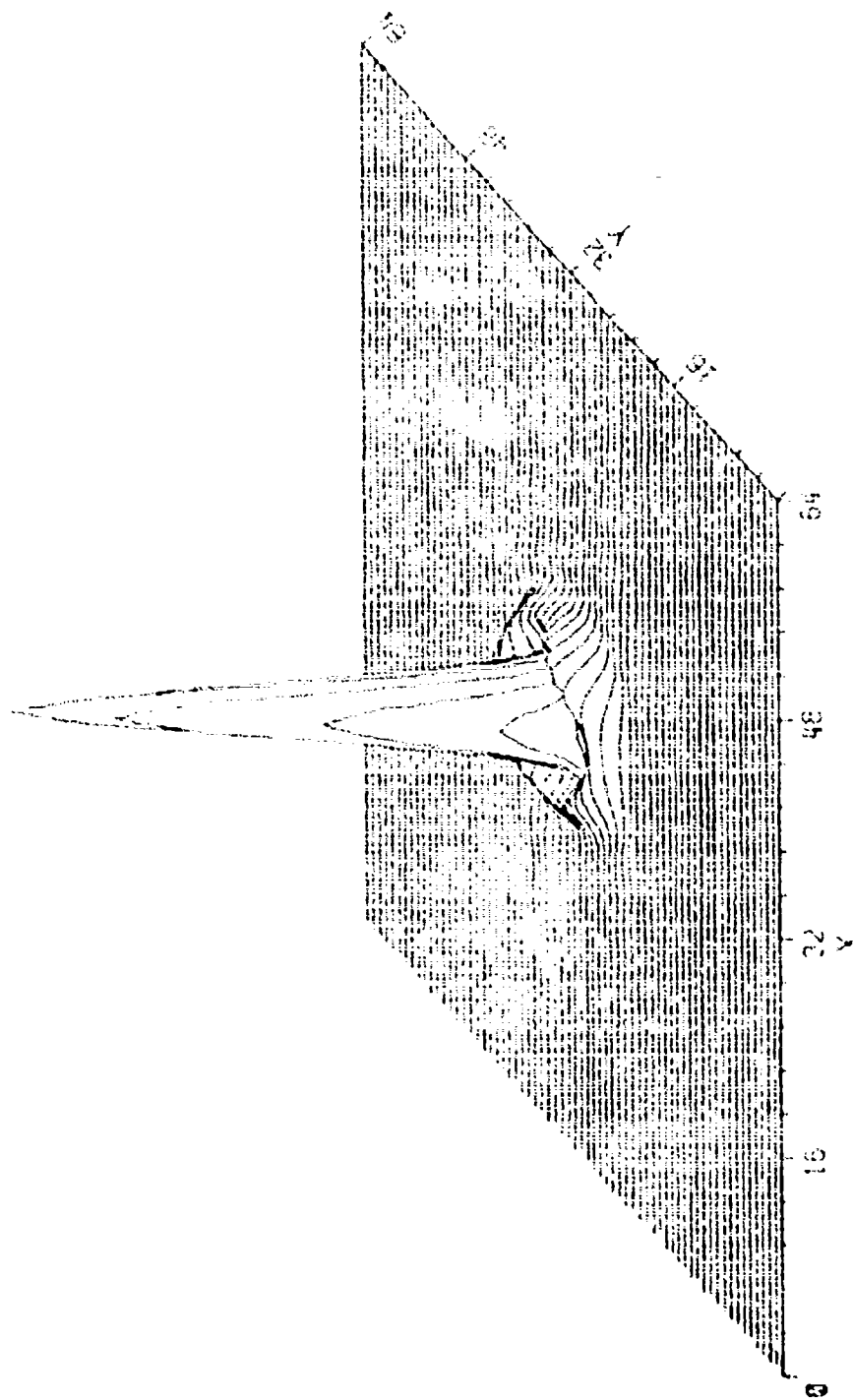


Figure 4.22 PSF After Second Correction

4.2 EFFECTS OF NOISE

We now present results showing the effects of detector noise. This noise is white, Gaussian, signal-independent noise characterized by a Noise Equivalent Flux Density (NEFD). This is the power from a point source falling on the entrance pupil which gives a signal to noise ratio of unity in the detector which receives the maximum amount of power from the diffraction limited point spread function. As such defined, the NEFD is dependent on the area of the entrance pupil. Assume we are sampling at the Nyquist rate with square detectors of area a , and s_j is the star image at the j^{th} sample position. The RMS noise power is

$$\sigma_N = A \cdot \text{NEFD}$$

where A is the aperture size. The total power from one detector is

$$s'_j = a s_j + \sigma_N n$$

where n is a unit variance white Gaussian noise signal. The sum of the power in the noise signal must equal the incident power:

$$a \sum_j s_j = I_0 A$$

where I_0 is the power per unit area over the entrance pupil. If a normalized signal is defined

$$\frac{A}{S_j} = \frac{s_j}{\frac{I_0 A}{a}}$$

then

$$\sum_j \hat{S}_j = 1$$

and

$$S_j = \hat{S}_j \cdot I_0 A + A \cdot \text{NEFD}_n$$

The signal to noise ratio at the diffraction limited PSF peak, \hat{S}_p , is

$$S/N = \frac{I_0}{\text{NEFD}} \hat{S}_p$$

In our simulation, \hat{S}_p was equal to 69./289., so for a S/N ratio of W, we have

$$\frac{I_0}{\text{NEFD}} = W \cdot 4.2$$

A zero magnitude star has a power of 3.6×10^{-15} watts/cm²_μ. Assuming a narrow band filter transmitting 0.1_μ wavelength to get nearly monochromatic radiation, the total power is 3.6×10^{-16} watts/cm². The star magnitude simulated is thus, from the definition of magnitude,

$$2.4 \log_{10} \frac{W \cdot 4.2 \cdot \text{NEFD}}{3.6 \times 10^{-16}}$$

Figures 4.23 through 4.31 present the results of a simulation with noise. Figure 4.23 shows contours of the initial phase aberration across the exit pupil. The key to the right shows the contour values in terms of waves. Figures 4.24 shows contours of the MTF corresponding to this phase aberration. Figure 4.25 is the MTF after noise has been added. The phase

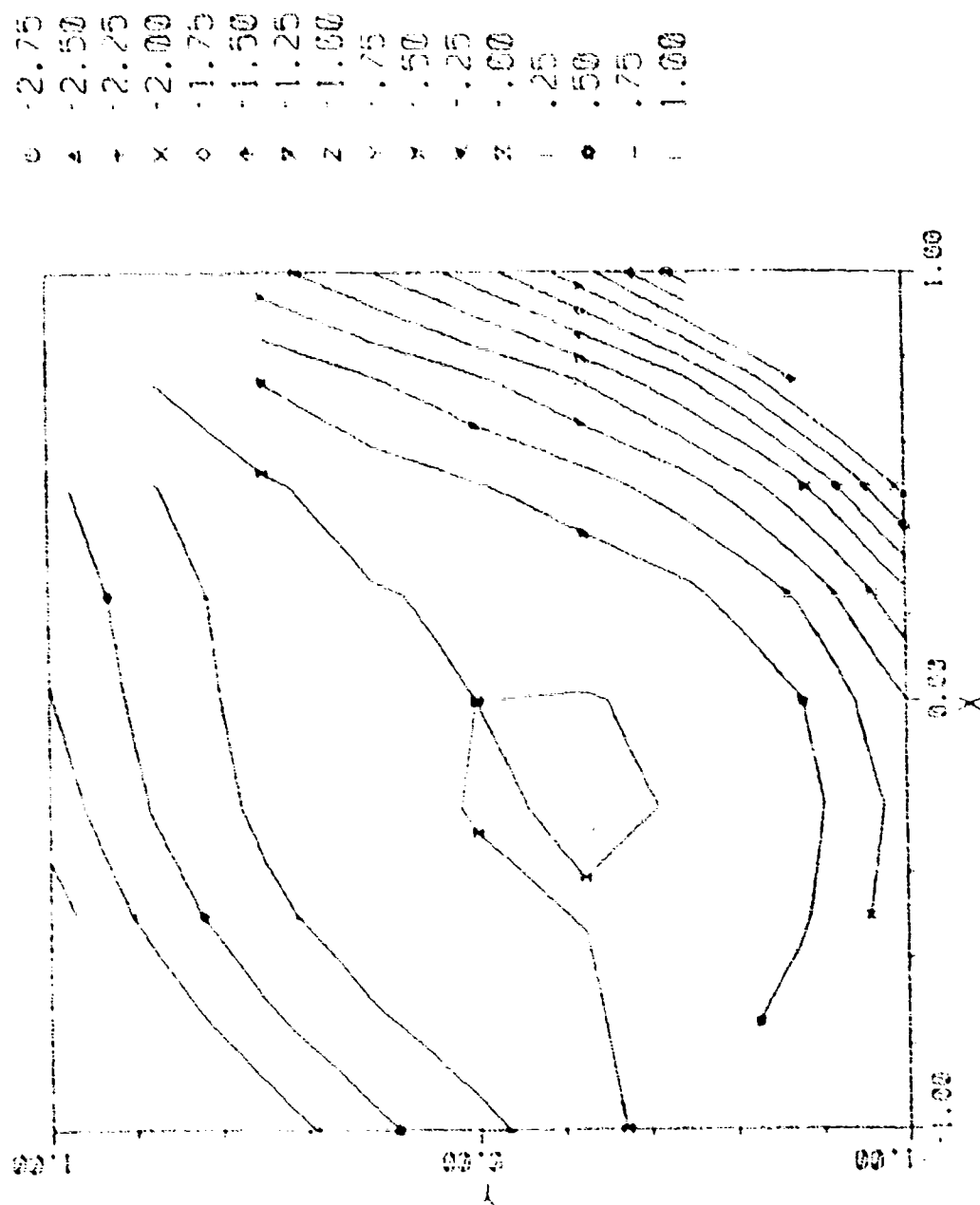


Figure 4.23 Initial Phase Aberration

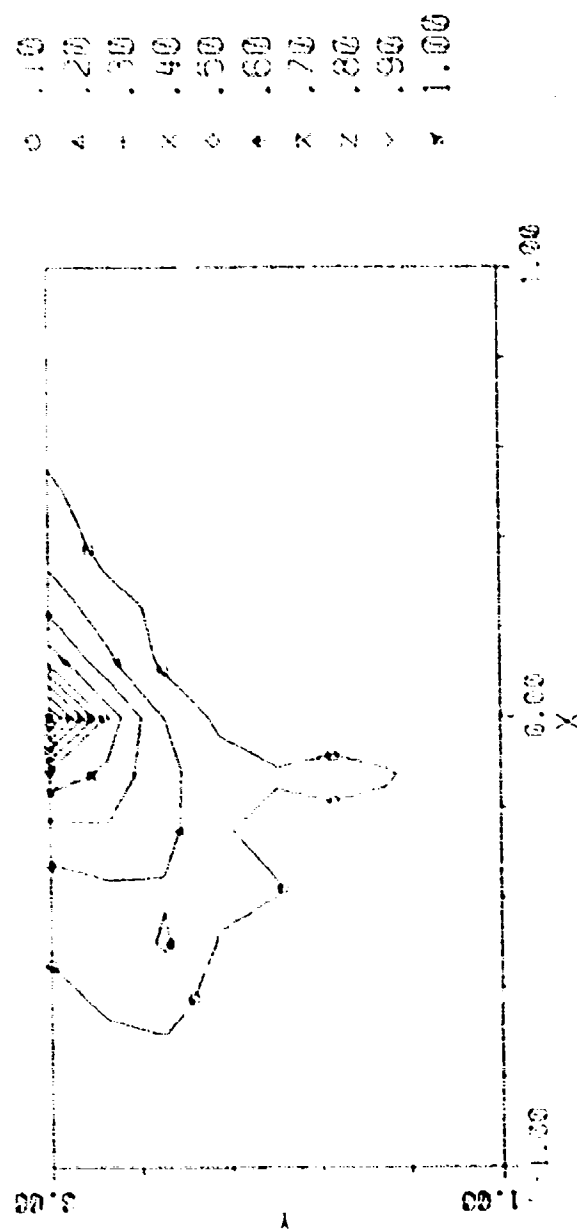
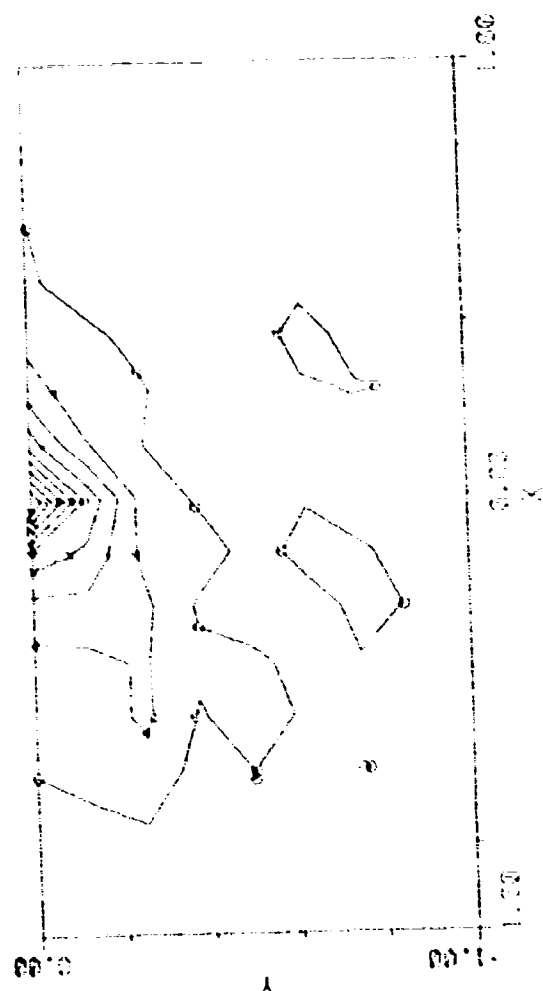


Figure 4.24 Initial MTF

0.10
 0.20
 0.30
 0.40
 0.50
 0.60
 0.70
 0.80
 0.90
 1.00



INIT MTF W/N

Figure 4.25 Initial MTF with Added Noise

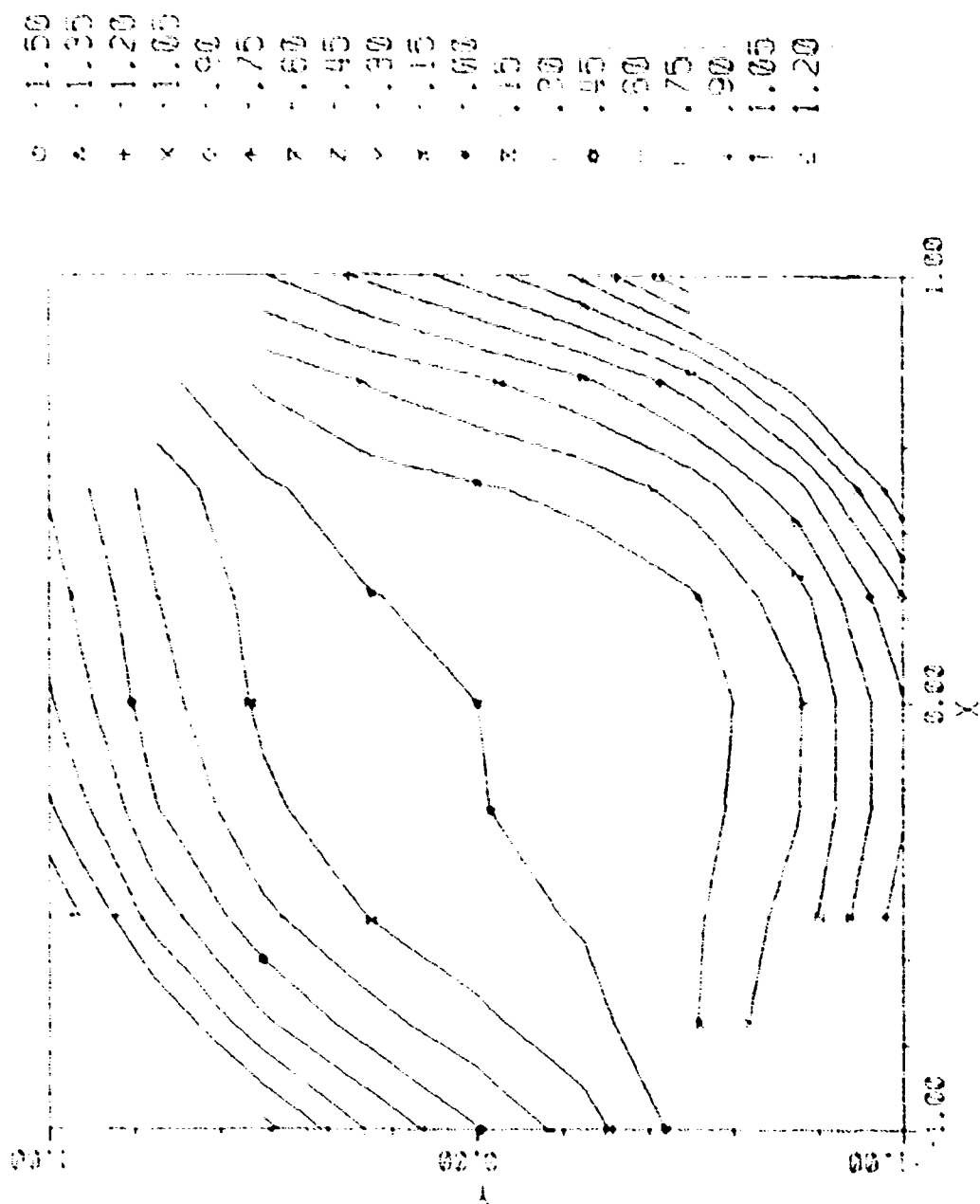


Figure 4.26 Estimated Phase in Noisy Case

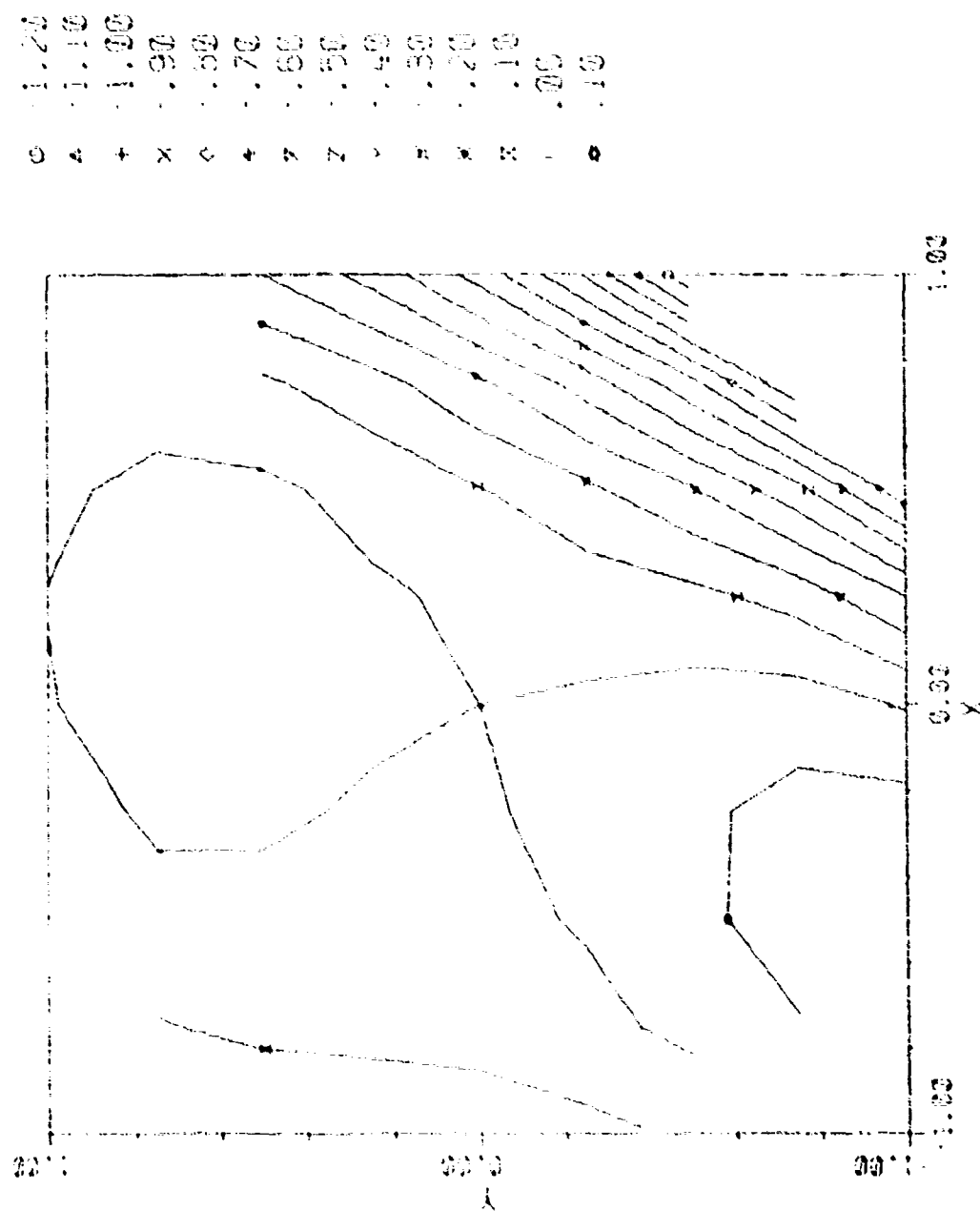


Figure 4.27 Residual Phase Aberration After Correction in Noisy Case

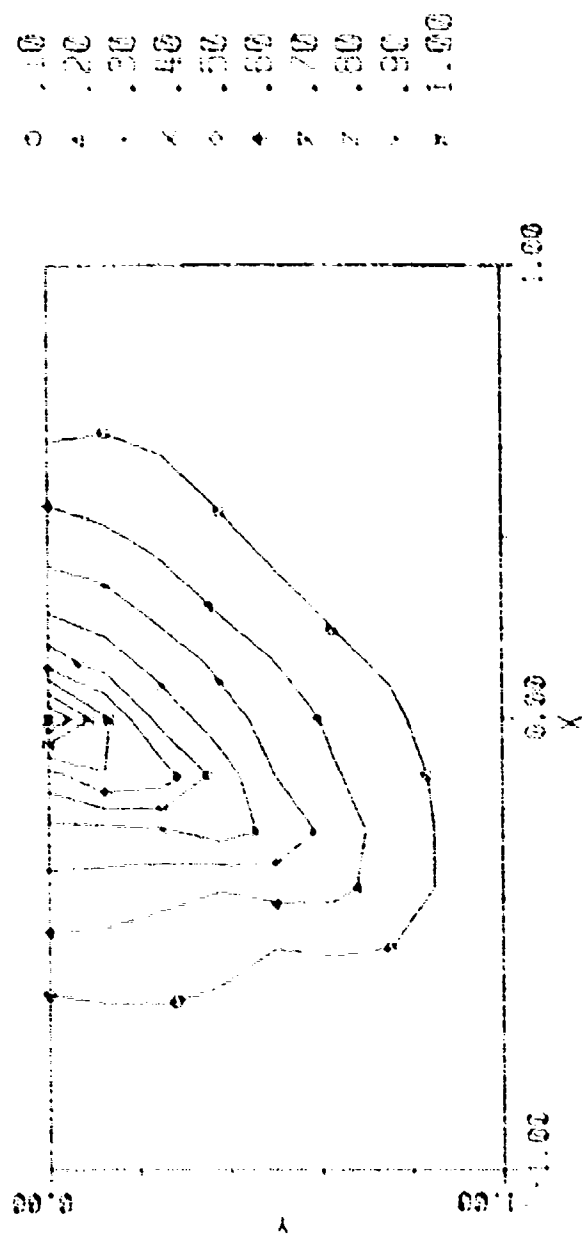


Figure 4.28 MTF After Correction in Noisy Case

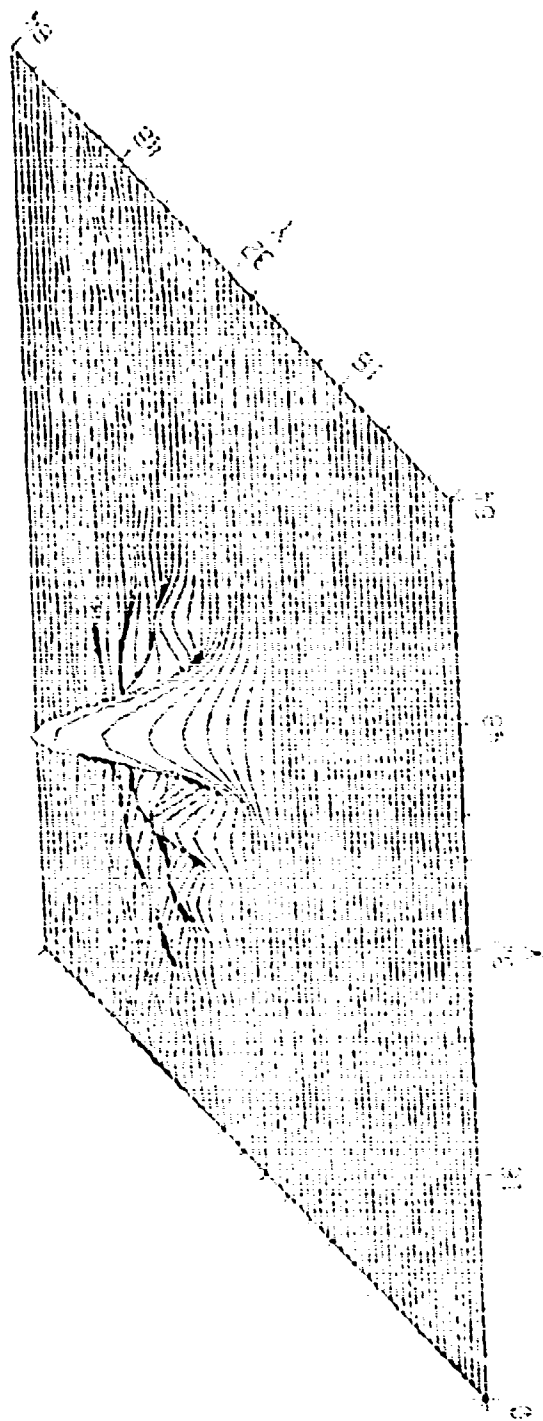


Figure 4.29 Original PSF

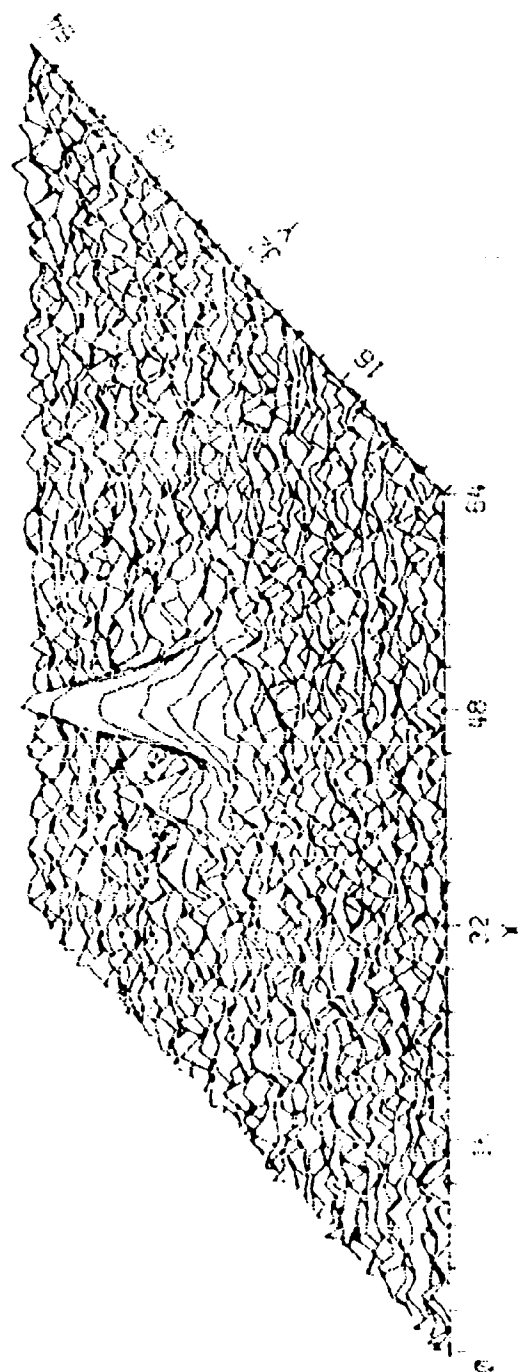


Figure 4.30 Original PSF with Noise

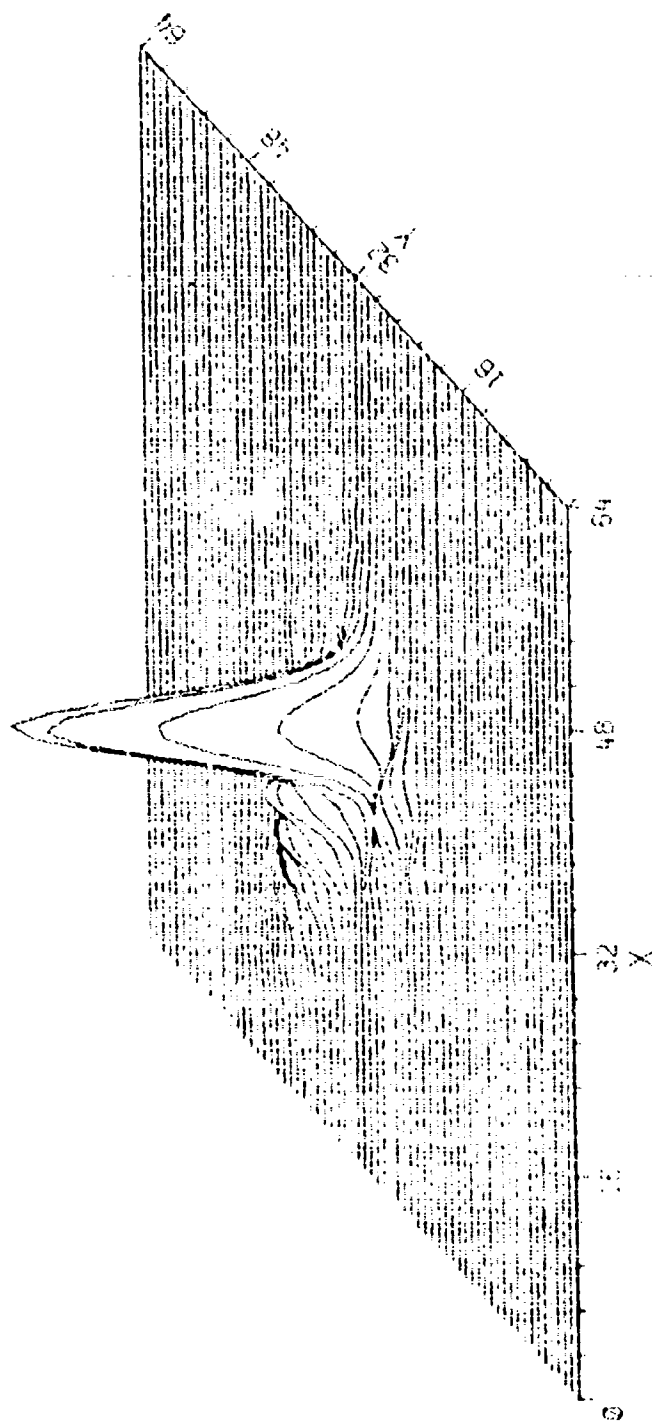


Figure 4.31 Corrected PSF from First Run of Algorithm in Noisy Case

aberration as estimated by the program is displayed in Figure 4.26. The residual phase, equal to the initial less the estimate, is shown in Figure 4.27. Note that it is significantly less aberrated than the initial phase. The MTF corresponding to the residual phase aberration is in Figure 4.28. No noise has been added to this MTF. The point spread function from the initial aberration is shown in Figure 4.29. The same PSF with added noise is shown in Figure 4.30. The PSF from the corrected system is displayed in Figure 4.31. This is definitely sharper than the first PSF. When the same case was run without noise, the corrected PSF was as shown in Figure 4.32. This is very nearly diffraction limited. However, it must not be thought that the noise was really responsible for a poorer phase estimate. When the program was rerun in such a manner as to simulate the results of a more complex version of the algorithm, a much better estimate of the phase aberration was obtained. The PSF from this correction is displayed in Figure 4.33. The version of the algorithm needed to insure good results in this case requires much more computer time to execute. For a different phase aberration or an algorithm differing in its details, it could well be that a noise-free simulation might yield a poorer estimate than a simulation with noise. The algorithm is not perfect, but the noise presents no additional difficulty. It should not be difficult to find stars which will provide at least the signal to noise ratio tested here.

4.3 EFFECTS OF NON-POINT DETECTORS

In the case of extended (non-point) detectors the measured point spread function $\hat{PSF}(x, y)$ is related to the ideal point spread function $PSF(x, y)$ by

$$\hat{PSF}(x, y) = PSF(x, y) \odot D(x, y),$$

where $D(x, y)$ is the detector response which we have taken as a square of side L :

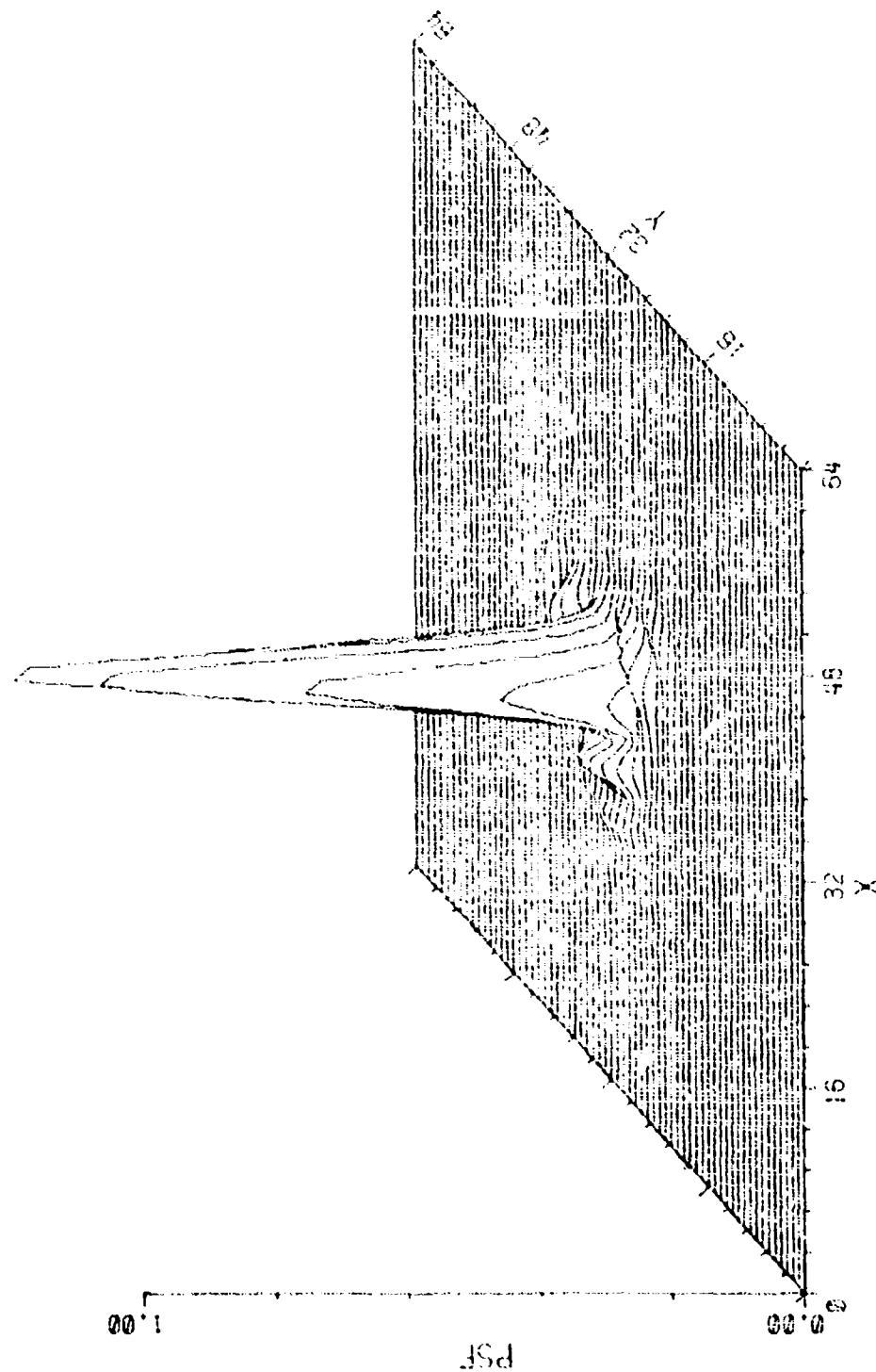


Figure 4.32 Corrected PSF from Noise-Free Case

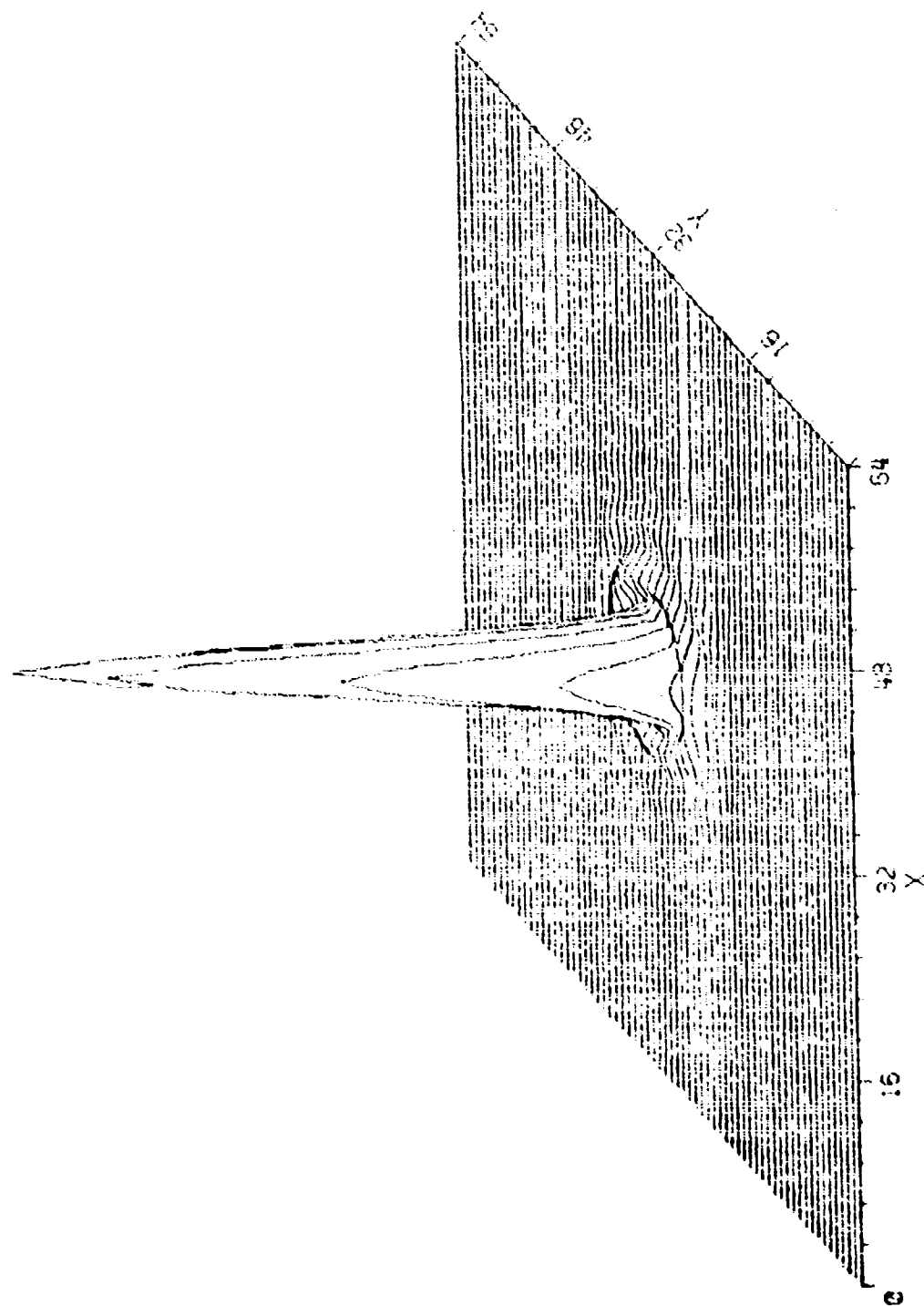


Figure 4.33 Corrected PSF from improved algorithm in noisy case

$$D(x, y) = 1 \quad 0 \leq x < L, \quad 0 \leq y < L$$

$$= 0 \quad \text{otherwise}$$

The OTF is multiplied by the transform of D

$$\hat{OTF}(f_x, f_y) = OTF(f_x, f_y) \frac{\sin \pi L f_x \sin \pi L f_y}{L^2 f_x f_y}$$

A detector size of 100 units, as used in the simulations, has the first zero due to the sine function at a spatial frequency of 0.01 cycles/unit. The optical system with which we have simulated here has a diffraction-limited cut-off frequency as determined by the F# and the wavelength of 0.05 cycles/unit which is severely limited by the detector size.

Despite these detector size limitations on the received signal, the phase retrieval algorithm shows a remarkable ability to correctly perform estimates, even in the presence of noise.

The results obtained in one simulation are presented in Figures 4.34 through 4.38. Figure 34 shows the intensity profile of a star object of the same brightness relative to the detector noise as presented in Section 4.4 imaged by an optical system possessing a wave aberration function shown in Figure 4.35. The image of the star was assumed to move across the focal plane detector array at a sufficiently small angle to the array axis to allow the convolution of the star image with the array transfer function to be sampled at the Nyquist rate, $\lambda F\#/2$, which is 10 units in the simulation. This convolution is shown in Figure 4.36 where it is assumed that the detector array is composed of square, 100 unit x 100 unit detector elements. The signal has been multiplied by a factor of ten relative to Figure 4.38, since otherwise it would be difficult to see. Assuming the same NEFD as used in Section 4.2 the noise corrupted, detected signal which

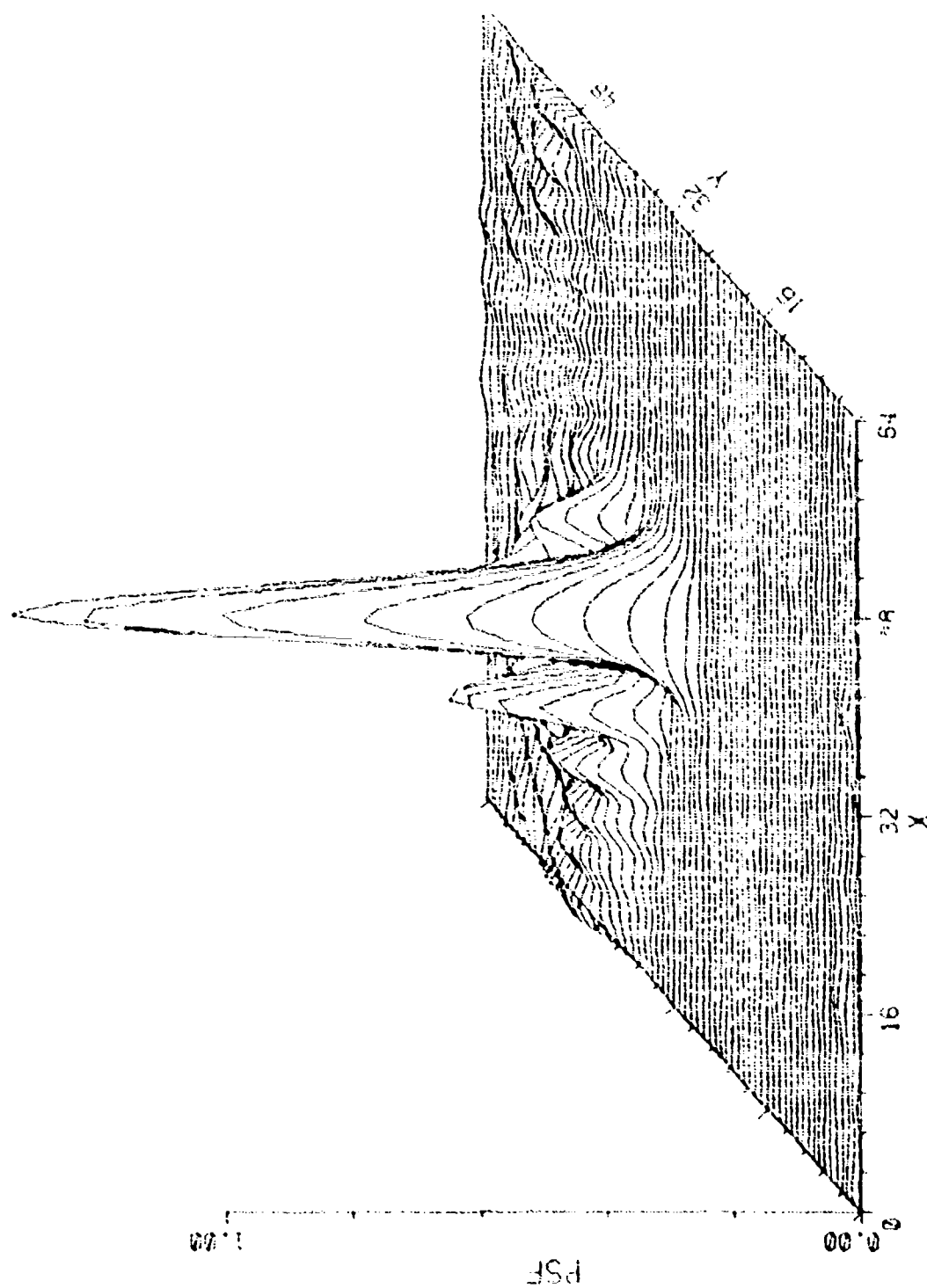


Figure 4.34 Initial System Point Spread Function

Contour values (in waves)

0
-2.750
-2.500
-2.250
-2.000
-1.750
-1.500
-1.250
-1.000
-.750
-.500
-.250
-.000
.250
.500
.750
1.000

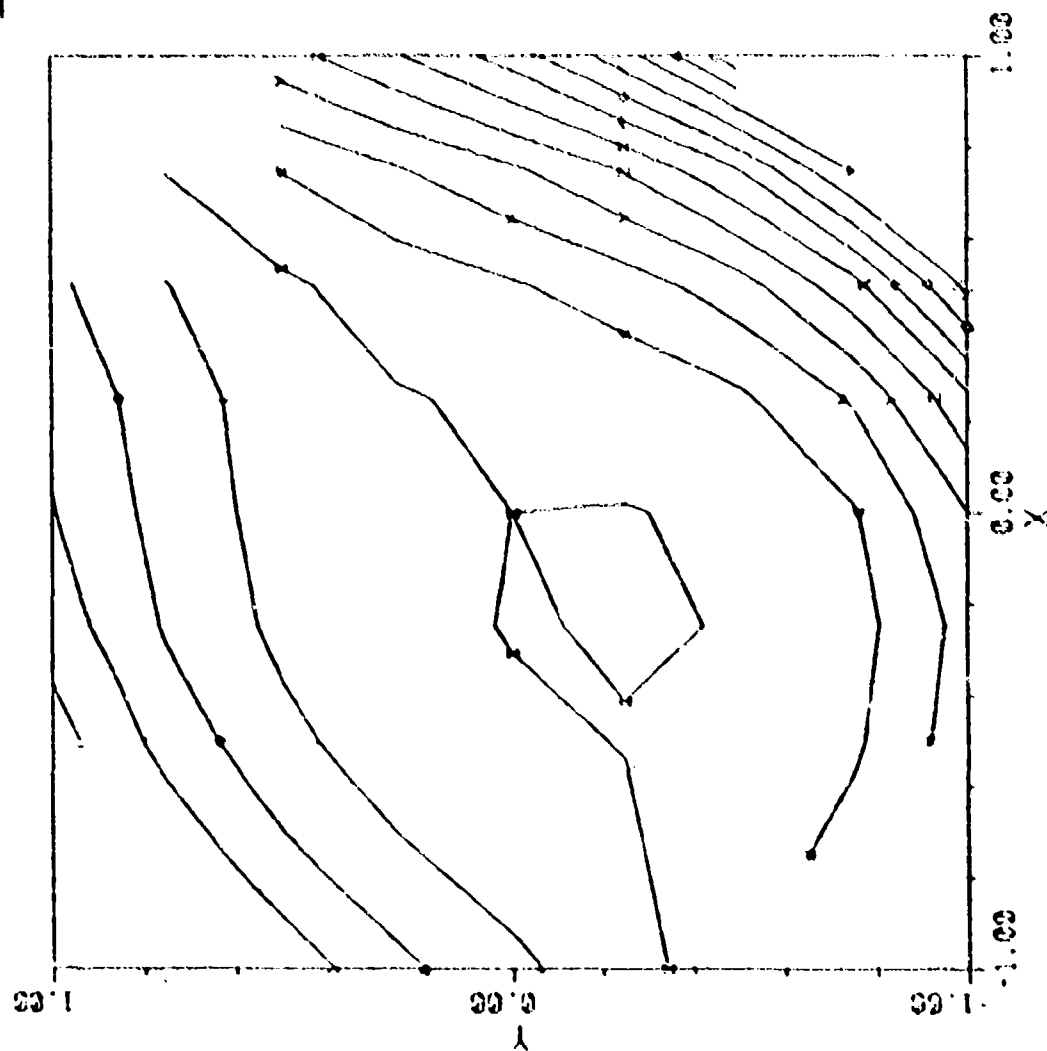


Figure 4.35 Initial Phase Aberration Across the Exit Pupil

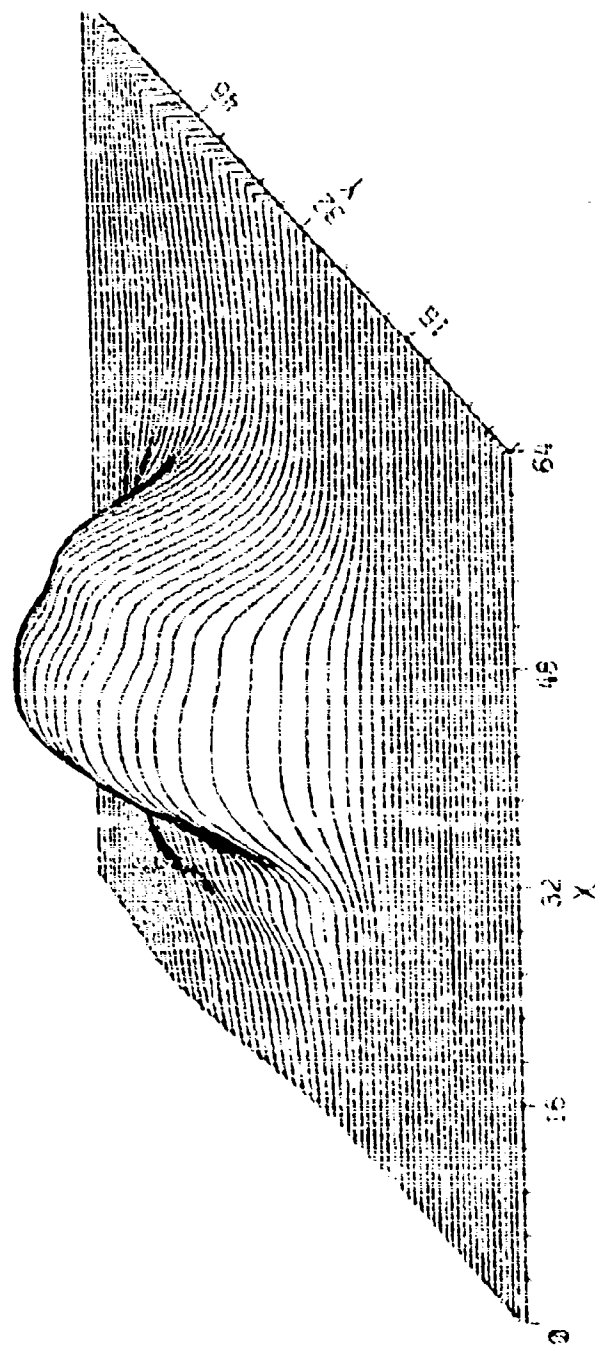


Figure 4.36 Initial Point Spread Function Convolved with Detector Size

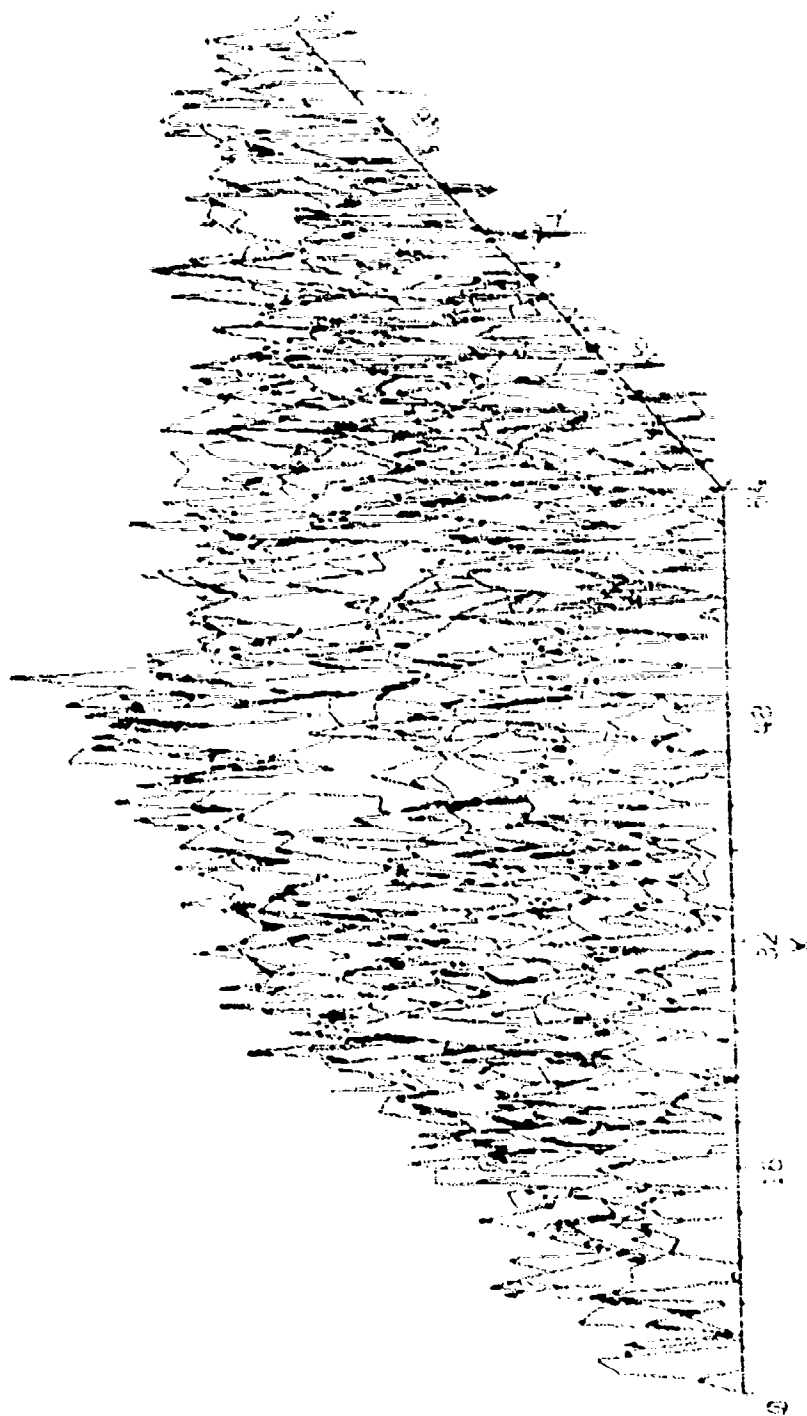


Figure 4.37 Measured Initial Point Spread Function
Including Detector Noise and Detector Size

Contour value (in waves)

0 -2.60
 △ -2.40
 + -2.20
 × -2.00
 ◇ -1.80
 ◆ -1.60
 × -1.40
 z -1.20
 y -1.00
 x -.80
 v -.60
 z -.40
 - -.20
 o .00
 - .20
 . .40
 ! .60
 ! .80
 = 1.00

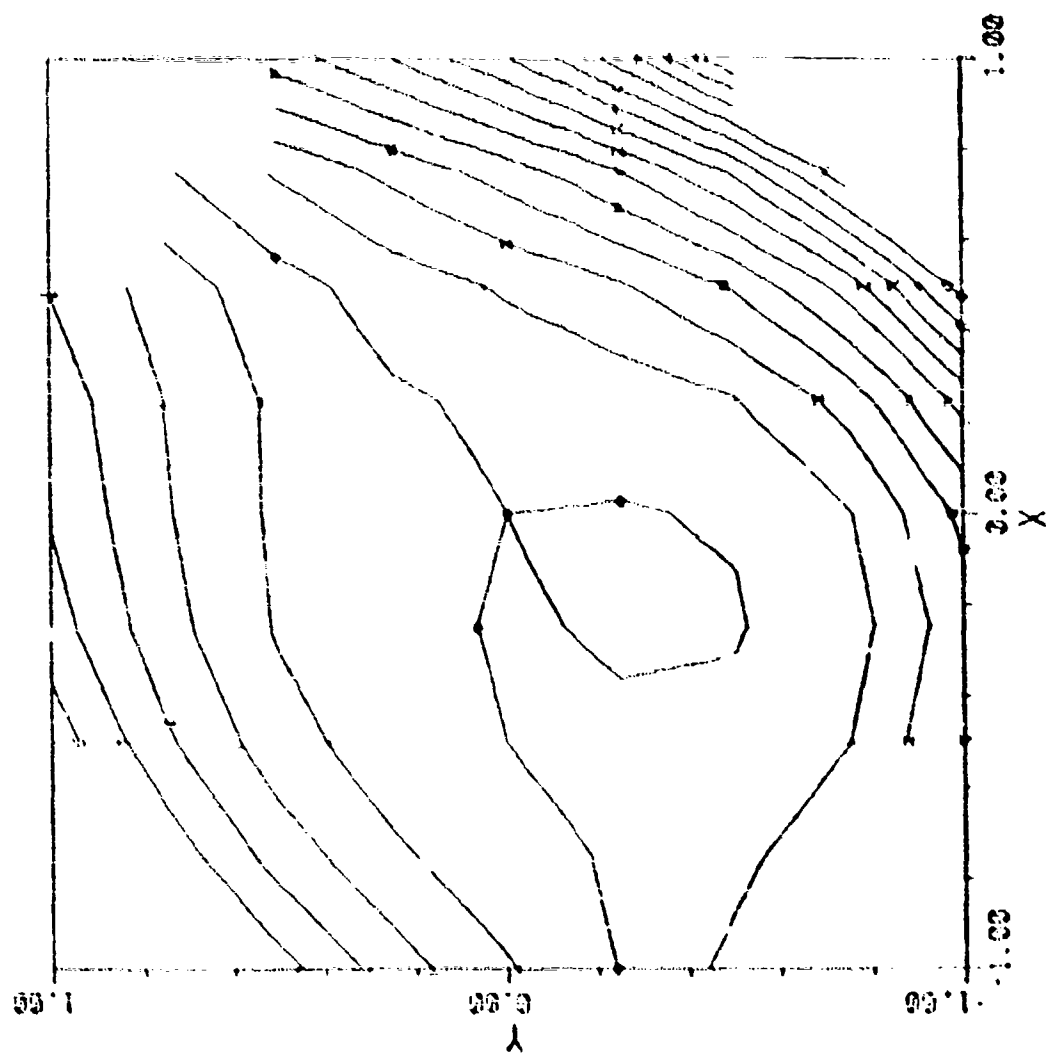


Figure 4.38 Phase Retrieval Estimate of Wavefront Aberration

was input to the aberration estimation algorithm appears as shown in Figure 4.37 (again multiplied by ten). Finally, the estimate of the system's wave aberration function produced by the algorithm is shown in Figure 4.38. This estimate is seen to be very accurate as is evidenced by the nearly diffraction limited point spread function which results after the adaptive optics are corrected, in Figure 4.39. All of the three-dimensional plots of point spread functions presented here are sampled at approximately twice the Nyquist rate in order to clarify the structure for ease in viewing; the sample spacing is 5.2 units. The PSF's actually used in the simulation program were sampled at only the Nyquist rate.

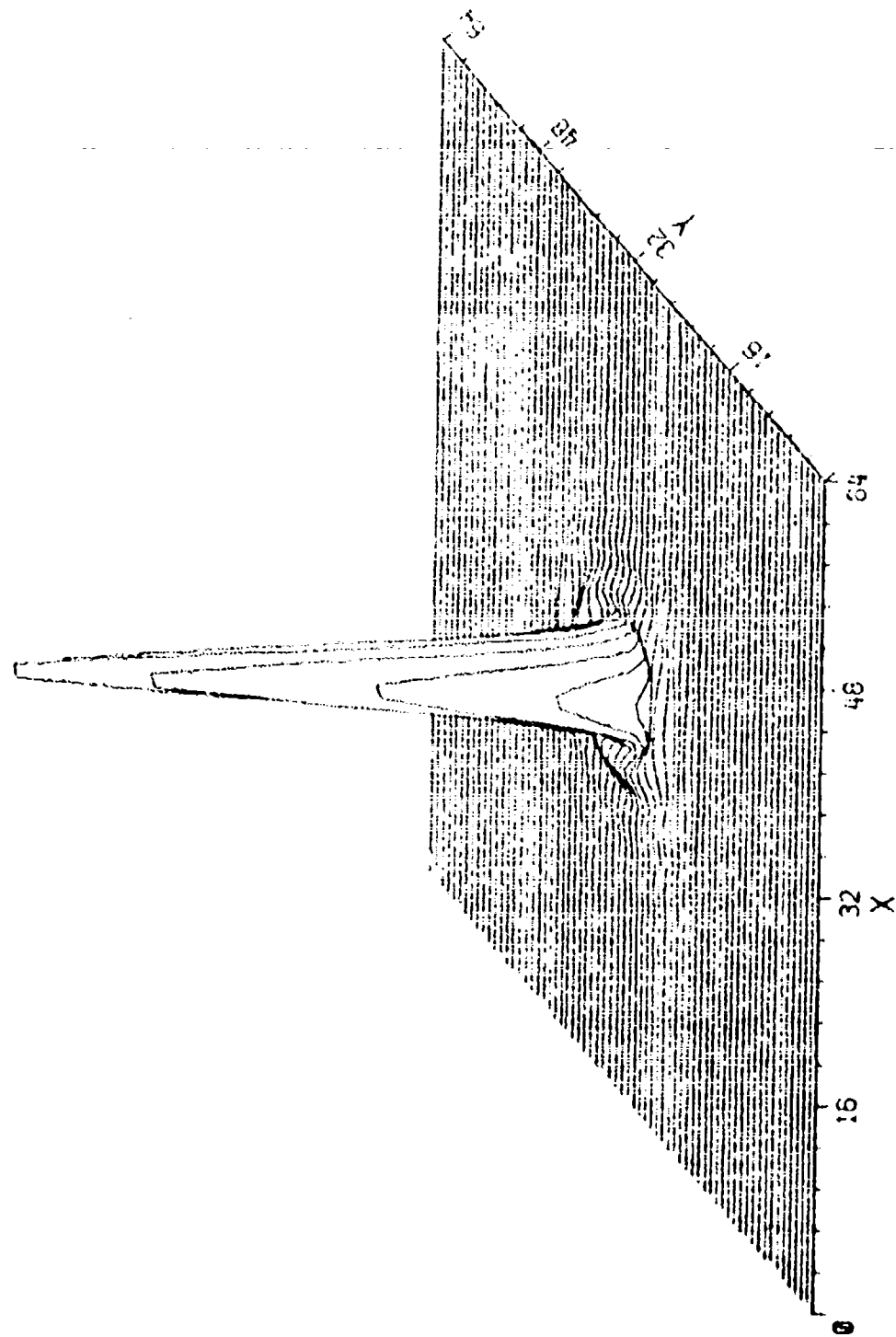


Figure 4.39 System Point Spread Function After Correction

5.0 THE TWO-IMAGE PLANE ALGORITHM

5.1 INTRODUCTION

The two-image plane algorithm was devised in order to perform wavefront aberration estimation from an unknown, extended object. When imaging a delta-function-like object, the transform of the measured signal $S(x,y)$ is $P(f_x, f_y)$, the OTF of the imaging system. An extended object yields a transform $M(f_x, f_y) = O(f_x, f_y) \cdot P(f_x, f_y)$, where O is the object transform. Since O is assumed unknown, P cannot be separated out to permit use of the one-image algorithm already discussed in Chapter 4. Appendix B presents the actual algorithm used and provides a more complete discussion of results than in this Chapter.

5.2 RESULTS

All the results presented here used two image planes separated by one wave of defocus, that is, a paraboloidal aberration which is zero at the center of the aperture and equal to one wave at the aperture edge is added to the existing aberration to simulate the result of moving the image plane. The proper amount to shift the image plane is presumably an amount which causes a significant change in the OTF; if the defocus is small compared to the aberrations already present, we would expect poorer results. Variations in the amount of shift were not investigated here. In an imaging system using a moveable image plane, the amount of defocus can be controlled as appropriate for the aberrations present.

Results are shown for only one particular phase aberration, although it is thoroughly investigated. The initial RMS wavefront error was .708 waves. All cases presented only simulated the operation of the extremely lengthy "complete"

algorithm which is virtually guaranteed of finding a good estimate in the absence of noise. Table 5.1 presents results for varying amounts of noise. Point detectors and point objects were used. The sampling is assumed to be at the Nyquist rate. The RMS error of the system after correction by the estimate is shown in the column labelled "RMS". As the noise increases, the error of the phase retrieval estimates also increases.

TABLE 5.1
Results of the Two Image Plane Simulations

RMS Error	Noise Level	Detector Size	Object Width	Case
0.708				Original
0.0	Noise	Point	Point	K
0.016	0.01	Point	Point	N
0.056	0.02	Point	Point	P
0.081	0.04	Point	Point	Q

Table 5.2 shows simulations with non-point detectors (but still point objects). As in the one image simulations, the detectors are assumed to be squares 100 units on a side, with a $\lambda F\#$ product of 20 units. The error in the phase estimate has increased by a factor of 10 for case U versus case N, both having a noise level of 0.01. Case Z, with 1/8 as much noise as case N still has a larger error. Figure 5.1 shows MTF's that reveal how much information is lost by use of 100 unit detectors. Figure 5.1(a) is the MTF from the initial aberration in case N. Figure 5.1(b) has had the noise from case N added. Figure 5.1(c) presents the transform of the detected signal, which is the MTF from Figure 5.1(a) multiplied by the transform of the detector response. Note that little information is present except at the very lowest frequencies. Figure 5.1(d) shows the result of adding

the noise in case Z (which is much less than in case N). These MTF's display only one quadrant.

TABLE 5.2
Results of the Two-Image Plane Simulations

RMS	Noise Level	Detector Size	Object Width	Case
0.708				Original
0.087	0.01	100	Point	U
0.070	0.005	100	Point	V
0.045	0.0025	100	Point	Y
0.022	0.00125	100	Point	Z

0.018 0.037 0.038 0.025 0.014 0.000 0.000 0.000 0.000
0.074 0.054 0.037 0.014 0.007 0.009 0.000 0.000 0.000
0.047 0.037 0.070 0.077 0.023 0.002 0.020 0.000 0.000
0.105 0.083 0.052 0.048 0.086 0.024 0.060 0.018 0.000
0.057 0.060 0.067 0.108 0.053 0.077 0.059 0.020 0.014
0.136 0.020 0.027 0.142 0.036 0.071 0.045 0.034 0.013
0.094 0.046 0.074 0.165 0.027 0.040 0.029 0.082 0.038
0.242 0.024 0.081 0.043 0.028 0.043 0.055 0.058 0.035
1.000 0.170 0.102 0.093 0.108 0.111 0.032 0.016 0.027

Figure 5.1(a) Case N, Original MTF

0.031 0.059 0.026 0.041 0.049 0.068 0.084 0.038 0.030
0.061 0.093 0.039 0.052 0.025 0.021 0.055 0.092 0.022
0.080 0.053 0.048 0.114 0.056 0.058 0.089 0.010 0.036
0.070 0.040 0.041 0.015 0.070 0.076 0.055 0.044 0.018
0.077 0.088 0.117 0.083 0.068 0.064 0.032 0.038 0.058
0.143 0.072 0.034 0.151 0.042 0.065 0.031 0.011 0.072
0.198 0.060 0.063 0.190 0.009 0.045 0.008 0.076 0.038
0.263 0.042 0.061 0.078 0.019 0.060 0.066 0.022 0.048
1.000 0.167 0.095 0.069 0.110 0.135 0.094 0.036 0.033

Figure 5.1(b) Case N, Noisy MTF

0.001	0.001	0.000	0.000	0.000	0.000	0.000	0.000	0.000
0.002	0.001	0.000	0.000	0.000	0.000	0.000	0.000	0.000
0.004	0.002	0.001	0.001	0.000	0.000	0.000	0.000	0.000
0.008	0.003	0.000	0.001	0.001	0.000	0.000	0.000	0.000
0.005	0.003	0.001	0.002	0.000	0.001	0.000	0.000	0.000
0.023	0.002	0.000	0.004	0.001	0.001	0.001	0.000	0.000
0.009	0.003	0.001	0.003	0.000	0.000	0.000	0.000	0.000
0.137	0.008	0.004	0.004	0.001	0.002	0.003	0.001	0.001
1.000	0.096	0.010	0.015	0.010	0.008	0.003	0.000	0.002

Figure 5.1(c) Case Z, Transform of Detected Signal of Point Object

0.003	0.004	0.003	0.006	0.008	0.008	0.010	0.005	0.004
0.005	0.006	0.004	0.004	0.004	0.002	0.007	0.011	0.003
0.000	0.001	0.003	0.008	0.004	0.007	0.011	0.001	0.004
0.003	0.003	0.002	0.005	0.007	0.006	0.003	0.004	0.002
0.008	0.007	0.005	0.008	0.004	0.003	0.006	0.002	0.007
0.023	0.005	0.001	0.006	0.006	0.004	0.003	0.005	0.009
0.006	0.004	0.005	0.005	0.003	0.001	0.003	0.003	0.002
0.138	0.010	0.008	0.004	0.002	0.006	0.002	0.006	0.004
1.000	0.095	0.013	0.019	0.010	0.010	0.008	0.004	0.004

Figure 5.1(d) Case Z, Transform of Detected Signal of Point Object Plus Noise

Cases AA, BB, and CC in Table 5.3 have the same noise and detector size as Case Z, but now an extended object is used. The object is taken to have an intensity in the image plane given by a Gaussian

$$I_{OBJ}(x,y) = \exp \left[-(x^2 + y^2)/D_{OBJ} \right].$$

TABLE 5.3
Results of the Two-Image Plane Simulations

RMS	Noise Level	Detector Size	Object Width	Case
0.708				Original
0.029	0.00125	100	157.1	AA
0.041	0.00125	100	314.2	BB
0.060	0.00125	100	628.3	CC
0.088	0.0025	100	628.3	DD

D_{OBJ} is listed in the table under "Object Width" and is in the same units as the detector size. The detected signal is given by the convolution of the system PSF with the detector response and the object distribution:

$$S(x,y) = PSF(s,y) \otimes D(x,y) \otimes I_{OBJ}(x,y)$$

The transform of I_{OBJ} is

$$I_{OBJ}(f_x, f_y) = \exp \left[- \pi^2 D_{OBJ}^2 (f_x^2 + f_y^2) \right]$$

The transform of the detected signal is

$$S(f_x, f_y) = OTF(f_x, f_y) D(f_x, f_y) \cdot I_{OBJ}(f_x, f_y)$$

As the object size increases (in case AA, BB, and CC in Table 5.3), the error on the phase retrieval estimate increases. The additional attenuation of the high frequencies due to the object size is shown in Figure 5.2, which represents the detected signal transform with and without noise, from case CC. This may be compared to case Z in Figure 5.1(c), in which the only difference is the use of a non-point object in case CC. More high frequency information is lost in case CC. Case DD, from Table 5.3 has twice as much noise as case CC, and may be compared with case Y, which has the same amount of noise but a point object. Case DD yielded an estimate having twice the residual error of case Y.

0.000	0.000	0.000	0.000	0.000	0.000	0.000	0.000	0.000
0.000	0.000	0.000	0.000	0.000	0.000	0.000	0.000	0.000
0.000	0.000	0.000	0.000	0.000	0.000	0.000	0.000	0.000
0.000	0.000	0.000	0.000	0.000	0.000	0.000	0.000	0.000
0.000	0.000	0.000	0.000	0.000	0.000	0.000	0.000	0.000
0.000	0.000	0.000	0.000	0.000	0.000	0.000	0.000	0.000
0.000	0.000	0.000	0.000	0.000	0.000	0.000	0.000	0.000
0.000	0.000	0.000	0.000	0.000	0.000	0.000	0.000	0.000
0.040	0.001	0.000	0.000	0.000	0.000	0.000	0.000	0.000
1.000	0.028	0.000	0.000	0.000	0.000	0.000	0.000	0.000

Figure 5.2(a) Case CC,
Transform of Detected Signal of Extended Object

0.001	0.003	0.003	0.006	0.008	0.008	0.010	0.005	0.004
0.003	0.006	0.009	0.004	0.004	0.002	0.007	0.011	0.003
0.004	0.002	0.003	0.008	0.004	0.007	0.011	0.001	0.004
0.005	0.006	0.002	0.004	0.008	0.006	0.003	0.004	0.002
0.004	0.004	0.006	0.006	0.004	0.004	0.005	0.002	0.007
0.004	0.006	0.001	0.005	0.006	0.004	0.004	0.005	0.004
0.012	0.003	0.005	0.002	0.003	0.001	0.003	0.003	0.002
0.041	0.003	0.003	0.005	0.003	0.006	0.001	0.006	0.004
1.000	0.027	0.004	0.003	0.001	0.002	0.004	0.004	0.005

Figure 5.2(b) Case CC,
Transform of Detected Signal of Extended Object Plus Noise

In summary, the two-image plane technique certainly works; it does suffer from the same problem as the one-image plane algorithm, that of very long execution times to insure the best estimate. Finally, it may be worth noting that although we have used the addition of defocus to the system, since it is easy to add a known amount, any sort of other aberration could also work, as long as it was known. These aberrations could be induced by varying the active optics, or by the introduction of aberrating elements into the optical system. Also possible are algorithms utilizing three or more different focus positions which may be useful in the presence of a large amount of noise, or for very large objects.

6.0 CONCLUSIONS AND RECOMMENDATIONS

EIKONIX has successfully demonstrated phase retrieval of a complex amplitude from its modulus under a wide variety of conditions. Our methods are directly applicable to the problem of actively controlling an optical system and possess definite advantages over other methods such as direct interferometric measurements of the wavefront aberration which requires integration of elaborate and costly electromechanical devices into the system. In particular, our algorithm works well for a wide variety of wavefront aberrations, reference objects, detector sizes and noise levels.

The only information needed to perform phase retrieval is the detected signal of a bright "point" object sampled at the Nyquist rate. Although the planned detector sizes would seem to preclude Nyquist sampling, use of image motion across the focal plane array, with suitably spaced time samples, can provide the necessary spatial resolution. Despite the fact that much of the higher frequency information in the OTF is lost due to the detector size, our simulations were successful with the planned HALO detector sizes.

Phase retrieval simulations have not been performed for polychromatic radiation but OTF calculations show that for a bandpass filter transmitting from 0.8 to 1.2 of the central wavelength, the polychromatic OTF differs only slightly, and at the higher frequencies, from the monochromatic OTF. This difference would be obscured by noise and the large detector size. Thus, we do not feel that there would be any difficulty in performing phase retrieval on broadband radiation provided some sort of filter is provided.

Simulations have been run using white noise on the detected signal as specified by the NEFD of the focal plane

detector arrays. Phase retrieval has been shown to be possible even when visually the signal from a point source is apparently totally obscured by the noise. The noise simulations also assumed a very narrow-band spectral filter which reduced the energy from the point source significantly. It should not be difficult to find stars which yield a sufficient signal-to-noise ratio.

It may be necessary to estimate aberrations in regions of the field of view which are totally below the horizon, and consequently will probably lack bright point objects. In this case, it is still possible to perform phase retrieval using a bright extended (non-point) object as a target; however, two images must be obtained at different focus positions. This procedure has been successfully simulated.

The chief difficulty with the method lies in executing the algorithm in an acceptable length of time. Current simulations take about thirty minutes on a PDP 11/70. Special purpose hardware could reduce this by at least a factor of 100 but the computation time increases extremely rapidly as the magnitude and the number of degrees of freedom of the wavefront aberration increases. It will be necessary to reduce the running time before realistic simulations of the HALO system could be performed.

Further study of the Gerchberg-Saxton algorithm is needed to understand its convergence problems in two dimensions. It works well in one dimension and has the potential to be much faster than the parameter search method.

Another question to be answered is the range of magnitudes of the aberrations such that phase retrieval can be performed in a specified period of time. This will impact on how accurate the initial alignment procedure must be. This question must

also be coordinated with a more realistic model of the aberrations expected from HALO, both at the point of takeover of control after the initial alignment, and the drifts in mirror positions as a function of time. Also to be considered are the effects of short term fluctuations which could cause shifts in the aberrations between measurements done at slightly different times, which otherwise would have been expected to be measuring exactly the same aberration functions.

The problem of precisely which stars that are bright enough to be used as point objects and which will be able to be acquired is not yet answered. Although there are many stars which would be suitable, there is the additional constraint that nearly simultaneous measurements be made in perhaps six different isoplanatic regions.

Simulation of extended (non-point) objects has been limited to Gaussian intensity distributions. Other kinds of objects, such as random scenes, may be more appropriate.

The problem of "deconvolution", that is, obtaining mirror positions from a knowledge of the wavefront error in several different regions of the field of view is complicated by the two-fold ambiguity in the phase retrieval estimates inherent in any problem with a symmetrical pupil function. Although many of the field points will not have a nearly symmetrical pupil, the magnitude of this problem must be determined in conjunction with the designers of the HALO optical system. Simulations so far have only treated the case of on-axis imaging of a symmetric optical system. Eventually off-axis cases must be considered, and possibly non-symmetric systems. A realistic treatment will involve more detailed knowledge of the optical system.

MISSION
of
Rome Air Development Center

ESD plans and executes research, development, test and selected acquisition programs in support of Command, Control, Communications and Intelligence (C³I) activities. Technical and engineering support within areas of technical competence is provided to ESD Program Offices (POs) and other ESD elements. The principal technical mission areas are communications, electromagnetic guidance and control, surveillance of ground and aerospace objects, intelligence data collection and handling, information system technology, ionospheric propagation, solid state sciences, microwave physics and electronic reliability, maintainability and compatibility.